SALTWATER ENTRAINMENT FROM BATHYMETRIC DEPRESSIONS: A CFD ANALYSIS FROM A LABORATORY CAVITY TO A SCOUR HOLE IN THE HARINGVLIET ESTUARY

Master thesis
by
Ashraf Al-mohagry
November 2023

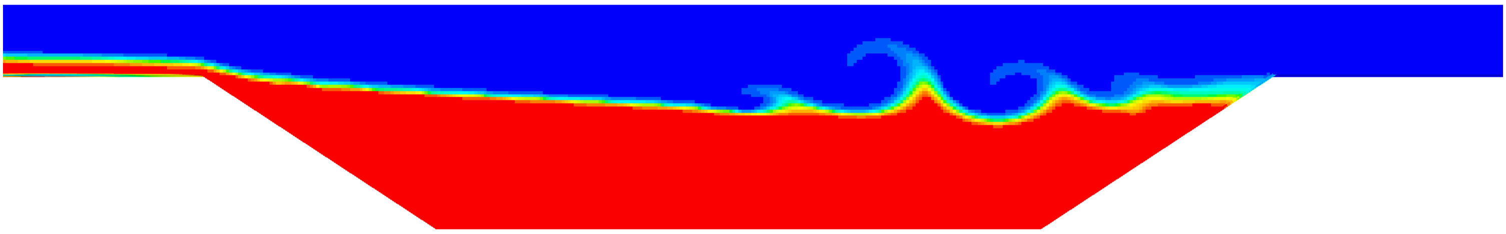

University of Twente supervisors:
Prof. Suzanne J.M.H. Hulscher
Dr. Vasileios Kitsikoudis
Fateme Ebrahimierami

Deltares supervisor:
Dr. Tom O'Mahoney

Preface

After an enriching journey of pursuing my bachelor's and master's degrees across diverse countries and continents, I am filled with a profound sense of pride and fulfilment as I present my MSc thesis. This journey, filled with diverse experiences, has taught me invaluable lessons about life, contributing to my personal growth, self-awareness, and potential. These experiences have thoroughly equipped me with the resilience and knowledge necessary for a successful career in river and coastal management engineering, a field that deeply resonates with my passion.

My time spent at Deltares working on my thesis was enriching and rewarding as it allowed me to explore the complexities of fresh-saltwater dynamics in a research environment ideal for intellectual development. Before embarking on this journey, I had limited knowledge of Computational Fluid Dynamics and stratified flow dynamics. However, Deltares provided the perfect setting for learning about these important topics.

I extend sincere thanks to my graduation committee members for their valuable contributions. I am particularly grateful to Tom O'Mahoney for his consistent guidance, supervision, and sharing of valuable experiences at Deltares, along with his profound technical and theoretical advice, which greatly deepened our discussions and my understanding of the subject matter. I am grateful to Tommaso Boschetti for the insightful conversations we had regarding the model setup.

Special thanks to Vasileios Kitsikoudis for his continuous support, guidance, and insightful feedback on various aspects of my project. Gratitude is also extended to Fateme Ebrahimierami for providing the field data of the Haringvliet, which was part of the SALTISolutions project's Work Package 3.2. This data was used for validating the Haringvliet CFD model of this study. My acknowledgements would be incomplete without thanking Suzanne Hulscher for her valuable insights and feedback during the feedback meetings.

I must express my boundless gratitude to my family for their unwavering support and encouragement throughout my academic journey. Lastly, I am deeply grateful to the University of Twente scholarship, which enabled me to achieve my dream of pursuing a master's degree in Water Engineering and Management in the Netherlands.

Ashraf Al-mohagry
November 2023

Abstract

Saltwater intrusion, especially in semi-closed estuaries such as the Haringvliet, poses threats to freshwater availability. Proper sluice management helps in maintaining water balance but determining the saltwater entrainment from the scour holes is needed to reduce saltwater intrusion. This is important considering climate change's worsening effects on freshwater availability. Despite existing studies on flushing saltwater from cavities, there is an existing knowledge gap in quantifying the saltwater entrainment rate from real-life scour holes. The primary research question focused on accurately predicting saltwater entrainment rates from cavities using CFD modelling in both lab and real-world scales using the commercial software Star CCM+. To understand the entrainment of saltwater in cavities, a systematic methodology was implemented. A lab scale model was first developed, referencing the physical model by Debler and Armfield (1997). Though Kirkpatrick et al. (2012) had earlier developed a validated model using a computationally demanding Large Eddy Simulation (LES), the current study pursued a less resource-intensive approach. Findings revealed that model choices such as meshing size and choice of Schmidt number had a significant role in the performance of the model. The field scale model of the Haringvliet scour hole showed a good agreement with the field observations, unlike what was observed for the lab scale model, which had more varied success. Finally, the study recommends further research on saltwater intrusion, broader data validation, and exploration of other software like OpenFOAM which allows for a higher degree of modelling control.

Contents

List of Figures

List of Tables

Nomenclature

Abbreviation	Meaning
CFD	Computational Fluid Dynamics
FDM	Finite Difference Method
FVM	Finite Volume Method
FEM	Finite Element Method
DNS	Direct Numerical Simulation
LES	Large Eddy Simulation
DES	Detached-Eddy Simulation
RANS	Reynolds-averaged Navier-Stokes
URANS	Unsteady RANS
PIV	Particle Image Velocimetry
LIF	Laser Induced Fluorescence
TKE	Turbulence Kinetic Energy
MV	Material Volume
K-H	Kelvin-Helmholtz
2DV	Two-Dimensional Vertical
ADCP	Acoustic Doppler Current Profiler
CTD	Conductivity-Temperature-Depth Device
NAP	Normaal Amsterdams Peil (Amsterdam Ordnance Datum)
RMSE	Root Mean Square Error
2D	Two-Dimensional
3D	Three-Dimensional

Symbol	Unit	Meaning
ϕ	-	Intensive property
Δt, t	s	Time interval, Time
MV	-	Material Volume
ρ_{SMOW}	kg/m^3	Standard Mean Ocean Water Density
ρ_{fw}	kg/m^3	Freshwater Density
ρ_{sw}	kg/m^3	Saltwater Density
V	m^3	Volume
D	m	Channel Depth
H	m	Cavity Depth
$\mathbf{v}(t,\mathbf{x})$	m/s	Flow Velocity Vector
U_e	m/s	Entrainment Velocity
V	m/s	Freshwater Inflow Velocity
∇	-	Nabla (vector operator)
Γ^{ϕ}	m^2/s	Diffusion coefficient of ϕ
Q$^{\phi}$	-	Generation/destruction of ϕ per unit volume
Re	-	Reynolds number
u	m/s	Typical flow velocity
L, l	m	Typical length scale, Length scale
l	m	Length scale
v	m^2/s	Kinematic viscosity
μ	Pa·s	Molecular dynamic viscosity
Fr	-	Froude number
g	m/s^2	Gravitational acceleration
d, h	m	Uniform water depth, Height from Bottom of Cavity to Saltwater Interface
S_{ct}	-	Schmidt Number
RMSE	-	Root Mean Square Error
D	m^2/s	Mass diffusivity
Ri_0	-	Richardson number
$\Delta\rho$	kg/m^3	Density difference
E	-	Entrainment Rate
S	kg/m^3	Salinity
T	℃	Temperature
α	-	Coefficients in UNESCO Density Formula
β	-	Coefficients in UNESCO Density Formula
γ	-	Coefficients in UNESCO Density Formula
k	-	Turbulent kinetic energy
ε	-	Turbulent dissipation rate

1 Introduction

Saltwater intrusion is a common issue faced in semi-enclosed estuaries, like the Haringvliet. The Haringvliet is a large inlet of the North Sea that was closed in 1970 as part of the Delta Works in the Netherlands (Kranenburg et al., 2023). The intrusion of saltwater to such semi-closed systems occurs through structures like shipping locks or sluices, which is the case with the Haringvliet sluices. The management of the sluices at the Haringvliet plays a crucial role in controlling saltwater intrusion in this semi-closed estuary. These sluices are strategically operated in sync with the natural ebb-tide cycle, allowing for the controlled release of freshwater into the North Sea during periods of low tide. By coordinating the release of freshwater from the sluices with periods of low tide, when the sea level is at its lowest, the natural flow of the water helps flush away saltwater that enters the Haringvliet back to the sea. This management strategy helps to maintain a balance between freshwater and saltwater, minimizing the intrusion of saltwater into the Haringvliet.

Saltwater intrusion into such a semi-closed system leads to its accumulation in scour holes and depressions within the estuary. Over time those saline pools become dangerous to fish and other aquatic organisms that use these deeper pools for breeding and as safe locations to escape from other predators (Kirkpatrick et al., 2012). Additionally, saltwater intrusion can impact significantly the availability and quality of freshwater needed for drinking and irrigation (Konikow & Kendy, 2005). In order to mitigate salt intrusion, it is effective to increase the discharge of freshwater, as the amount of intrusion is mostly dependent on the discharge from the river system (An et al., 2009; Augustijn et al., 2011; Nguyen et al., 2008; Sierra et al., 2004). However, it is very important to determine the minimum amount of water volume needed to flush the salt water away from the scour holes it accumulated in. Given the growing freshwater shortage anticipated by climate change and drought events, it is crucial to estimate the precise amount of freshwater needed to remove the saltwater. Debler and Armfield (1997), Strang and Fernando (2004) and Williamson et al. (2018) investigated the process of flushing a denser fluid from a cavity using a less-dense fluid which resembles the flushing of saltwater with freshwater. Notably, the terms "cavities" and "scour holes" both refer to depressions or holes, but their distinction lies in their origin and scale. Cavities and scour holes, both types of depressions, can form naturally or be man-made. Scour holes are distinct from cavities in that they are depressions formed by the erosive process of flowing water and can usually be found near hydraulic structures such as sluices or locks.

Saltwater, being denser than freshwater, tends to accumulate in cavities, making them ideal locations for saltwater accumulation. While existing literature provides valuable insights into the physical processes involved in lab-scale models of saltwater flushing from cavities, there remains a substantial knowledge gap when it comes to quantifying the freshwater required to flush saltwater from real-life scour holes. This knowledge gap is particularly critical given the increasing scarcity of freshwater due to climate change. To bridge this gap and contribute to freshwater preservation, this study focuses on studying the flow behaviour within an actual scour hole in the HaringVliet using a Computational Fluid Dynamics (CFD) model, which has been validated with both a lab scale model and field scale model. The findings of this study are particularly useful in understanding the processes that contribute to the saltwater removal from a scour hole. These insights are useful in the development of effective sluice management strategies aimed at mitigating saltwater intrusion.

1.1 Problem Statement

In a comprehensive literature analysis, Almohagry (2023) investigated the flushing of saltwater from cavities and found out that limited knowledge exists on the quantifying the entrainment rate of saltwater from a scour hole and its relation to the dynamics of the sheared flow in a stratified environment. Previous research conducted by Debler and Armfield (1997), Strang and Fernando (2004) and Williamson et al. (2018) employed observational methods to examine the flow dynamics in cavities. These studies have provided valuable insights into the relationships between saltwater entrainment rates and various flow rates. However, the range of geometries explored in these studies was limited and did not include real-world configurations, such as those encountered in natural scour holes. Consequently, the limited scope of the present literature constrains our capacity to draw definitive conclusions concerning saltwater entrainment rates and the flow dynamics taking place within a real-world scour hole.

1.2 Knowledge gaps

Problem 1: The presence of walls, slopes, and other geometric features within a cavity can give rise to the formation of vortices, eddies, and intricate flow patterns between the stratified layers that need to be investigated and understood better. The current comprehension of the flow dynamics within these cavities is limited to a small set of experimental observations characterized by restricted flow conditions and geometric variations. This shortfall in available data underscores our limited understanding of how saltwater is entrained from a cavity. Therefore, the goal is to further investigate the behaviour of the fluid within a cavity by modelling and understanding the effects of fluid properties, such as velocity and fluid density, on the flow patterns and pressure gradients within the cavity, as well as the relations between the flow behaviour and the geometry of the cavity.

Problem 2: Laboratory investigations offer valuable insights into a system's behaviour. However, for a comprehensive understanding and predictive capability of how the system will perform in the field, it is often crucial to scale up these studies to real-world dimensions. This is because the physics and dynamics of a system can exhibit scale dependent variations, potentially rendering observations from a controlled laboratory setting inapplicable to larger scales. This could mean that the eddies formed in a small scale model would disappear or grow even larger in a large scale scour hole raising the need to investigate the behaviour of the saltwater entrainment from large scaled scour holes. Consequently, upscaling the model becomes imperative to grasp how the mixing of flow and the entrainment rate of saltwater would evolve at larger scales, corresponding to those encountered in scour holes within the Haringvliet.

1.3 Research objectives

The main objective of this research is to model the flushing of saltwater from cavities and to assess the most influential parameters that would allow for a better understanding of this mechanism and ultimately allow for enhancing the effectiveness of saltwater entrainment from cavities. This research will further explore the governing processes of saltwater entrainment efficiency in an upscaled model representing real-world scour holes. The expected outcome of this study includes an enhanced understanding of the saltwater entrainment rate under freshwater inflow in both lab and real-world scales.

1.4 Research questions

The main research question of ***"How can the entrainment rate of saltwater from cavities be accurately predicted using CFD modelling with Reynolds-Averaged Navier-Stokes (RANS) and Detached Eddy Simulation (DES) as modelling approaches in laboratory and real-world scales?"*** is formulated to address the aforementioned objectives. In order to completely address this research question, it must be broken down into a number of sub-questions. These sub-questions are as follows:

1. Which turbulence model, in terms of precision and computational efficiency, best estimates the entrainment rate of saltwater from the laboratory scale cavity?
2. How does the dynamics of the flow change when the model is upscaled to replicate the dimensions of a scour hole in the Haringvliet and what consequences does this transformation have on the entrainment rate of saltwater?
3. How does the entrainment rate from the field data of the Haringvliet compare to the theoretical relation in the literature?
4. How does the change in the saltwater interface as observed in the Haringvliet compare to the predictions of the CFD model?

2 Literature review

Gaining a deep understanding of the factors that contribute to the entrainment of saltwater from a cavity is a crucial step in addressing the objectives of this thesis effectively. This section investigated the process of flushing saltwater from a cavity using freshwater and examined the underlying physical phenomena. Additionally, this section explored the numerical techniques employed to model this process, as have previously been published in academic literature.

2.1 The characteristics of cavities

Scour holes are created when the sand particles are eroded by the flow, for instance as seen near hydraulic structures, where the turbulence in the flow can result in an increased erosion. The shape of a scour hole can be approximated to an experimental setup as cavity. A cavity refers to an empty or hollow place within a solid object or structure. This can be with varying aspect ratios (length/height of the cavity), angles, and shapes. Even though scour holes have irregular shapes in nature, a cavity is a very simple representation of reality that allows to study a complex flow phenomenon. The shapes of the cavities examined in the literature under density stratified flow are mostly trapezoidal and rectangular as seen in Debler and Armfield (1997). A good example of a cavity set up in the laboratory is seen in the study by Debler and Armfield (1997) where the experimental apparatus consisted of a laboratory flume and a cavity created by a transparent box. The schematic of the cavity is shown in Figure 2.1 and the description of each of the parameters shown in the schematic is explained in Table 2.1.

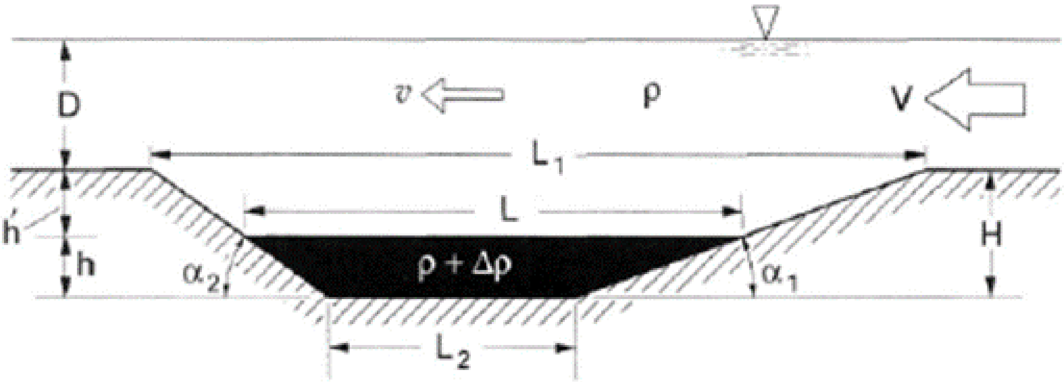

Figure 2.1. Schematic sketch of the cavity (Debler & Armfield, 1997)

The geometry of a cavity is important because it affects the efficiency and productivity of the withdrawal process. The shape, size, and orientation of the cavity can affect the flow separation at the upstream edge of the cavity, and this can control the formation of vortices (Debler & Armfield, 1997). A flow over a simple geometry cavity could exhibit phenomena which can include complex wave interactions, multiple flow and acoustic instabilities and resonant tones. Even though the

Table 2.1. List of symbols and their descriptions as used in Figure 2.1

Symbol	Description
L	Mean length of interface in the cavity
L_1	Length of the cavity opening at the elevation of the channel floor
L_2	Length of the cavity floor
h	Mean depth of saline (dyed) water in the cavity
H	Geometric depth of the cavity
D	Depth of water in the channel
α_1	Angle of decline of the upstream cavity wall
α_2	Angle of incline of the downstream cavity wall
ρ	Density of the water in the channel
$\rho + \Delta\rho$	Combined density of the dyed saline water in the cavity
v	Inferred water speed in the channel as it passes over the cavity
V	Average water speed in the channel at depth D

flow is complex, there are four processes that occur within this dynamic system. Those processes are vortical disturbance amplification by the fluid shear layer, generation of pressure wave by vortex surface interaction, propagation of acoustic waves upstream, and conversion of the waves into vorticity waves at the upstream edge (Rowley & Williams, 2006). The vorticity formation is complex even in the case of a constant density as seen in Figure 2.2. The system complexity will increase in the case of density stratified flow where the mixing between the two layers will change the behaviour of the system. For instance, the degree of steepness of the slopes at the edges of the cavity and the flow conditions can result in a film formation that transports part of the saltwater away (Debler & Armfield, 1997). However, such behaviour is not fully understood due to the limited number of experiments carried out.

Figure 2.2. Vorticity contours for a square cavity (Rowley & Williams, 2006)

2.2 The effects of varying the geometry of the cavity on the flow

Debler and Armfield (1997) investigated different end wall slopes and cavity profiles. According to the authors, it was possible to efficiently characterize the impact of the geometrical characteristics and the cavity aspect ratio by normalizing a non-dimensional purging velocity with the square of the densimetric Froude number Fr_d defined in Equation 1.

$$Fr_d = \frac{u}{\sqrt{gH\frac{\Delta\rho}{\rho_0}}} \tag{1}$$

Where u is the flow velocity, g is the acceleration due to gravity, H is the depth of the cavity, $\Delta\rho$ is the difference in density between the two layers of fluid, and ρ_0 is the density of the reference fluid.

Furthermore, the following can be inferred from their experiments:

1) Aspect Ratio and End-Wall Effects:

A wide range of cavities with varying slopes and varying flow conditions were investigated with the aim of finding the methods of eliminating the cavity vortex and the upstream surface depression that occurs early in the experiment. Based on their experiment, they found out that a slope of less than 10° roughly would prevent the channel flow from separating. Moreover, they found that the surge wave that formed at the upstream region of the cavity, see Figure 2.3a, could be suppressed if the channel flow acceleration was carried out sufficiently slowly. Even yet, the interface did exhibit a slight tilt, which caused its downstream height to rise over the top of the cavity as would be predicted.

The authors plotted the normalized rate of purging against the depth of the saline water h for all 33 experiments they recorded and concluded that indeed there could be a relation inferred from their results that can allow for estimating a normalized purging rate for certain geometry of the cavities for similar conditions that were present in the experiments in which most of the saline water transport was due to the breaking of the interfacial waves and the turbulence in the flow.

A film that transported liquid out of the cavity formed on the wall for 10°, 14°, and 21° for the turbulent flow but only occurred for 10° and 14° in the case of laminar flow. The authors also made a conclusion based on limited information that the transport of the fluid by this film is only significant towards the end when the cavity is almost empty. Based on this, further study can be carried out to investigate the effect of this film on the flow at different conditions.

2) Rectangular Cavities and Aspect Ratio Influences:

According to Debler and Armfield (1997), the interface tilt and interfacial shear became very important contributors to the saltwater withdrawal when h exceeded 12 cm. Furthermore, for rectangular cavities, the purging rate will decrease as the aspect ratio increases for a fixed depth. Furthermore, the energy transfer coefficient (K_{ET}) remained approximately the same with a value of 0.0145 ± 0.0030 over a range of values of h and only increased as the cavity became empty.

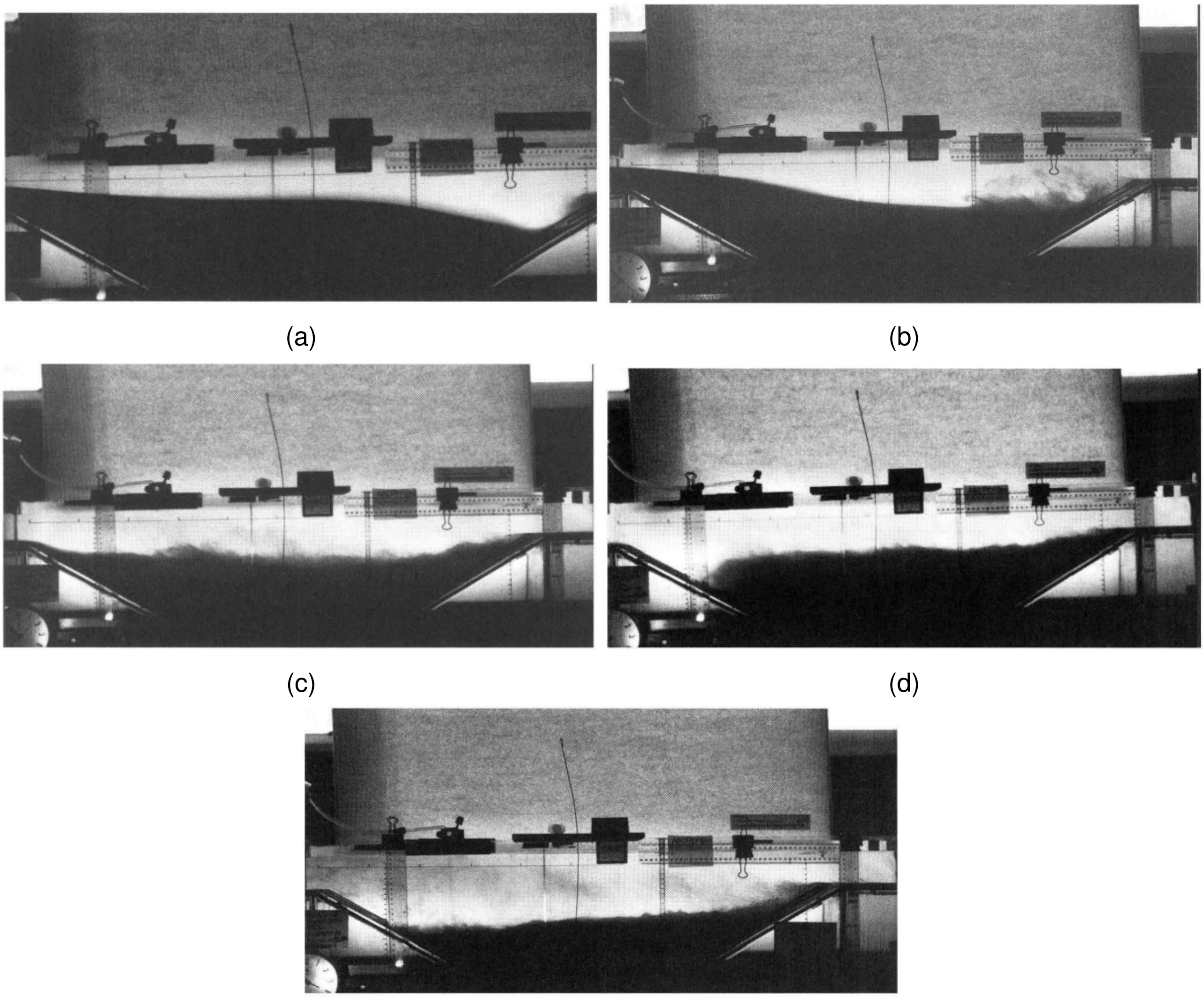

(a) (b) (c) (d) (e)

Figure 2.3. Photographs taken at different times over the course of the experiment (Debler & Armfield, 1997). (a) Photograph captured at 6-10 seconds showing the saltwater interface at the downstream end raising due to the initiation of the flow; (b) Eruption of the interface at the upstream edge of the cavity; (c) The interface falls back after the initial incline due to the flow initiation; (d) The saltwater interface drops as the entrainment of saltwater continues at the downstream end of the cavity; (e) Wisps of dyed fluid ejected by the breaking interfacial waves into the flowing stream

3) Rectangular vs Trapezoidal Cavities:

The results obtained in the study showed that the vortex was effective in transporting most of the saline water. A comparison of the trapezoidal and rectangular cavity data shown in Figure 2.4 provides evidence that supports the effectiveness of the vortex in flushing away the saltwater. Data sets 1a to 8a correspond to a trapezoidal cavity whereas data sets 9a and 10a correspond to rectangular cavities. Moreover, data sets 1a and 2a of the trapezoidal cavities had approximately the same parameters and conditions as the experiments for data sets 9a and

10a. With this in mind, it can be inferred from Figure 2.4 that the surging rate was relatively higher for the rectangular cavities when compared to the trapezoidal ones. This is due to the stronger vortices that form in the rectangular cavities. Moreover, the authors explained that using separate examination, it was found out that the energy transfer coefficient (K_{ET}) for the rectangular geometry at $h = 0$ was 0.019, whereas K_{ET} for the trapezoidal shape was 0.011 which shows that the rectangular cavity experienced higher energy due to the stronger vortices formed.

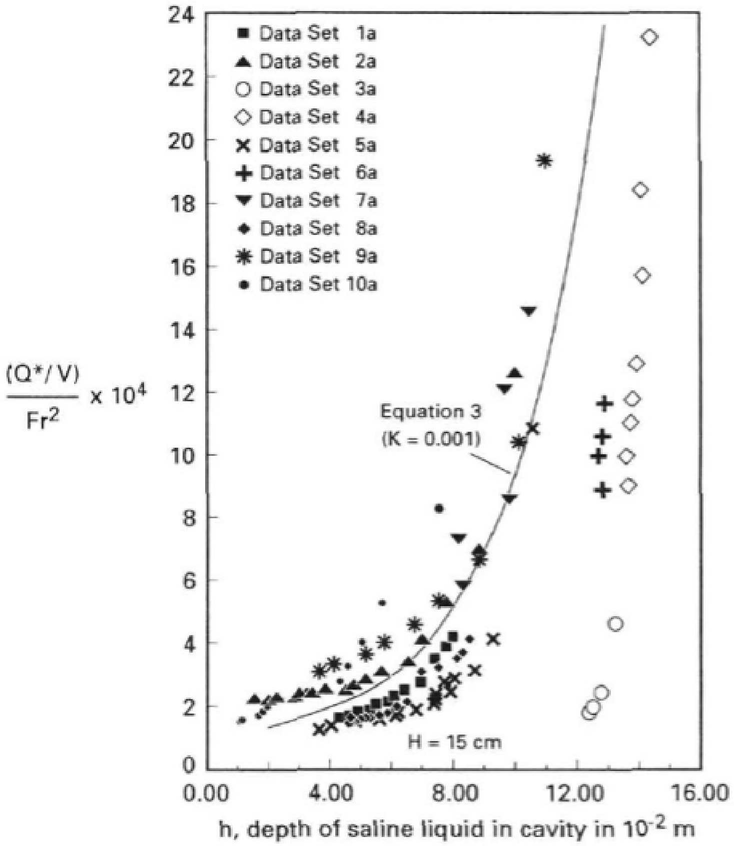

Figure 2.4. Dimensionless purging velocity, Q^*/V, plotted against the depth of saline fluid for trapezoidal and rectangular cavities with an aspect ratio of 10 under continuous channel flow conditions. Q^* represents the volume rate of saline water flushing per unit length of interface, while V denotes the average water speed in the channel. Data sets 1a-8a correspond to trapezoidal cavities, while data sets 9a and 10a correspond to rectangular cavities. Data sets 1a and 2a of the trapezoidal cavities share similar flow conditions with experiments in data sets 9a and 10a (Debler & Armfield, 1997)

2.3 Physical phenomena occurring during shear flow at cavities

Strang and Fernando (2004), Kirkpatrick and Armfield (2005) and Baratian-Ghorghi and Kaye (2013) have demonstrated that the flow may be described by an interface entrainment mechanism. This entrainment is coupled with an exchange between the turbulent overflow and the interior of the cavity. Furthermore, the entrainment is characterized by a turbulent nature for cavities with low aspect ratios where cavity length/cavity depth is within the range of 1 to 2.

Flow development and vortices formation:

Interfacial mixing is produced as a result of the flow's disruption and the interface's stability. This turbulent mixing occurs due to the lateral circulation, surface and bottom wall shear, local effects of sidewalls, and the transmission of turbulence from any upstream disturbances, such as a boundary layer or pumps in laboratory setups (Williamson et al., 2018). According to Debler and Armfield (1997), the following phenomena have been noticed to occur as the liquid starts to flow over a density-stabilized pool:

1. The wave created by the overflow at the interface causes a significant volume of the denser fluid to be plunged out of the cavity and be carried away as seen in Figure 2.3a.
2. A vortex emerges from the upstream border of the pit, takes part of the denser fluid, and combines with it as seen in Figure 2.3b.
3. For short cavities characterized by a relatively small length with respect to their depths, it is noted that the mixing occurring consists of a three-layered system. The liquid within the short cavity is continuously flushed by large amplitude seiching motions that are commonly occurring within these short cavities. However, this seiching, which involves rhythmic oscillations of water layers usually seen in semi-enclosed body of water, eventually fades away and is succeeded by a circulatory motion that occurs within the mixed layer and takes away the denser, nearly still, liquid from the bottom of the cavity through the actions of shear stresses and molecular diffusion.
4. Unlike short cavities, step (2) and the circulatory motions described in step (3) are not of a major contribution towards the total liquid flushed away from the bottom of a long cavity. Instead, the freshwater flow past the interface result results in localized vortices at the upstream and the downstream margins which in turn transports most of the liquid out of the cavity.

Regarding vortex formation, Debler and Armfield (1997) observed that by gradually descending into the cavity, it becomes possible to prevent flow separation at the upstream edge of the depression, thus averting the formation of a vortex that enhances transport rates. This gradual inclination facilitates the removal of denser fluid from the depression through interfacial shear. Further elaboration on flow separation and vortex formation is provided below.

In a similar context, Kirkpatrick and Armfield (2005) investigated the purging of saline water from a square cavity with fresh water and offered a comparable explanation of the evolving flow dynamics. Their study delineated four distinct phases of purging. The initial three phases resembled Kelvin-Helmholtz billows and encompassed splashing, seiching, and vortex formation. The fourth phase was characterized by the deformation of the interface, marked by turbulent pinched flow, which was subsequently succeeded by the emergence of thin fluid structures from the denser fluid.

Flow separation:

The traditional understanding of flow separation attributes this phenomenon to the effects of viscosity, often described as "boundary layer separation." This phenomenon typically arises in two-dimensional and axisymmetric steady flows and is contingent upon the presence of an adverse pressure gradient, where the pressure increases in the direction of the flow, known as a positive or adverse pressure gradient. Consequently, flow separation is generally induced by an adverse pressure gradient, combined with the effects of viscosity, whether the flow is laminar or turbulent. The absence of either an adverse pressure gradient or viscosity typically means the flow will remain attached to the wall.

Figure 2.5a shows an example of flow separation, characterized by the detachment of the boundary layer from the surface in response to a positive pressure gradient extending in the stream-wise direction. This detachment gives rise to vortex formation (top right of the figure), a common occurrence in fluid dynamics when the velocity of the flow decreases and the downstream pressure escalates, resulting in a situation where the flow ceases to maintain contact with the surface.

Conversely, the removal of the boundary layer through suction effectively neutralizes the impact of viscosity along the channel walls (Figure 2.5b). Preceding the channel's throat, the narrowest section, there is a decrease in pressure along the flow direction, and this is attributed to the diminishing cross-sectional area. In this specific zone, the pressure gradient becomes negative (or advantageous), ensuring complete adherence of the flow to the walls. However, post-throat, the significant divergence or a substantial adverse pressure gradient leads to the detachment of the boundary layer from the wall, culminating in vortex formation (Figure 2.5a). Nonetheless, by applying suction to the boundary layer downstream of the throat, the flow can be reestablished, adhering to the surface (Figure 2.5b).

Moreover, a notable increase in pressure along the flow direction can be seen in areas adjacent to the stagnation point; however, flow separation is averted due to the lack of wall friction. Close to the wall, the flow remains attached as the fluid within the boundary layer moves towards a region of decreasing pressure (CHANG, 1970). Nevertheless, the introduction of a thin projecting plate leads to flow separation, attributed to both the pressure increase along the flow direction and the emergence of wall friction.

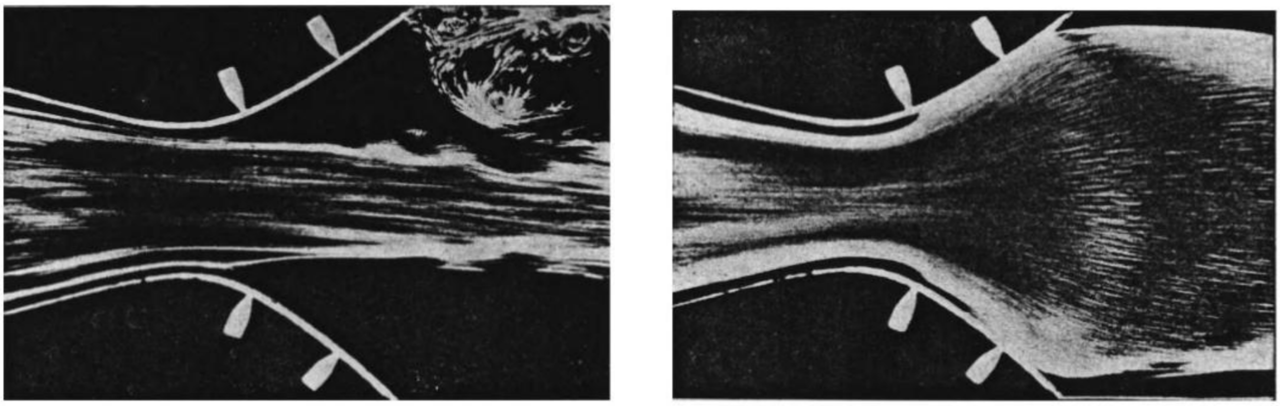

(a) Flow separation in a rapidly diverging channel.

(b) Suction of the boundary layer from both walls and its effect on flow separation.

Figure 2.5. Illustration of (a) flow separation and vortex formation due to positive pressure gradient in stream-wise direction, and (b) boundary layer removal by suction and negative pressure gradient effects in a channel's narrow throat section (CHANG, 1970).

Vortices formation:

In fluid dynamics, a vortex is often associated with the rotational motion of fluid around a central axis. This behaviour is characterized by vorticity, a vector field that represents twice the angular velocity of a fluid particle. When vorticity aligns in a co-directional or nearly co-directional manner, it forms a concentration referred to as a vortex. This vortex motion leads to the creation of circular or nearly circular streamlines (Kundu et al., 2012; Nitsche, 2006). It's important to emphasize that vorticity within a flowing fluid is not typically unidirectional or steady. Instead, vorticity is embedded within fluid elements, allowing it to be reoriented, concentrated, or diffused based on the motion and deformation of the fluid element and the torques applied by neighbouring fluid elements (Kundu et al., 2012).. In the vicinity of a vortex, fluid circulation occurs, resulting in an increase in velocity as one approaches the vortex core and a simultaneous decrease in pressure.

Internal Cavity Mixing:

Debler and Armfield (1997) used colour to dye the saline solution to allow for observing the mixing between the two layers of the fresh and saline waters. The authors observed wisps of fluid, see Figure 2.3e, at the interface which allowed them to conclude that the intermediary mixing layer was very thin. Moreover, the authors observed that the volume of the denser fluid at the bottom of the cavity remained unchanged during the large fluid evacuation phenomena. Finally, the authors explained that the seiching motions that were causing the mixing became more evident as the cavity became almost empty. Besides, Kirkpatrick and Armfield (2005) explained that this small-scale turbulence characterized by the fluid wisps that were ejected from the denser fluid only becomes important at the final stage which confirms the observations made by Debler and Armfield (1997).

2.4 Governing equations & Parameters characterizing the flow

Conservation equations:

The conservation of mass, momentum, and energy are all governing equations that involve specific quantities or intensities to describe the dynamics of the flow. Those conservation equations are applicable to any intensive property ϕ, such as a concentration of a solute in a solution or a mass fraction from the total mass. According to Moukalled et al. (2016), the variation of any intensive property ϕ over time within a controlled volume can be expressed using the following balance equation:

Change of ϕ over time (Δt) within the material volume (MV) **Term 1**	=	Surface flux of ϕ over time (Δt) across the control volume **Term 2**	+	Source/sink of ϕ over time (Δt) within control volume **Term 3**

Considering a fixed control volume, the Reynolds transport theorem can be used to express Term 1 as follows:

$$\text{Term I} = \int_V \left[\frac{\partial}{\partial t}(\rho\phi) + \nabla \cdot (\rho \mathbf{v} \phi)\right] dV \tag{2}$$

Where ρ is the fluid density, V is the volume, and $\mathbf{v}(t, \mathbf{x})$ is the flow velocity vector as a function of position $\mathbf{x}$ and time t. The term $\rho\mathbf{v}\phi$ represents the transport of ϕ by the flow field and represents the convective flux. The term ∇ is a vector operator known as "nabla" and defined as:

$$\nabla = \frac{\partial}{\partial x}\mathbf{i} + \frac{\partial}{\partial y}\mathbf{j} + \frac{\partial}{\partial z}\mathbf{k} \tag{3}$$

The second term is the result of diffusion which is produced by molecular collisions. Therefore, the second term can be expressed as follows:

$$\text{Term II} = \int_V \nabla \cdot (\Gamma^{\phi} \nabla \phi) dV \tag{4}$$

Where Γ^{ϕ} is the diffusion coefficient of ϕ. Finally, Term 3 is represented as follows:

$$\text{Term III} = \int_V Q^{\phi} dV \tag{5}$$

Where Q^{ϕ} is the generation/destruction of ϕ within a control volume per unit volume. Therefore, the above three terms are combined to form the following:

$$\int_V \left[\frac{\partial}{\partial t}(\rho\phi) + \nabla \cdot (\rho \mathbf{v} \phi)\right] dV = \int_V \nabla \cdot (\Gamma^{\phi} \nabla \phi) dV + \int_V Q^{\phi} dV \tag{6}$$

Through some integration and rearrangements of the above equation, the final formula of the general conservation equation for the transport of property ϕ is stated as:

$$\underbrace{\frac{\partial}{\partial t}(\rho\phi)}_{\text{unsteady term}} + \underbrace{\nabla \cdot (\rho \mathbf{v} \phi)}_{\text{convection term}} = \underbrace{\nabla \cdot (\Gamma^{\phi} \nabla \phi)}_{\text{diffusion term}} + \underbrace{Q^{\phi}}_{\text{source term}} \tag{7}$$

Flow characteristics:
When writing the conservation equations in non-dimensional form, you get dimensionless numbers that are very useful for carrying out parametric studies of engineering problems (Moukalled et al., 2016). For this study, the Reynolds, Froude, Richardson, and Schmidt dimensionless numbers are considered.

According to Moukalled et al. (2016), Reynolds number (Re) describes the relative importance of the advection (inertia) to the diffusion (viscous) momentum fluxes. This parameter can help in determining whether the flow regime is laminar, turbulent, or in between and is defined using the equation below:

$$Re = \frac{uL}{v} = \frac{\rho uL}{\mu} \tag{8}$$

Where L is a typical length scale (e.g., the depth), u is a typical flow velocity, v is the kinematic viscosity of water, and μ is the molecular dynamic viscosity. For Re values less than 2000, the flow is typically laminar, which means the fluid moves in smooth, orderly layers without much mixing between them. As the Reynolds number increases, specifically in the range between 2000 and 4000, the flow undergoes a transition phase. During this transition range, the flow characteristics can fluctuate between laminar and turbulent, making the flow patterns less predictable and more varied. When the Reynolds number exceeds 4000, the flow is generally considered turbulent. This turbulent flow is marked by chaotic, irregular fluid motions and the formation of eddies, leading to a high degree of mixing within the fluid. Each of these flow regimes, from laminar to turbulent, represents distinct physical behaviours of fluids under varying conditions of velocity and viscosity.

The Froude number is defined as the ratio of the characteristic velocity to the gravitational wave velocity as given by the following equation:

$$Fr = \frac{u}{\sqrt{gd}} \tag{9}$$

Where d represents a uniform water depth. A Froude number larger than 1 indicates a supercritical flow, while a value less than 1 indicates a subcritical flow and a value of 1 indicates a critical flow, which means that the flow velocity is equal to the velocity of the surface waves.

The Schmidt number is a dimensionless value that compares how momentum and mass are diffused in a turbulent flow. Specifically, it represents the ratio of the eddy diffusivity of momentum to the eddy diffusivity of mass (Di Bernardino et al., 2020) as seen in Equation 10.

$$S_{ct} = \frac{v}{D} \tag{10}$$

Where (D) is the mass diffusivity (Moukalled et al., 2016).

In examining shear-driven entrainment flows, the Reynolds and Schmidt numbers, along with the Richardson number, emerge as key non-dimensional parameters (Kirkpatrick et al., 2012). In this regard, Linden (1979) has formulated the Richardson number, as illustrated in Equation 11. Further emphasizing the importance of this parameter, Meehan et al. (2022) highlighted the significant role of the Richardson number, denoted as Ri_0, especially in determining the frequency of large-scale vortex formation. This parameter is of particular relevance in stratified fluid flows, where density variations play a crucial role in influencing the dynamics of the flow.

$$\mathrm{Ri}_0 = \frac{g\Delta\rho l}{\rho_0 u^2} \tag{11}$$

Where ρ is the density, u is the velocity, and l is a length scale.

Under different Richardson numbers, distinct phenomena in fluid dynamics are observed. For a Ri_0=0, the entrainment rate is anticipated to be infinite. In scenarios where Ri_0<0, the influence of buoyancy becomes negligible, allowing shear forces to take dominance. Within this specific range, the entrainment process is primarily driven by turbulent eddies caused by shear forces, characterized by their swirling fluid motions, which effectively incorporate fluid from the surrounding environment. On the other hand, when Ri_0>20, the effects of buoyancy are so pronounced that molecular diffusion becomes the exclusive mechanism for entrainment. The Richardson number attains a critical value at 0.25. When the value descends below this critical point, it induces stirring turbulent motions through small-scale eddies, which in turn generate the expulsion of thin streams of denser fluid from peak regions. These streams subsequently undergo mixing as they are transported away by the overflow (Kirkpatrick et al., 2012). In these situations, involving sheared interface flows, the emergence of shear-driven instabilities, particularly Kelvin-Helmholtz and Holmboe waves, is observed, presenting a unique mechanism for modifying the density interface.

2.5 Stratified flow governing parameters

Baratian-Ghorghi and Kaye (2013), Kirkpatrick and Armfield (2005) and Strang and Fernando (2004) have demonstrated that the flow may be described by an interface entrainment mechanism coupled with an exchange between the turbulent overflow and the interior of the cavity characterized by a turbulent nature for cavities with low aspect ratios where cavity length/cavity depth is within the range of 1 to 2. Christodoulou (1986) studied the turbulent phenomenon at the density interface of 4 types of stratified flows available in the literature. Based on that, he identified 4 governing laws relating the Richardson number to the flow type and the mixing process. These laws are summarized in Table 2.2.

Table 2.2. Flow and mixing conditions based on the Richardson number (Christodoulou, 1986)

Richardson number (Ri_0)	**Flow conditions**	**Mixing occurs through:**
For small Richardson number ($Ri_0 < 0(l)$)	Supercritical	Vortex entrainment & $Ri_0^{-\frac{1}{2}}$ law holds
For large Richardson numbers ($Ri_0 > 0(l)$)	Subcritical	Cusp entrainment & $Ri_0^{-\frac{3}{2}}$ law holds
Intermediate range of Ri_0	Unity of supercritical and subcritical	Mixing following Ri_0^{-1} law.
Value approaching zero ($Ri_0 \sim 0$)	Critical	Similar mixing that occurs in homogenous fluid with Ri_0^0 asymptotic law.

In addition, investigations were carried out by Townsend (1958) using a turbulent jet of intermediate density injected along a steady gravity interface. He observed that when the values of the Richardson number exceeded 0.3, the turbulent entrainment of the fluid from the jet nearly vanished. According to Christodoulou (1986), the conclusions he made allow for accurate quantification of the interfacial mixing rates with a variety of flows. Furthermore, Xuequan and Hopfinger (1986) explained that a turbulent eddy will enter the interfacial layer and result in thickening the interface when very small values of Ri_0 exist, see Figure 2.6, whereas the interface will smooth out for large values of Ri_0.

Chu and Baddour (1984)investigated a cavity-like flow using laboratory tests under stable gravity stratification. The authors looked at how the surface jet developed and demonstrated that the flow initially expands as a planar wall jet with a nearly self-similar velocity profile. It was determined that the expansion rate was quite similar to that of a non-buoyant wall jet. Also, they observed no relationship between the stratification and the initial development of the flow near the exit of the cavity. Williamson et al. (2018) divided the flow explained by Chu and Baddour (1984) into two regions where the first region describes the region where the development of the surface jet occurs, and the second region is the region starting downstream where the jet vanishes, and a

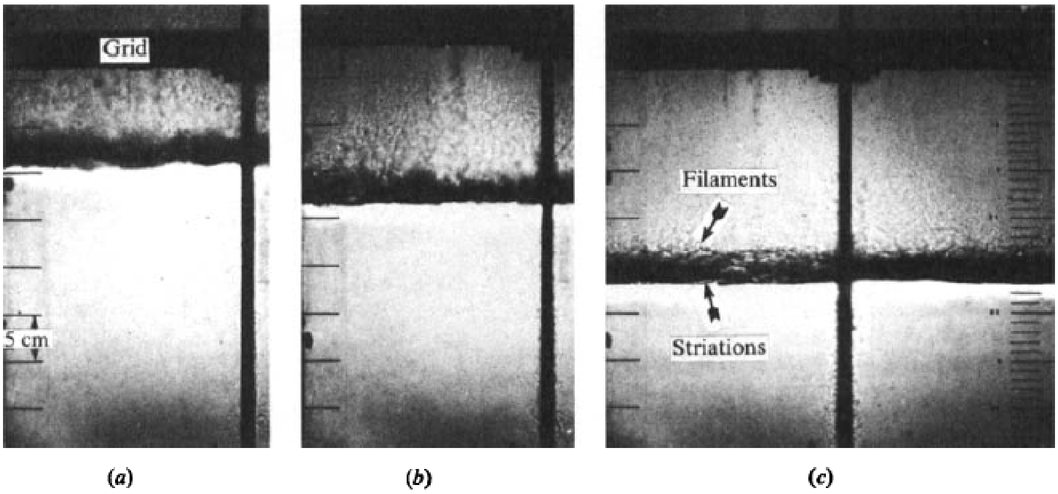

Figure 2.6. Mixed layer deepening for difference Richardson number. (a) Ri_0=22.1; (b) Ri_0=53.9; (c) Ri_0=199.8 (Xuequan & Hopfinger, 1986)

parallel flow starts to develop with growing thickness of the mixing layer. Williamson et al. (2018) describes the entrainment in regions 1 by the relation $u_e/U_0 \sim Ri^{-1}$ and describes the mixing behaviour in region 2 with the relationship $u_e/U_b \sim Ri_b^n$ with U_b being a local scale and $n \approx -1$ where Ri, U, and u are the bulk Richardson number, bulk velocity in the cavity, and characteristic entrainment velocity respectively.

Strang and Fernando (2001) related the entrainment rate to the Richardson number using a similar approach to that of Williamson et al. (2018). Strang and Fernando (2001) used different entrainment relations based on the type of the stratified layers and the Richardson number range. 2.3 summarizes the relationships they proposed.

Table 2.3. Entrainment based on the bulk Richardson number and the stratification case, where f_N is the frequency ratio ($f_N = \frac{ND}{\Delta U}$) (Strang & Fernando, 2001)

Bulk Richardson number (Ri_B)	Stratification case	Entrainment relation
$1.5 < Ri_B < 5$	Two-layer	$E \approx 0.22 Ri_B^{-2.6}$
	Linearly stratified ($0.7 < f_N < 1.8$)	$E \approx 0.076 Ri_B^{-2}$
	Linearly stratified ($2.1 < f_N < 4.8$)	$E \approx 0.033 Ri_B^{-1.6}$
$Ri_B > 5$	Two-layer	$E \approx 0.02 Ri_B^{-1.3}$
	Linearly stratified ($1.4 < f_N < 4.8$)	$E \approx 0.02 Ri_B^{-1.25}$

The entrainment relation of both the two-layer and the linearly stratified cases were very similar for the second range of Richardson numbers ($Ri_B > 5$). The symmetric Holmboe waves or the asymmetric wave are more prevalent for such values of the Richardson number. Whereas the entrainment of the two-layered case is twice as large as the linearly stratified case in the Kelvin-Helmholtz regime for the first range of Richardson values. Moreover, the growing Holmboe waves, a second shear instability, replace the Kelvin-Helmholtz (K-H) instability dominated regime through a transitional phase $3.2 < Ri_B < 5.8$ where the K-H activity stopped entirely after the bulk Richardson number $Ri_B \sim 5$ or local gradient Richardson number $\overline{Ri}_g \sim 1$ (Strang & Fernando, 2001). The differences between the Kelvin-Helmholtz and the Holmboe instabilities are shown in Figure 2.7.

Williamson et al. (2018) found using particle image velocimetry and laser-induced fluorescence measurements that the flow regime is dominated by the Holmboe wave instability for a flow having a bulk Richardson number range Ri_B between 1 to 19, Reynolds number ranging between 7100 to 15100, and aspect ratios ranging between 2.4 to 16. Furthermore, their research concluded that the entrainment rate for these ranges can be described by the relation $E = CRi_B^{-1.38}$ where C is 0.02. Also, they noticed that there was no clear dependence noticed between the entrainment rate and the interface length.

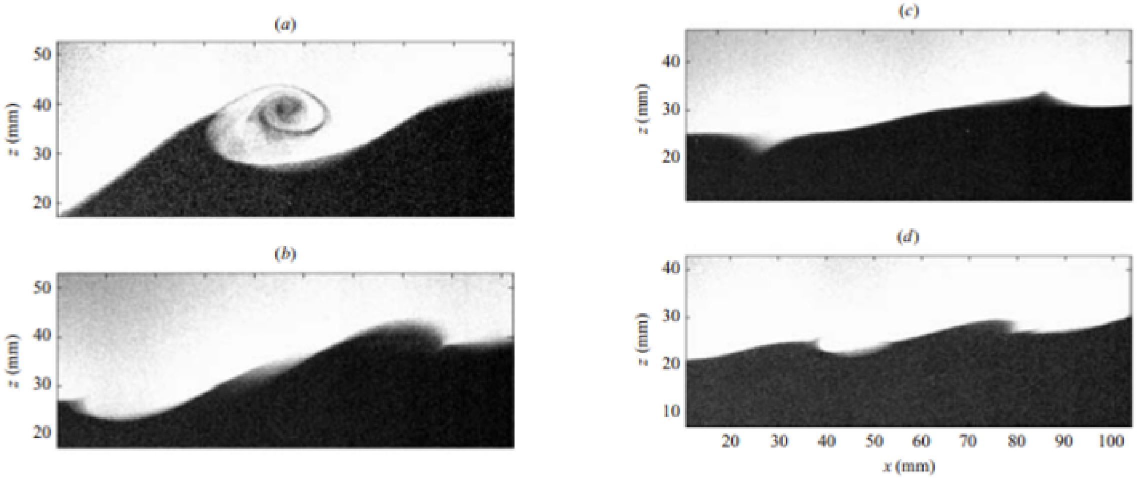

Figure 2.7. Transition from Kelvin–Helmholtz to Holmboe transition: (a) Pure KH instability, (b) both KH and Holmboe's instability (c) Holmboe's instability (d) Holmboe's instability with two oppositely propagating modes (Hogg & Ivey, 2003)

2.6 Quantifying saltwater withdrawal rate

Debler and Armfield (1997) used a dyed test saline solution to investigate the withdrawal rate of the saltwater when flushed away using fresh water. They conducted their studies over a range of cavities with aspect ratios ranging between 1.0 and 16.7, cavity edges with angles ranging between 8.5° and 90°, and a range of velocities U_c with continuous and intermittent channel flow. Water was abruptly introduced to a flume upstream at the beginning of an experiment such that it would flow over the cavity on its way out of the apparatus via the downstream weir. The flow was initiated with a rapid opening valve, and with the help of calibrated flow measuring devices, the average flow velocity was obtained depending on the channel width and depth. The authors took photographs of the processes that occurred after the flow initiation and then used these photographs to qualitatively determine the amount of saline liquid flushed away from the cavity as a fraction of the original dyed volume. Also, they made use of a hypodermic needle and a density meter to take measurements of the density of the saline solution in the middle of the cavity throughout the process. Furthermore, using the photographs acquired throughout the experiments, the authors calculated the entrainment velocity $u_e = dh/dt$ as a function of the average interface height h in the cavity. Williamson et al. (2018) approach, similar to Debler and Armfield (1997), used dye visualization and a camera to carry out the measurements in the experiment. The authors made use of particle image velocimetry (PIV) and laser induced fluorescence (LIF) to measure the entrainment velocity using three different approaches. The three approaches were based on measuring the difference in interface depth, the difference in salinity across the cavity, and the rate of change in salinity.

Debler and Armfield (1997) and Kirkpatrick et al. (2012) explained that when the nondimensional entrainment rate u_c/U_c is scaled by the square of a cavity Froude number $Fr_{\text{cav}} = U_c/(\Delta bH)^{1/2}$ expressed using the channel velocity, interfacial buoyancy jump $\Delta b = -\Delta\rho g/\rho_0$, and cavity height H, the experimental data collapses rather well. They created a scaling formula for the entrainment rate using physical reasoning based on a balance between the bulk flow of turbulence kinetic energy (TKE) into the cavity and the potential energy needed to move the heavier fluid from the interface to the top of the cavity.

$$\frac{L}{D}\left(\frac{Q^*}{V}\right)\frac{1}{Fr^2} = \frac{K_{ET}}{(l - h/H)\left([1 + H/D] - h/D\right)^2} \tag{12}$$

where L is the interface length, D is the height of the channel, and K_{ET} is an energy transfer coefficient that is used for the mixing efficiency.

Theoretical formulations to assess the withdrawal rate are based on idealized conditions which cease to exist near hydraulic structures as the flow is highly non-uniform and hard to predict. Hence, these equations fail to effectively quantify the rate of saltwater selective withdrawal (Boschetti et al., 2017; de Fockert et al., 2022; Jirka, 1979). This is where CFD proves useful. de Fockert et al. (2022) used a CFD model to analyze the patterns of water flow around the salt screen and the efficiency of selective withdrawal. Furthermore, Boschetti et al. (2017) explained that the replication of a 3D problem with the two-dimensional vertical (2DV) CFD model showed a good agreement between the 2DV measurements and the scale model results for a case study on selective withdrawal from a discharge sluice at the Eastern Scheldt dam. Hence, Boschetti et al. (2017) concluded that CFD can be used to quantify the selective withdrawal and optimize the salt screen's design.

3 Methodology

3.1 Overview of CFD Modelling approach

The CFD process to simulate fluid dynamics using a modelling tool is summarized in the schematic shown in Figure 3.1. Initially, the fluid problem must be conceptualized and clearly defined. In addition, an understanding of the fluid physical properties is required. The Navier-Stokes equations are the principal equations of the CFD model and they should be discretized using a mathematical discretization technique to transform the turbulent flow into a system of algebraic equations. This process aims to obtain an approximate solution to the actual turbulent flow solution, and it involves the usage of several mathematical discretization techniques such as the finite difference method (FDM), finite volume method (FVM), and finite element method (FEM) (Rashaduddin & Waheedullah, 2017; Zawawi et al., 2018). Figure 3.2 illustrates the trend of approximation between the numerical and the actual solutions of the turbulent flow equations. After meshing the whole model domain, a computer program is written to solve these discretized partial differential equations and obtain the simulation results. These simulations could be further validated through comparison with real-life problems and assessment through performance indicators such as resilience, reliability, and vulnerability. Resilience is about the ability of the model to overcome failure. Reliability is checked by assessing the model's capability to satisfy the conceptualized model objectives, and vulnerability is about quantifying the failure of the model (Hossain et al., 2018; Loucks & Van Beek, 2017; Zawawi et al., 2018).

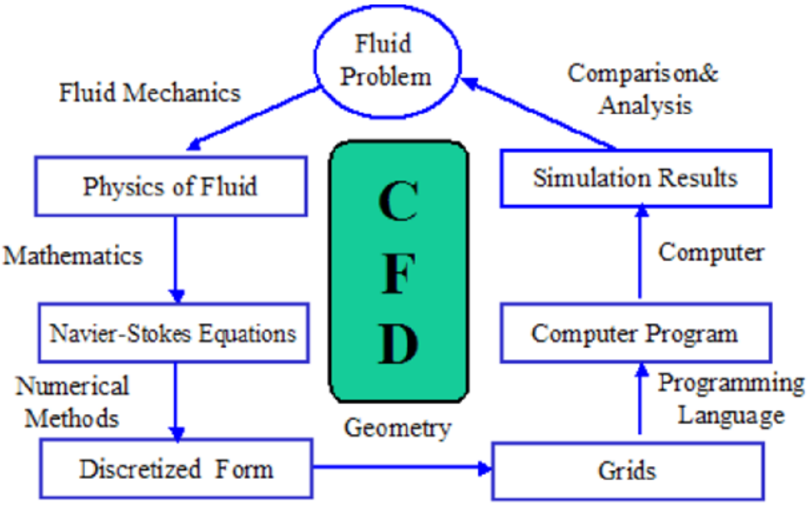

Figure 3.1. General CFD model development and simulation process (Zawawi et al., 2018)

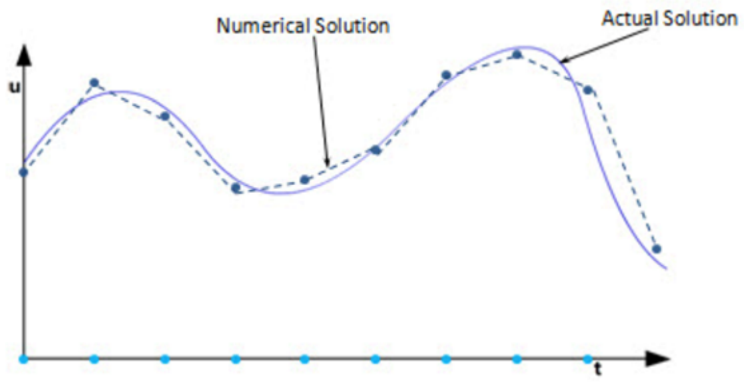

Figure 3.2. Approximation of the actual solution by the numerical one (Zawawi et al., 2018)

3.1.1 Numerical Discretization Techniques used to solve partial differential equations (PDEs)

The FDM is a widely used discretization technique due to its simplicity. However, it is limitedly used in modelling software that aims to solve problems with complicated geometries at high accuracy and precision. The FVM method is commonly utilized in CFD models, as it is efficient in terms of time and memory computational demands, especially when the computational problem involves a high Reynolds number (Surana et al., 2007; Zawawi et al., 2018). In this method, discrete control volumes are used to solve the Navier-Stokes equation and the other partial differential equations on turbulent flow, mass, and energy conservation physical laws. Finally, the FEM method requires higher computational demands compared to the FVM, as it should be precisely formulated to attain a conservative state for the developed partial differential equations. However, FEM offers superior stability compared to FVM, making it the preferred choice for conducting fluid dynamics analyses (Bakker et al., 2001; Surana et al., 2007).

3.1.2 Closure Models

When averaged, the Navier-Stokes equations present an imbalance, leading to a greater number of unknown variables than available equations to solve them. To address this imbalance, empirical equations, known as closure models are employed to bridge the gap by supplementing the system with additional equations.

In addressing the "closure" problem within the system of equations, the Boussinesq eddy-viscosity approximation is often applied (Wilcox, 1994). This method connects the Reynolds stresses to the average motion's strain rate by drawing a comparison between the dynamics of turbulent flows and molecular movements. In this approximation, the turbulence eddies are viewed as very small volumes of fluid. These volumes behave similarly to molecules that collide with and exchange momentum with others, reflecting principles from the kinetic theory of gases (Argyropoulos & Markatos, 2015; Markatos, 1986).

The Reynolds-averaged Navier–Stokes (RANS) approach is described by several models, including zero, half, one, and two-equation models (Argyropoulos & Markatos, 2015; Markatos, 1986; Rodi, 2017). Each model offers unique benefits and limitations, but the two-equation models, particularly the k-ϵ and the k-ω models, are the most widely adopted, especially in industry settings, and are considered the best choice for general CFD computations.(Argyropoulos & Markatos, 2015; Markatos, 1986).

These two-equation models expand on the mean flow equation of Navier-Stokes with two additional transport equations. The first of these accounts for the kinetic energy of turbulence, k, and the second for various factors that affect this energy, such as dissipation rate ε, specific dissipation rate ω, and the extents of length and time, as well as their combined effects with k.

For capturing unsteady mean-flow structures, unsteady RANS (URANS) is a viable method. However, RANS is limited to time-averaged data and, as such, cannot provide all the details of unsteady flow necessary for noise analysis (Thompson et al., 2015).

3.1.3 Direct Numerical Simulation (DNS)

In DNS, the time-dependent Navier-Stokes equations are directly computed, capturing every scale of turbulence without the need for a distinct turbulence model, offering the most comprehensive insight into turbulent flow dynamics. Hence, DNS is occasionally described as a 'virtual wind tunnel' (Thompson et al., 2015). Since highly detailed computational grids are required to accurately simulate the smallest motion magnitudes, makes DNS notably resource-intensive, rendering it challenging and often unfeasible for complex flows at larger Reynolds numbers.

3.1.4 Large Eddy Simulation (LES)

To mitigate the high computational demands of DNS, the LES approach was developed by Smagorinsky (1963). Based on the theory of Kolmogorov (1991) it is understood that larger turbulence magnitudes hold the majority of the energy, which then cascades down to smaller magnitudes. As shown in Figure 3.3, the energy in these smaller scales represents only a small portion of the total. In LES, the average and larger types of flow and the energy-rich eddies are directly resolved, while the structures at a small scale in the dissipation range are represented by a sub-grid scale stress term. In LES, both the average flow and the larger eddies holding significant energy are explicitly calculated, while the structures at the small scale in the dissipation spectrum are approximated using a sub-grid scale stress term. Though LES is less costly compared to DNS, it necessitates a substantial number of grid cells, particularly around solid surfaces, and requires very small time step iterations, rendering it impractical for most industrial applications (Thompson et al., 2015).

3.1.5 Detached-Eddy Simulation (DES)

DES was first proposed in 1997 (Argyropoulos & Markatos, 2015; P. Spalart et al., 1997) and began to be utilized in 1999 (Argyropoulos & Markatos, 2015; P. R. Spalart, 2008). DES was designed to address the issue of high-flow separations at high Reynolds numbers, and it integrates elements of both LES and RANS methodologies, taking into account the turbulence length scale and grid spacing. In this hybrid approach, LES is employed in regions of significant flow separation, while RANS is used within the boundary layer. Travin et al. (2000) describe DES as a three-dimensional, unsteady numerical approach that utilizes a unified turbulence model. This model operates as a sub-grid scale model in areas where the grid is adequately fine for large-eddy simulation purposes and as a Reynolds-averaged model in areas where the grid density is insufficient for such simulations (Argyropoulos & Markatos, 2015).

DES models have been specifically designed to resolve wall-bounded flows at high Reynolds numbers, where the entire boundary layer is treated by URANS models and the LES treatment is applied to the separated regions further from the walls. The computational requirements for DES are between those of LES and URANS while the accuracy of the complete flow field is potentially similar to LES (Thompson et al., 2015).

The DES models are developed to address wall-bounded flows characterized by high Reynolds numbers. In these scenarios, the entire boundary layer is subjected to URANS models, while LES is dedicated for the separated regions located farther away from the walls. In terms of computational demands, DES falls between the requirements of LES and URANS (Thompson et al., 2015). However, it offers the potential for accuracy in modeling the entire flow field as LES.

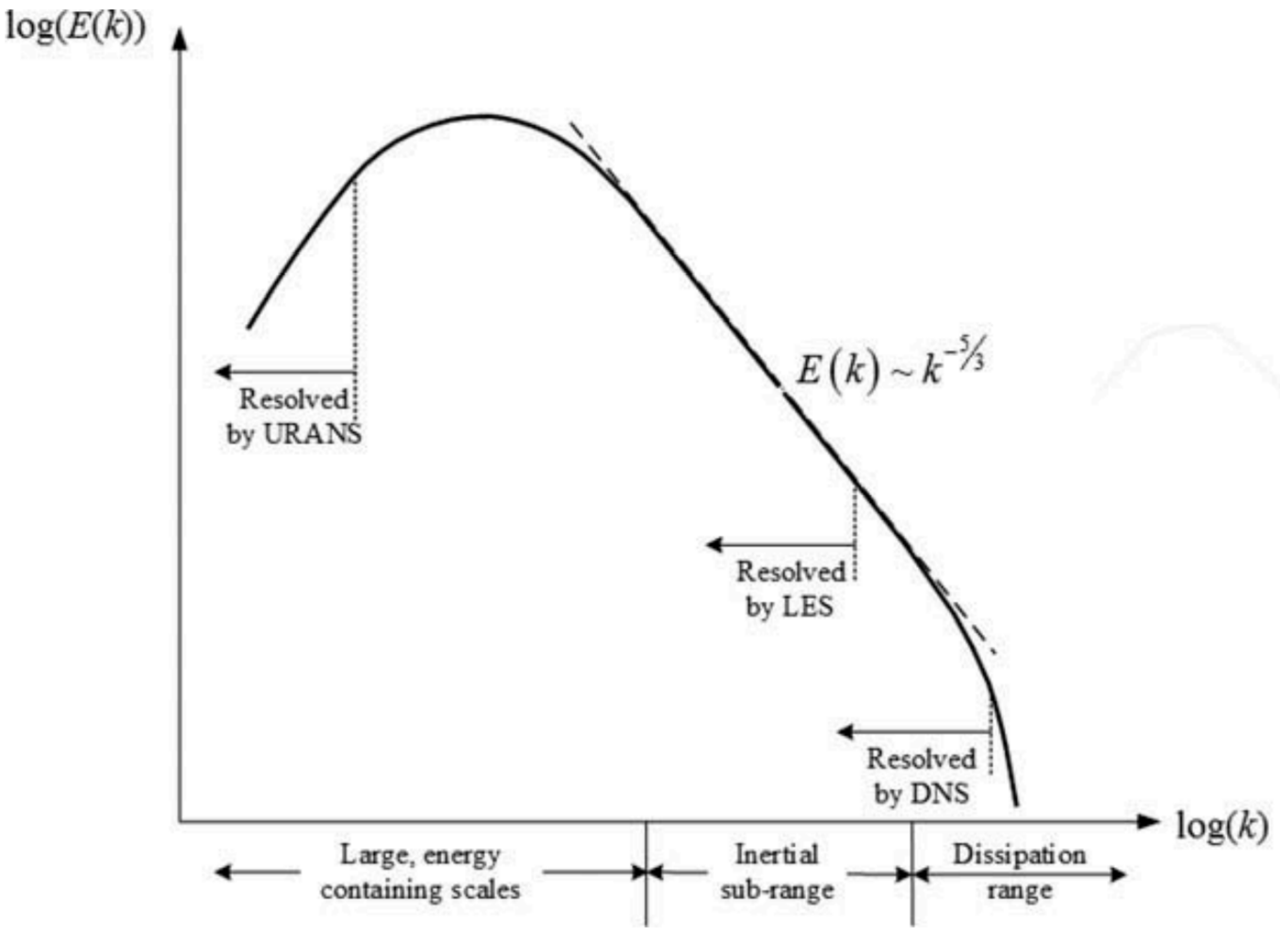

Figure 3.3. Graphical representation of energy distribution in turbulent flow across different wave numbers

3.2 Implemented approach

A systematic procedure was undertaken to address the research objectives of this study. In order to study the entrainment of the saltwater in the Haringvliet, it was necessary to first develop a validated model that could produce trusted results. For this reason, the physical model by Debler and Armfield (1997) was chosen as a reference case for validation. Kirkpatrick et al. (2012) were able to validate the model of Debler and Armfield (1997) using LES model incorporating high order solver schemes (third-order time and fourth-order space). However, LES is computationally demanding leaving the need for exploring other approaches to reduce the computational cost. Therefore, the process began with the development of a 2DV model using the RANS approach with an appropriate turbulence model. This was followed by comprehensive testing under various parameters and turbulence models to check the performance of the numerical model. Subsequently, a 3D model with DES approach was created, and further testing was conducted to evaluate its performance. The results were compared against the lab results of Debler and Armfield (1997) for validation, leading to the selection of the most effective model in terms of representation of the entrainment rate of saltwater leaving the cavity. This process then allowed for the development of a field scale model using the settings of the best-performing lab-scale model. Finally, the results of the field model were checked against the field data to evaluate its performance in quantifying the entrainment rate of saltwater in a large scale model. This approach, as shown in Figure 3.4, ensured a systemic progression throughout the research resulting in a good understanding of the capability of different models to accurately capture the entrainment rate of saltwater using STAR-CCM+ software. The methodology explained for developing the model in the following sections concerns the development of the 2D RANS model and the adjustments implemented to the models in the 3D lab scale and the Haringvliet model cases are discussed in sections 3.7 and 3.8. To streamline the presentation of the sections and avoid repetition, several figures are employed to depict both the 2D and the 3D lab scale models. Distinctions between the two models are highlighted and reported specifically in the contexts where they are applied.

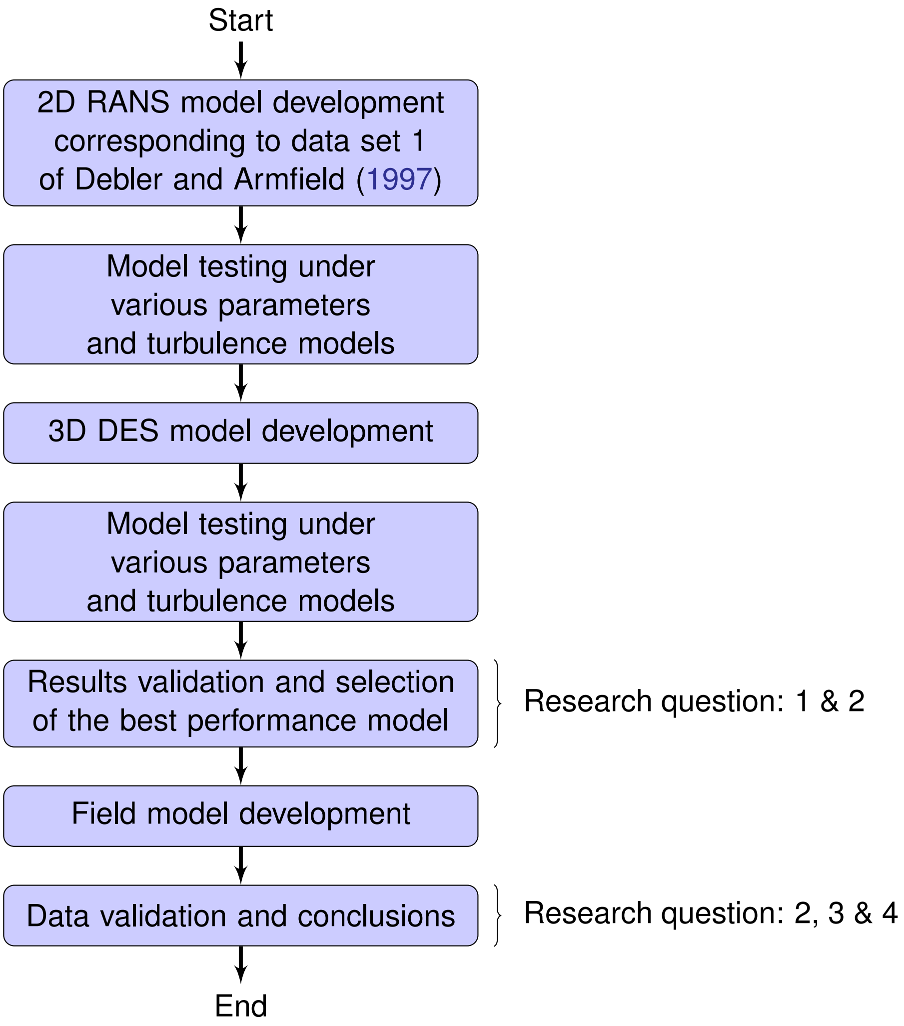

Figure 3.4. Overview of the steps taken to address the research questions of this study

3.3 Description of the physical lab scale model

In order to trust the results of the numerical model in calculating the entrainment of saltwater from a cavity, it is essential to directly compare it with the observations from a physical model. The physical model that has been selected for this validation process is one that has been developed by Debler and Armfield (1997). A visual representation of the cavities examined by the authors is shown in Figure 2.1.

The experiment of Debler and Armfield (1997) was conducted in a flume, measuring 11 meters in length and 0.25 meters in width. This setup involved the fitting of a false bottom into an adjustable opening in the flume to configure various cavities with different geometries, all having a consistent depth of 0.15 meters. These cavities were filled with saline solutions of varying specific gravities, determined by the weight of added salt to known volumes of water, and confirmed through density measurements. To initiate the experiments, dyed saline solution was gradually introduced at the cavity's bottom, while water from a hose, previously passed through flow measuring devices and a quick opening valve, was simultaneously introduced at the upstream end of the flume. This created a flow that passed over the cavity and exited through a downstream weir. The water was released 5 meters upstream of the cavity indicating that the flow was fully developed by the time it passed through the cavity. The experiments included a wide range of flow rates, from laminar to turbulent, and were monitored, photographed, and analyzed to gain insights into the flow dynamics and associated physical mechanisms. Finally, the data set selected for validating the numerical model corresponds to data set number 1 from the work of Debler and Armfield (1997) which corresponds to the dimensions of the model developed in this study shown in Table 3.1.

Table 3.1. Parameters of the lab scale numerical model corresponding to experimental data set 1 of Debler and Armfield (1997)

Parameter	**Value**
Density difference $\Delta\rho$ (kg/m^3)	2
Channel velocity V (m/s)	0.08
Froude number Fr_d	1.47
Reynolds number Re	5400
Richardson number Ri_0	0.21
Cavity aspect ratio L_1/H	6.93
Angle α_1 (degrees)	33.3
Angle α_2 (degrees)	33.3
Channel depth D (m)	0.067

3.4 Description of the CFD model set up

3.4.1 Software selection

The CFD model was employed in the STAR-CCM+ software, version 2021.2 (16.04.007-R8), to conduct simulations of the flushing process involving the interaction of saltwater and freshwater within a cavity. This software was selected as the description of the buoyancy-term in the Navier-Stokes equations and $k-\varepsilon$turbulence models have been validated by Deltares. The numerical approach employed the Finite Volume Discretization method, a robust method for solving fluid flow problems offering a balance between accuracy and computational cost (Surana et al., 2007; Zawawi et al., 2018). The approaches implemented were 2DV RANS and 3D DES. In the 2D RANS model, the equations of mass conservation, momentum, and turbulence were solved with the Reynolds-averaging approach, providing insights into the time-averaged flow behaviour. Whereas, the 3D DES model captured both the resolved large-scale turbulence and the unresolved small-scale eddies, offering a more comprehensive representation of the turbulent flow dynamics. This is because DES approach implements RANS near the boundaries and LES away from them. These models were essential in understanding the dynamics of the flow that results in the entrainment of saltwater.

3.4.2 Geometry of the cavity

The model was developed as shown in Figure 3.5. The model had a channel depth (D) of 0.067 meters and a cavity depth (H) of 0.15 meters, with slopes at both ends of the cavity inclined at an angle of 33.3°. To expedite computational processes, the numerical model maintained a shorter channel length of 1 m compared to the 5 m observed in the physical experiment upstream of the cavity. To compensate for this reduction, a pre-simulation was conducted before the model run to confirm the attainment of fully developed flow at the model inlet. This approach ensured the avoidance of additional computational expenses associated with extending the channel length. The pre-simulation method is explained in sections 3.4.3 and 3.4.5

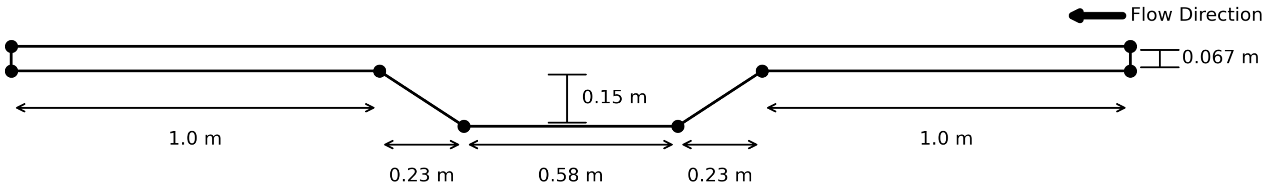

Figure 3.5. Dimensions of the model

3.4.3 Boundary conditions

Prior to generating a numerical solution for the system of partial differential equations of the fluid problem, the boundary conditions must be defined as they direct the fluid flow motion. The usual boundary conditions in CFD models include the Axisymmetric, the No-Slip, the inlet, the outlet, and the Periodic boundaries. Figure 3.6 shows an example of fluid flowing from the left to the right in a pipe where different boundary conditions are set. At the left, an inlet boundary is specified where the velocity of the fluid is set manually, whereas, at the exit of the pipe, the outlet boundary is set with the purpose of retaining constant properties of the fluid. The No-Slip boundary is set at the upper wall of the pipe which signifies that the fluid velocity is zero, and at the middle of the pipe, a horizontal axis is specified called an axisymmetric boundary which indicates similar fluid properties across that axis (Zawawi et al., 2018).

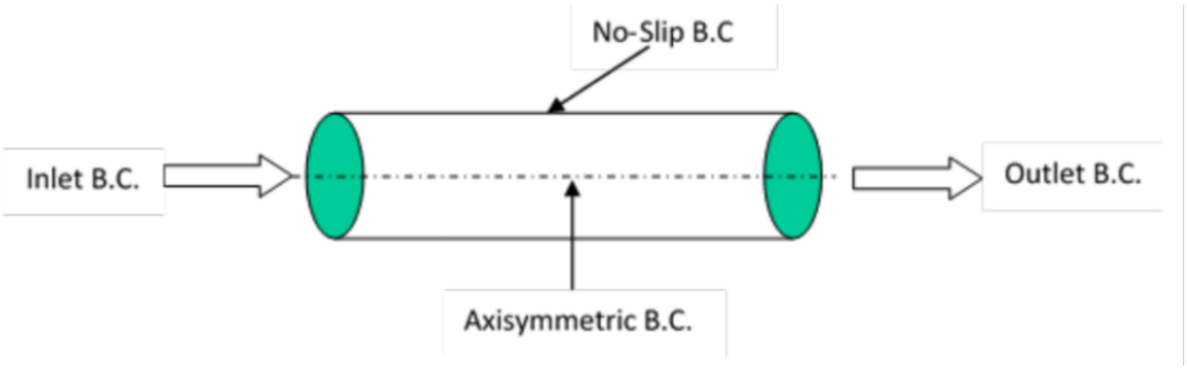

Figure 3.6. Boundary condition types in case of fluid flowing through a pipe (Zawawi et al., 2018)

The boundary conditions imposed on the lab scale model are illustrated in Figure 3.7. On the figure's left side, the cavity model is presented, whereas, on the right, a pre-simulation (presim) model is shown. The geometry of the presim is an extension of the cavity channel's geometry, ensuring that the number of cells on the adjacent sides of the cavity and the presim were identical and perfectly aligned with one another.

The boundary conditions of the model are presented in Table 3.2. The model has a solid wall at the bottom enforcing the no-slip condition resulting in a zero velocity at the wall. Conversely, the upper boundary was defined as a rigid lid with slip condition ensuring no friction at the upper boundary. Finally, the inlet was defined as a velocity inlet and the outlet was defined as a pressure outlet with 0 pascals pressure value imposed.

The presim was used to develop the velocity profile used at the cavity inlet. The presim has identical boundary conditions as those defined in the cavity with the exception that the presim velocity inlet and velocity outlet were coupled using a fully developed interface that used a mass flow rate to produce a fully developed velocity profile. The velocity profile was exported to an excel file, which was then utilized to define a fully developed flow at the cavity inlet, right from the start of the main simulation. Along with the velocity profile, the turbulent kinetic energy, turbulent

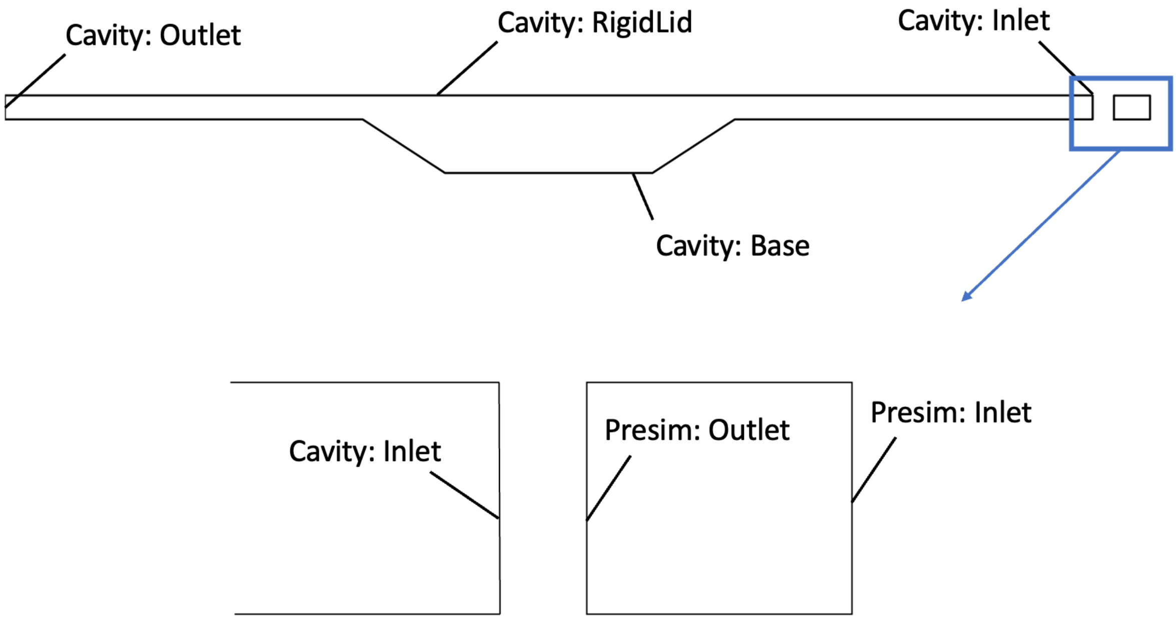

Figure 3.7. Lab model boundary conditions

Table 3.2. Boundary conditions of the lab CFD model

Boundary	**Specification**
Bottom boundary	Solid wall with no-slip condition
Upper boundary	Rigid lid with slip condition
Inlet	Velocity inlet
Outlet	Pressure outlet

dissipation rate and Reynolds stresses (in the case of 3D simulations) were transmitted from the velocity outlet of the presim to the velocity inlet of the cavity after the presim run was completed. This approach was carried out in steps where first the presim was run till the velocity profile was developed. Then, the cavity was run with the velocity input from the presim output.

3.4.4 Mesh generation

In the Star CCM+ software, the meshers employed to discretize the physical domain into individual cells for the model consisted of the Surface Remesher, Trimmed Cell Mesher, and Prism Layer Mesher. These are tools that were used to subdivide the model domain to facilitate the numerical analysis. The objective was to produce a high-quality mesh that accurately represented the cavity geometry and fluid flow behaviour. The Surface Remesher option was utilized to refine the surface mesh. Next, the Trimmed Cell Mesher was employed to generate the volume mesh. A base size of 0.003 m was selected for the cell size to strike a balance between computational efficiency and capturing important flow features. This value was determined by Ruiz (2022) after careful consideration of the anticipated flow behaviour, the computational time, and the desired level of resolution. Finally, the Prism Layer Mesher was applied to create boundary layer meshes. The prism layers are essential for capturing the flow phenomena near solid surfaces, such as boundary layer development and wall shear stress distribution. In this case, a seven-layer prism structure with a minimum thickness of 10% of the base size and with a prism layer stretching of 1.5 was employed as shown in Figure 3.8. The purpose of this configuration was to have small cells near the boundaries to capture the anticipated steep velocity gradients while maintaining a low computational cost. Finally, both the presim and the cavity geometries were both meshed in the same file to ensure that all the cells from the presim outlet align perfectly with the cells at the interface of the cavity inlet as seen in Figure 3.8. This process eliminates errors in transforming the velocity profile from the presim to the cavity. This configuration resulted in a total of 43,107 cells for the cavity in the 2D case in the 3 mm mesh size model.

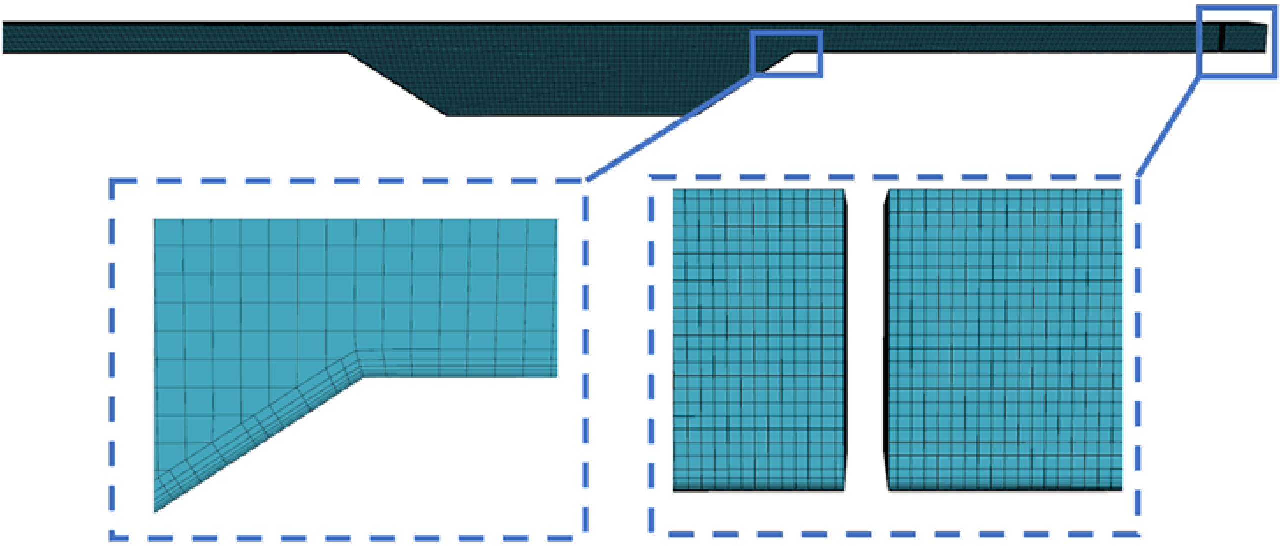

Figure 3.8. Model mesh

3.4.5 Water velocity profile

The inflow velocity at the inlet was transitioned to a fully developed state through a presim section as shown in Figure 3.7. This methodology ensures that the velocity of the flow upstream of the cavity is consistent as shown in Figure 3.9 and further quantified in Figure 3.10.

The fully developed velocity profile extracted from the presim outlet was used as an input for the cavity inlet as explained in section 3.4.3. This fully developed profile was established by simulating a mass flow rate of 5.36 kg/s at the presim inlet and allowing the presim to run till a fully developed velocity profile was achieved. The mass flow rate in this case converts to a

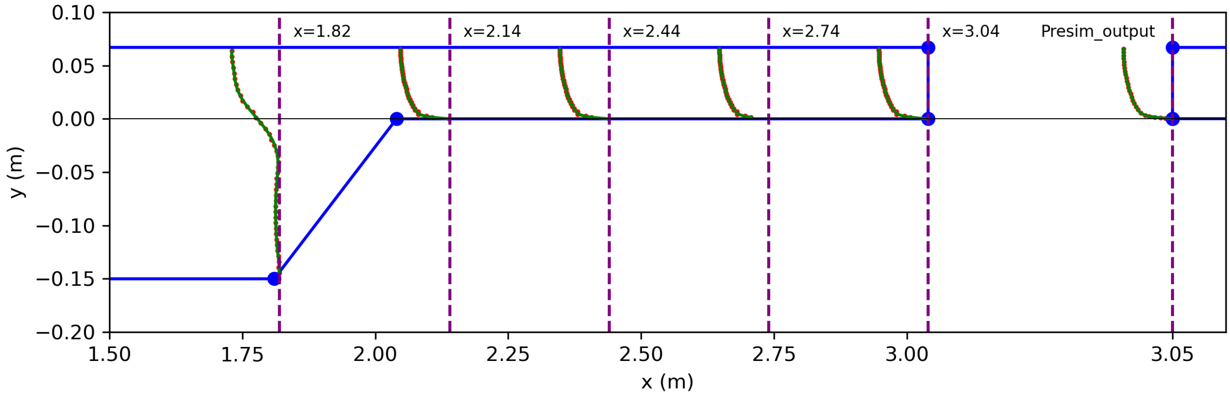

Figure 3.9. Sketch of velocity profiles along the model

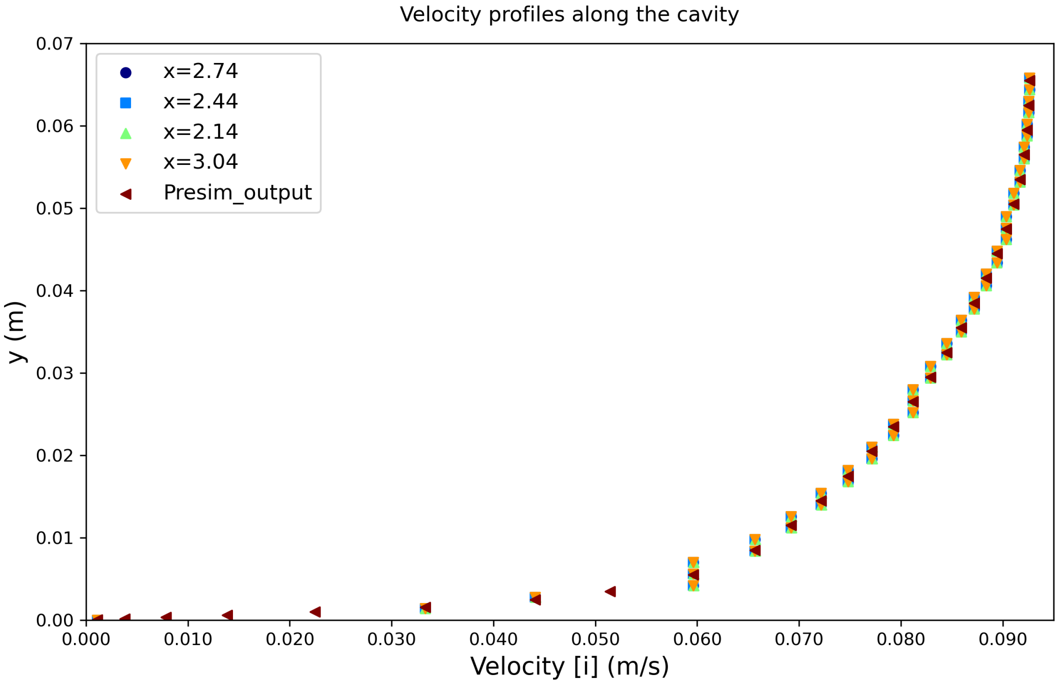

Figure 3.10. Velocity profiles along cavity

depth-averaged velocity of 0.08 m/s which aligns with the flow velocity used in the experiment of Debler and Armfield (1997). The implementation of this strategy demonstrates an effective method to achieve desired flow conditions while optimizing computational resources. Furthermore, Kirkpatrick et al. (2012) explained that the experiment of Debler and Armfield (1997) included a velocity ramp up over 90 seconds. Therefore, the velocity input at the cavity inlet was increased from 0% to 100% of the fully developed velocity profile over a period of 90 seconds using Equation 13 to match the conditions of the lab experiment.

$$V_{\text{ramp}}(t) = \frac{t}{90} \cdot V_{\text{input}} \quad \text{for } 0 \leq t \leq 90 \tag{13}$$

Where $V_{\text{ramp}}(t)$ represents the velocity at the inlet as a function of time t, t is the time in seconds, 90 is the total duration of the velocity ramp-up in seconds and V_{input} represents the input velocity, which is the fully developed velocity profile exported from the presim outlet.

3.4.6 Saltwater definition

Saltwater density was defined using a scalar introduced as a salinity variable, which was then added to the density of freshwater. The method used for defining the saltwater in the model was based on the UNESCO formulation. The UNESCO formulation calculates the density of saltwater by adding salinity (S) to the Standard Mean Ocean Water density (ρ_{SMOW}), as shown in Equation 14. This approach incorporates temperature-dependent variations, calculating density (ρ) as a function of temperature (T) and salinity (S) via a polynomial model (R. Massel, 2015; UNESCO, 1981):

$$\rho = \rho_{SMOW} + \alpha S + \beta S^{1.5} + \gamma S^2 \tag{14}$$

where α, β, and γ are coefficients determined based on temperature. Full parameters definition is provided in Appendix A.

Provided that the temperature is constant in this study, the UNESCO formulation can be made into a simplified method, where the desired salinity difference is added to the freshwater density to obtain the saltwater density. As illustrated in Equation (15), this method involves introducing a scalar variable, equivalent to salinity (S), and adding it to the density of freshwater (ρ_{fw}) to obtain the saltwater density (ρ_{sw}). Hence, this method is a simple and straightforward method.

$$\rho_{sw} = \rho_{fw} + S \tag{15}$$

The UNESCO method tends to produce more accurate density values, particularly in scenarios characterized by significant temperature variations. However, for this study, temperature data was not taken into account, as no temperature data was available for result validation. When considering a fixed temperature, the primary distinction between the two methods lies in the salinity requirement. The UNESCO method requires an input for salinity, which is subsequently utilized to derive a final density difference that deviates from the initial input, making it a more challenging method than the scalar method to precisely achieve the required density difference for this study. Conversely, the simplified approach of inputting the density difference as a scalar proves to be more accurate in this case, given that the study specifically targets a density difference of 2 kg/m^3. Moreover, both the UNESCO formulation and the scalar method exhibit linear relationships between salinity and seawater density under fixed temperature, as depicted in Figure 3.11. This relationship is characterized by nearly identical slopes in the density-salinity relationship under fixed temperature conditions. Given our specific target saltwater density and the absence of temperature variation in our study, the simplified method presented in Equation 15 was a preferable choice, offering ease of application with similar output.

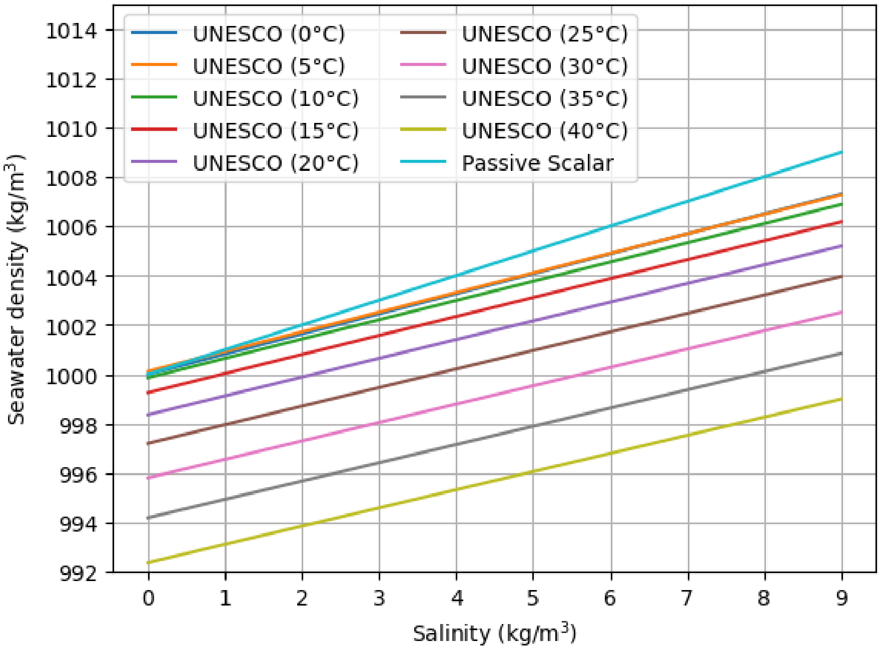

Figure 3.11. Salinity definition using the UNESCO and the scalar variable methods

Finally, prior to starting the main simulations, the sensitivity of the model to the saltwater method of definition was examined by investigating its response to different salt concentrations. This step allowed for the verification of the model's behaviour against expected trends. Subsequently, the performance of the model was evaluated under different configurations of mesh sizes, turbulent Schmidt numbers and turbulence models.

3.4.7 Turbulence models

The closure models used in the 2D RANS and the 3D simulations were the $k-\varepsilon$, the $k-\omega$ and the Spalart-Allmaras. Those models provide important approximations needed to solve turbulence equations. Closure models provide a controllable way to capture turbulence effects, considering the complex nature of turbulent fluctuations. The 2D RANS simulations used the $k-\varepsilon$ and $k-\omega$ while the 3D DES simulations investigated the $k-\varepsilon$, $k-\omega$ and Spalart-Allmaras models. It should be noted that all 2D and 3D simulations were initially run using the RANS (Reynolds Averaged Navier-Stokes) equations for presim run to create the fully developed velocity profile as explained in section 3.4.5.

3.4.8 Data monitoring in the simulations

Three different methods were used to extract the results throughout the simulation. Those methods involved line probes, plane sections and isosurfaces. Line probes consist of one-dimensional lines that extract results along a single linear trajectory. Plane sections, on the other hand, involve slicing the model with a two-dimensional plane. Iso-surfaces, in contrast, are employed for three-dimensional representations of specific values or ranges of a variable of interest. These surfaces are defined by constant values of the variable and are commonly used to visualize regions where a particular property or condition is present. The three types of derived parts are shown in Figure 3.12.

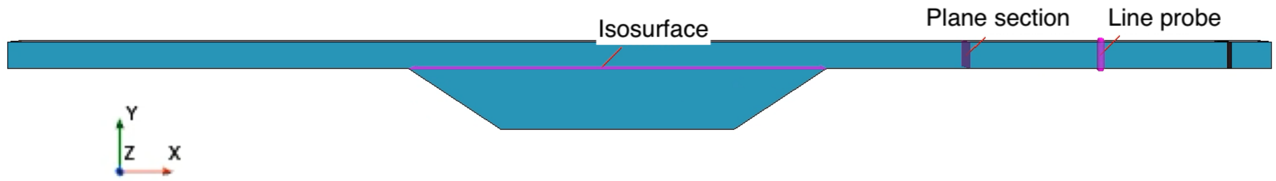

Figure 3.12. Schematic representation showing the isosurface, plane section, and line probe definitions within the model domain

Line probes were employed to gather data over time, enabling the investigation of velocity profiles and salinity concentration gradients within the central region of the cavity along the y-axis direction at various x locations along the cavity as shown in Figure 3.13. Similarly, the plane sections were employed across the yz plane of the cavity at different x-axis locations to observe salinity concentration variations. Furthermore, they were used to investigate velocity profiles for any anomalies within the channel, as explained in section 3.4.5. Lastly, the iso-surface was utilized to monitor the distance from the cavity base to the interface that separates the saltwater from the freshwater. This information indicates the remaining amount of saltwater in the cavity over time.

Figure 3.13. Line probes placement along the cavity. Locations of the line probes relative to the cavity downstream end (Cavity inlet: 3.04 m, A: 2.74 m, B: 2.44 m, C: 2.14 m and D: 0.84 m)

3.4.9 Calculating the entertainment rate

The interest of this study was to compute the rate at which the saltwater is drawn out of the cavity due to dynamics induced in the cavity by the freshwater inflow. This rate is known as the entrainment rate.

To be able to compare the results of this study to the results presented in Debler and Armfield (1997), the entrainment rate, denoted as E, is computed using the dimensionless expression presented in Equation 16 as derived by Debler and Armfield (1997).

$$E = \frac{\left(\frac{Ue}{V}\right)}{Fr_d^2} \cdot 10^4 \tag{16}$$

Where Ue is the entrainment velocity, V is the velocity of the freshwater inflow to the cavity.

The entrainment velocity is obtained by computing the change in height h from the bottom of the cavity to the interface at the top of the saltwater remaining in the cavity over time t as shown in Equation 17.

$$U_e = -\frac{dh}{dt} \tag{17}$$

The theoretical entrainment rate was calculated using Equation 12 with a mixing coefficient K of 0.001 (Debler & Armfield, 1997).

3.5 Methods of results validation and error quantification

To validate the model's outputs against Debler and Armfield (1997) findings, the following methods for results validation and error quantification were used:

1. **Qualitative analysis of turbulence and flow behaviour :** Snapshots of the simulations were captured at various time intervals. These snapshots are compared qualitatively to the observations of Debler and Armfield (1997) to examine the turbulence characteristics and flow behaviour throughout the simulation.
2. **Quantitative entrainment rate comparison:** The progression of the entrainment rate over time is computed, see section 3.4.9, and compared against corresponding figures from Debler and Armfield (1997). This offers a direct comparison of the entrainment rate trends between the experimental results and the numerical results.
3. **Error quantification using RMSE:** The experiment by Debler and Armfield (1997) produced discrete data points for dataset 1a (refer to Figure 2.4), in contrast to the continuous results from the numerical model. For RMSE computation, the entrainment

rates at matching interface heights from the experimental data were selected for comparison. The Root Mean Square Error (RMSE), as shown in Equation 18, is calculated using the observed values y_i from the experiment, and the predicted values $\hat{y}_i$ from the numerical model. The equation involves summing the squared differences between these observed and predicted values for each of the N data points, where N is the total number of data points, and then taking the square root of the average of these sums.

$$RMSE = \sqrt{\frac{1}{N}\sum_{i=1}^{N}(y_i - \hat{y}_i)^2} \tag{18}$$

3.6 Overview of changes implemented to study the performance of the model

In this subsection, an overview of the various alterations made to assess the model's performance is presented. The simulations are presented in Table 3.3. Seven distinct cases were considered for each of the 2D RANS and 3D DES simulations, with variations focusing on the model performance under the influence of the most influential model choices which were the closure model, the Schmidt number and the mesh size. While the 2D RANS included $k - \varepsilon$ and $k - \omega$ models, the 3D DES simulations included $k - \varepsilon$, $k - \omega$, and Spalart-Allmaras models. Also, the 6 mm model was eliminated from the 3D simulations to reduce computational time. The trend of results was already evident from the 2D model without the need for the 6 mm results. Therefore, the 12 mm simulation was found sufficient for showing the trend in results for the 3D model.

The base case simulation was defined with a time step of 0.1 seconds and a mesh size of 3 mm. This case had a Courant number of 2.6. However, STAR-CCM+ efficiently manages various Courant number values through its adaptive solver algorithms, which maintain stability and accuracy by dynamically adjusting under-relaxation factors and utilizing sophisticated time-stepping techniques as required. The sensitivity of the performance of the model was checked against several cases with varying Courant numbers which resulted in a close level of performance for all the cases (refer to Appendix F). Furthermore, the flow was defined with the same conditions in all the 2D and 3D lab scale cases. Therefore, all lab scale cases had the same values of Fr, Ri_0 and Re which were 1.47, 0.21 and 5360 respectively.

3.7 Numerical model adjustments for Lab scale 3D transition

This section describes the modifications made when transitioning from the 2D to the 3D model with respect to the methodology explained in the previous sections. Transitioning to a 3D model entails adding an additional dimension along the z-axis. This extension in the z-direction is termed

Table 3.3. Overview of the variations in the 2D RANS and 3D DES simulations

Case ID	**Closure model**	**Turbulent schmidt number**	**Mesh size (mm)**
RANS1	$k - \varepsilon$	1	3
RANS2	$k - \varepsilon$	1	1.5
RANS3	$k - \varepsilon$	1	6
RANS4	$k - \varepsilon$	1	12
RANS5	$k - \varepsilon$	0.7	3
RANS6	$k - \varepsilon$	1.2	3
RANS7	$k - \omega$	1	3
DES1	$k - \varepsilon$	1	3
DES2	$k - \varepsilon$	1.3	3
DES3	$k - \varepsilon$	6	3
DES4	$k - \varepsilon$	1	1.5
DES5	$k - \varepsilon$	1	12
DES6	$k - \omega$	1	3
DES7	Spalart-Allmaras	1	3

the "breadth" of the model. To optimize the computational efficiency while allowing sufficient space for the turbulence within the model to develop, the boundaries on both sides of the model in the z-direction are coupled using a symmetry plane. This allows the model to be modelled with a narrower breadth and still retain the effects of a wider breadth. Using this method, the breadth of the cavity was set to 0.0625 m which corresponds to one-fourth of the cavity breadth in the physical model. This ratio was chosen to establish a consistent scaling ratio, facilitating potential future research extensions that may build upon this thesis. This configuration resulted in a total of 949,304 cells for the 3 mm mesh size model. The symmetry plane enables the model's breadth to simulate an infinitely extended cavity along the z-axis. Such an approach is advantageous because it provides ample space for vortices to evolve without necessitating an expansion in the model's breadth, which would substantially elevate computational expenses. This approach was motivated by the study of Kirkpatrick et al. (2012) where the authors showed that the use of a periodic boundary for the wall resulted in entrainment rates that aligned well with the observations and they explained that the use of this boundary did not change the basic physics of flow in the model.

Unlike the 2D model where only RANS was incorporated, the 3D model utilized DES with different turbulence closure models such as k-ε, k-ω, and Spalart-Allmaras. These models were tested to improve the accuracy of the model predictions and account for the complex turbulent flow phenomena occurring during the flushing of saltwater from the cavity.

3.8 Description of the Haringvliet

3.8.1 Water operation at the Haringvliet

The Haringvliet, which was previously an estuary in the Rhine-Meuse delta as illustrated in Figure 3.14, underwent a significant transformation in 1970. This change occurred when it was sealed off with floodgates, a key component of the Deltaworks initiative, aimed at protecting the southwestern region of the Netherlands from flood risks. Currently, the Haringvliet serves as one of the two main channels in the western Netherlands, facilitating the discharge of water from the Rhine and Meuse rivers into the North Sea. The other primary channel is the Rotterdam Waterway, maintaining an open connection with the sea. The Haringvliet floodgates are designed to control the outflow of water towards the sea while simultaneously preventing seawater from entering inland. Essentially, this implies that they prevent any potential flooding from the sea and allow only a controlled release of river water during low tides. When river water levels are low, the gates remain completely closed, even at times of low tides. In such situations, water is diverted to the Rotterdam Waterway to prevent saltwater ingress. Following extensive deliberations, a high-level political decision was made in the Netherlands to allow a controlled amount of seawater back into the Haringvliet (Huismans, 2016; Kranenburg et al., 2023). The purpose of this decision was to enhance fish migration, especially aiding them in reaching their upriver spawning areas, and thus supporting ecological objectives. To implement this, a managed introduction of seawater is achieved by partially opening a few of the gates during times of high tide.

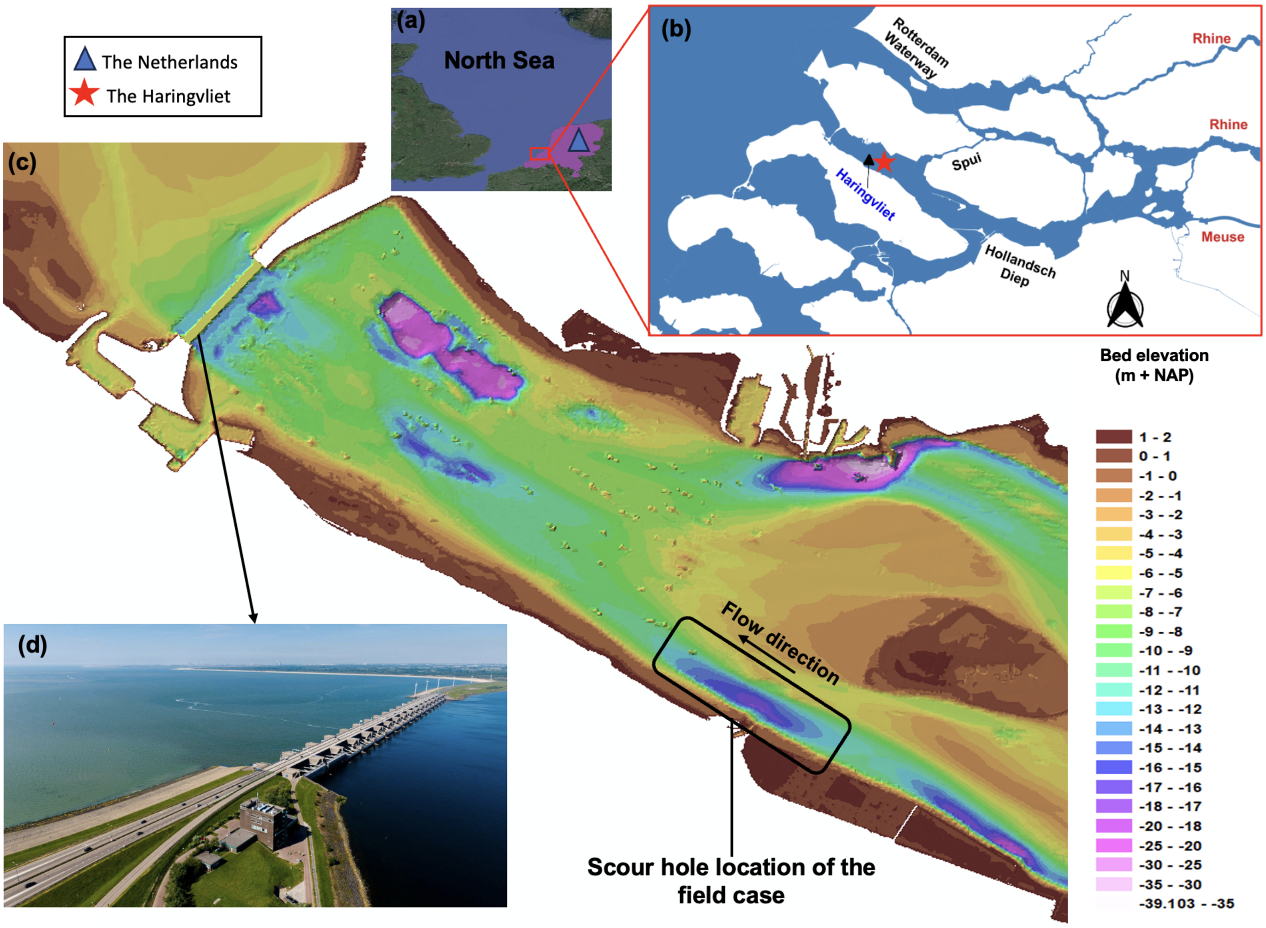

Figure 3.14. The Haringvliet location. a) position of the Haringvliet relative to the Netherlands; b) The Haringvliet map, retrieved from PDOK datasets; c) Bathymetry of the Haringvliet and location of the scour hole selected for modelling; d) Haringvliet sluices, picture retrieved from Rijkswaterstaat website. The arrow indicates the flow direction during flushing events.

3.8.2 The Haringvliet characteristics

The average depth of the Haringvliet is approximately 7 meters, with significant variations in depth as indicated by its bathymetry presented in Figure 3.14c. The formation of these deeper regions can be attributed to several factors, including historical tidal activities, erosion near structures like jetties, and activities related to sand mining. These factors collectively contribute to the diverse depth profile observed in the Haringvliet. The Haringvliet is isolated from the sea on its north-western side through a series of 17 double-door floodgates. These gates are capable of being raised from a sill depth of 5.50 meters below a reference level known as 'Normaal Amsterdams Peil' (NAP). The NAP, with a baseline of 0 meters, is approximately equivalent to the mean sea level of the North Sea. This structural feature of the Haringvliet is illustrated in Figure 3.14d.

The Haringvliet receives fresh water from the Rhine and Meuse rivers through the Hollandsch Diep, located at its south-eastern end. Additionally, the Haringvliet connects to the Rhine-Meuse delta through the Spui, situated on its northern side. These connections introduce tidal influences into the Haringvliet, leading to water level variations that can reach up to 0.50 meters at their maximum. Notably, the tidal range at the intake of the Rotterdam Waterway varies significantly, with a minimum of 1.0 meters during the smallest neap tides and increasing to 2.3 meters during the largest spring tides. Even greater fluctuations, reaching up to 3.0 meters, can be observed at the seaward side of the floodgates. Through its connections, the water levels in the Haringvliet are subject to changes caused by wind-driven water movements at sea. When there are intense events involving both tide and wind, the resulting flow towards the Haringvliet through the Rotterdam Waterway and Spui can occasionally result in saltwater entering the Haringvliet from the north, a phenomenon known as backward salinization (Huismans, 2016; Kranenburg et al., 2023).

3.8.3 The Haringvliet CFD model

This section outlines the adjustments undertaken when scaling the geometry of the CFD model from a lab scale to a field scale. Transitioning to a field scale model requires a broader and more complex spatial representation. The model setup is a 3D model following a similar process to that explained in section 3.7. However, the spatial resolution of the model in this case was much larger than that used for the lab scale model. The model represents a scour hole in the Haringvliet and extended to a total span of 2.5 km on the x-axis and 16 meters on the y-axis. The meshing method implemented for the Haringvliet model followed the methodology in section 3.4.4 with the difference in mesh size. The mesh size was 0.02 m (see Figure 3.15) and the breadth was 1 m resulting in a total number of 5,352,392 cells in the scour hole. The flow velocity was 0.16 m/s and included a velocity ramp up over 60 seconds. Therefore, the velocity input at the scour hole inlet was increased from 0% to 100% of the fully developed velocity profile over a period of 60 seconds. The model was run with a time step of 0.1 seconds resulting in a Courant number of 0.8. Furthermore, the Fr and Ri_0 were 0.60 and 4.82 respectively.

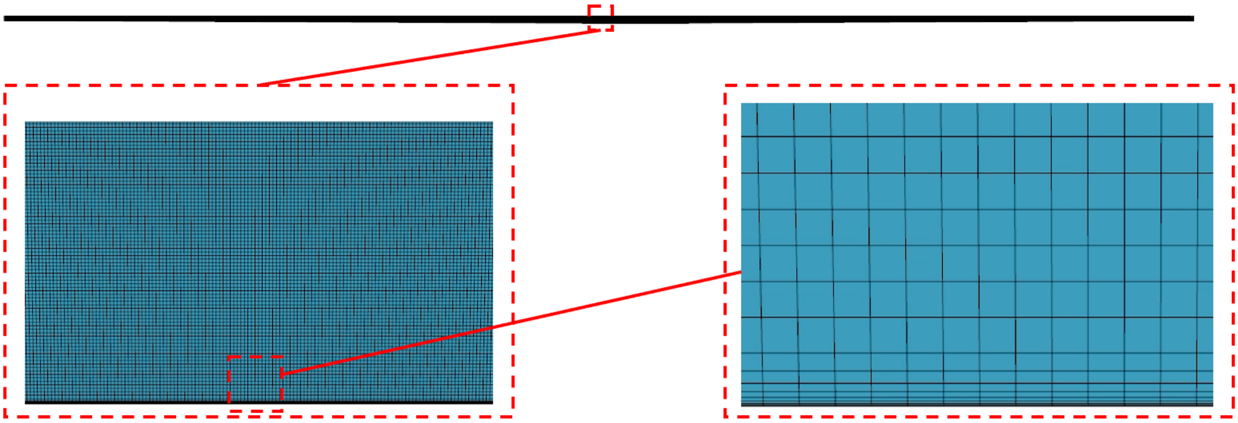

Figure 3.15. Haringvliet model mesh

3.8.4 Geometry of the scour hole

Building on the earlier description of the Haringvliet, this section focuses on the specifics of a particular scour hole selected for detailed investigation. As depicted in Figure 3.14, this scour hole is situated in the Haringvliet. The study utilizes a simplified model of the scour hole's geometry, as illustrated in Figure 3.16. The model encompasses a 2400-meter horizontal span, featuring a 100-meter channel on both sides of the scour hole. The scour hole itself stretches for 2300 meters in length. In terms of depth, the channel measures 10.5 meters upstream of the scour hole and 10.0 meters downstream, while the scour hole reaches a depth of 16 meters below the water surface.

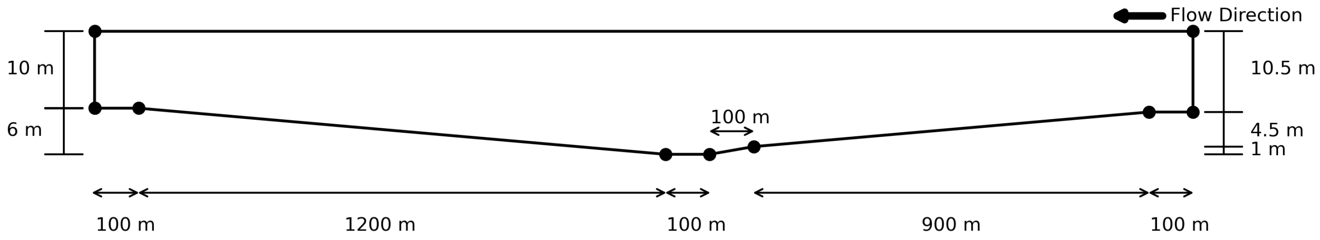

Figure 3.16. Scour hole geometry

3.8.5 Boundary conditions

The boundary conditions applied to the Haringvliet model are depicted in Figure 3.17. This figure shows the scour hole model on the left and the presim model on the right. The presim model's geometry is an extension of the upstream side of the scour hole channel. These boundary conditions are detailed in Table 3.4. At the model's bottom, a solid wall enforces a no-slip condition, leading to zero velocity at this boundary. In contrast, the top boundary is defined as a rigid lid with a slip condition to eliminate friction at this boundary. The walls are defined as symmetry planes. The scour hole upstream end is defined as a velocity inlet and the downstream end is defined as a pressure outlet with 0 pascals pressure.

Table 3.4. Boundary conditions of the Haringvliet CFD model

Boundary	**Specification**
Bed	Solid wall with no-slip condition
Upper boundary	Rigid lid with slip condition
Inlet	Velocity inlet
Outlet	Pressure outlet
Walls	Symmetry planes

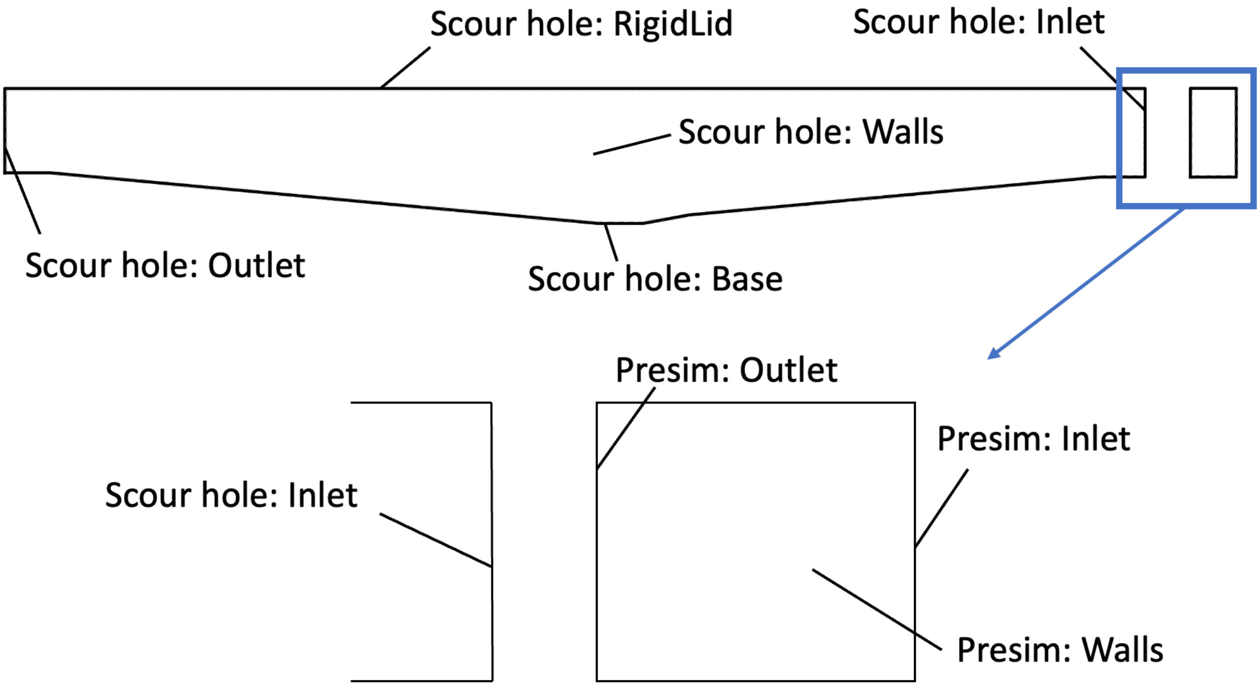

Figure 3.17. Haringvliet model boundary conditions

3.8.6 Data monitoring in the scour hole

The observation data of the Haringvliet are part of Work Package 3.2 of the SALTISolutions project and were provided for the validation of the CFD model in this study (see Appendix B for the raw data of the velocities). This data covers field data collected using Acoustic Doppler Current Profilers (ADCPs) and the Conductivity-Temperature-Depth devices (CTDs). Figure 3.18 shows the locations of the ADCPs and CTDs within the scour hole in the field. ADCP1 and ADCP2 were positioned 1290 meters and 1030 meters, respectively, away from the downstream end of the scour hole. Additionally, there were two CTD devices, CTD1 and CTD2, which were placed 1150 meters away from the downstream end of the scour hole. CTD1 was positioned at a depth of 10.3 meters while CTD2 was positioned at a depth of 12.5 meters. In the model, plane sections were established at the positions of the ADCPs and line probes were established at the positions of the CTD devices. The plane sections and line probes were implemented to replicate field measurement methods, enabling a direct evaluation of the results and the model's performance. The salinity data of the CTD was provided in PSU. Therefore, the data was converted to density using the relation 1 PSU = 1 kg/m^3 and added to the freshwater density using Equation 15 to obtain the saltwater density.

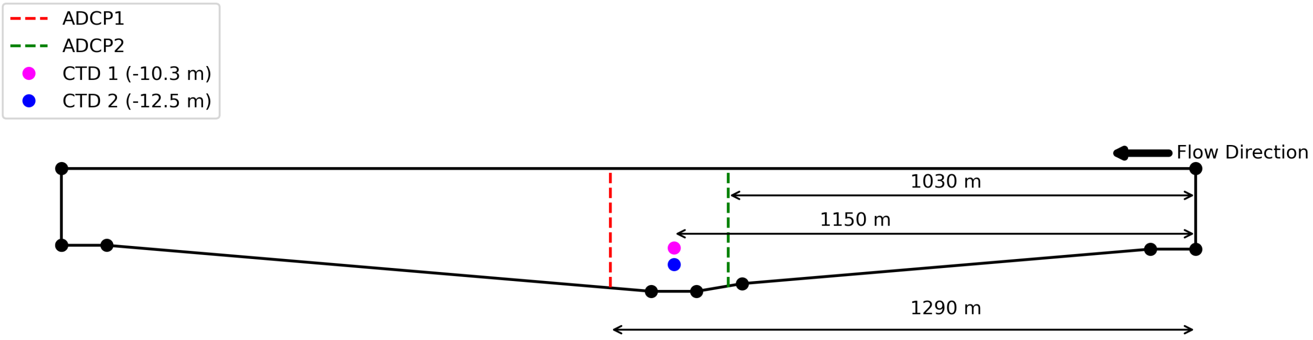

Figure 3.18. Location of the measuring devices within the scour hole

3.8.7 Comparing model results with field observations

The drop in saltwater level in the model was compared to the recorded saltwater level in the scour hole over time. The saltwater interface height was determined from the velocity profiles recorded using the ADCPs for the 17th of February 2023. The interface height was determined from the velocity profiles by identifying points where there was a sharp increase in velocity compared to its neighbouring bottom cell, indicating the presence of a freshwater-saltwater boundary at that point (refer to Appendix B for the velocities plots). This interface height was then plotted against time to visualize its temporal evolution. To further refine the representation, a moving average with a specified window of 10 consecutive data points was applied for calculating the average interface height, smoothing out minor fluctuations and emphasizing the overall trend as shown in Figures 3.19 and 3.20 for the interface heights at ADCPs 1 and 2 respectively.

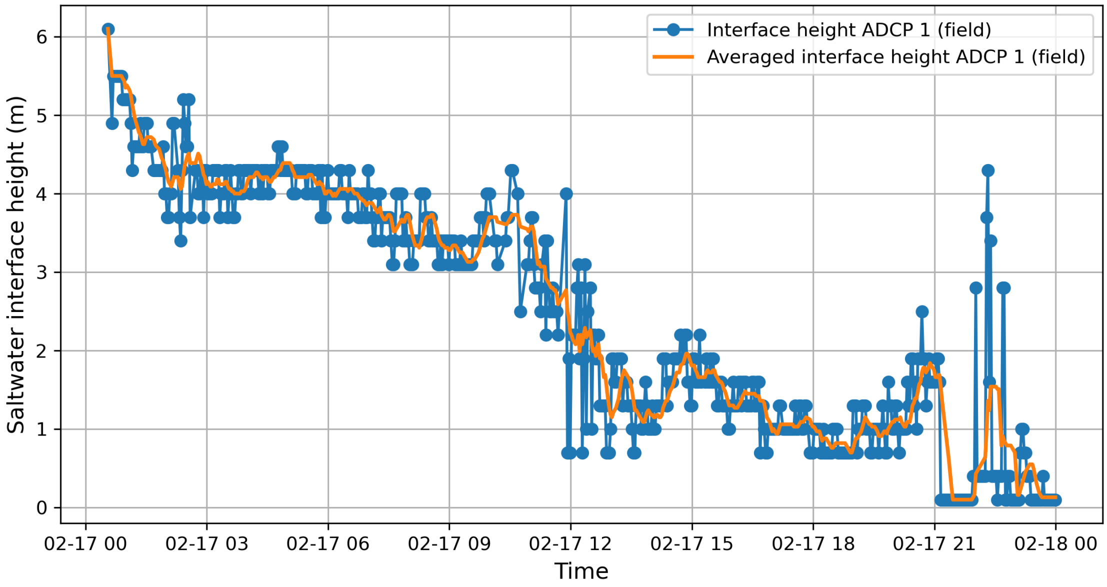

(a)

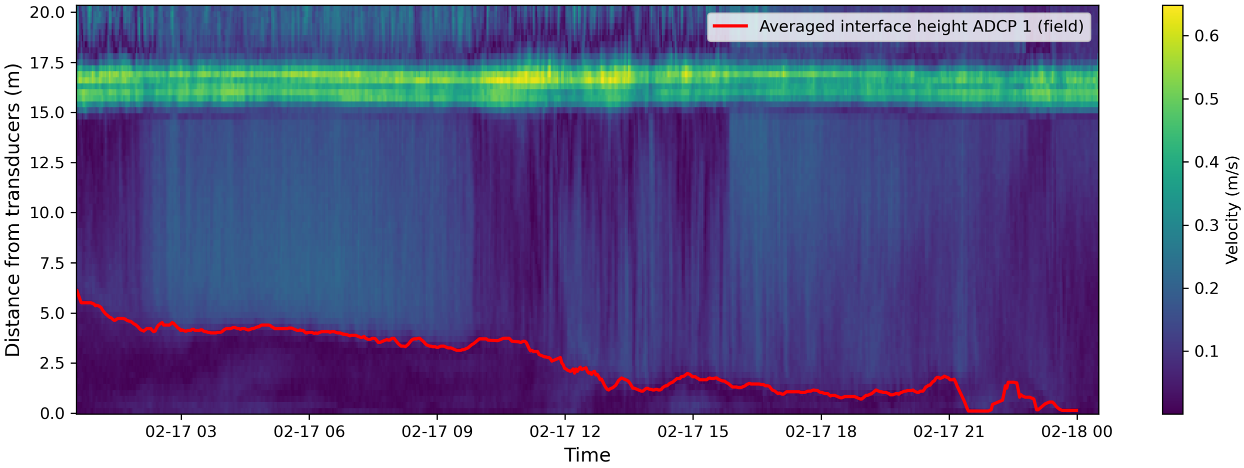

(b)

Figure 3.19. Estimated saltwater interface height and velocity measurements at ADCP1. (a) Averaged saltwater interface height estimated from the velocity profile; (b) Estimated interface height overlaid on field velocity measurements

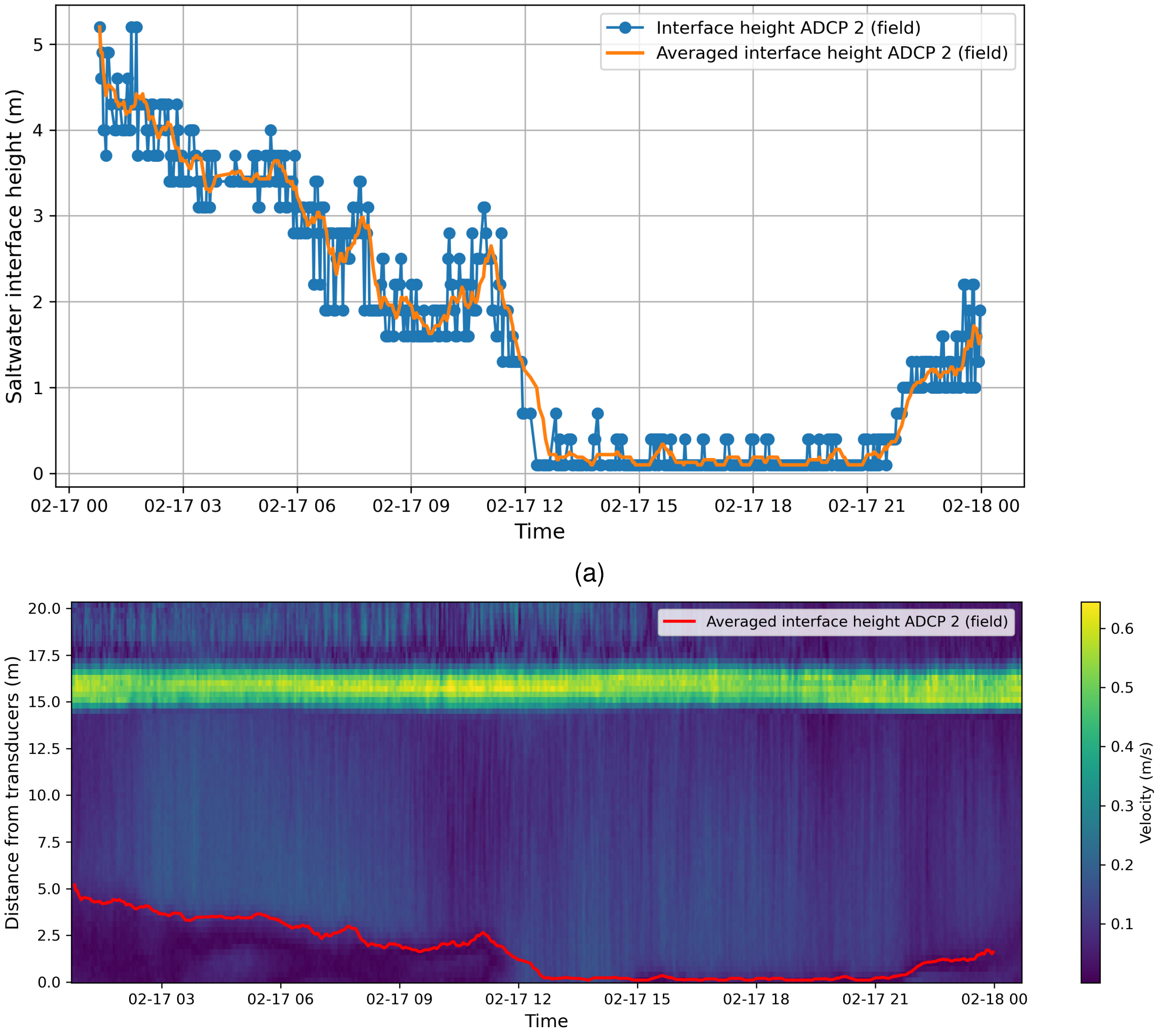

(a)

(b)

Figure 3.20. Estimated saltwater interface height and velocity measurements at ADCP2. (a) Averaged saltwater interface height estimated from the velocity profile; (b) Estimated interface height overlaid on field velocity measurements

4 Results

4.1 2D RANS lab scale model

4.1.1 Influence of mesh variation

The results of the 1.5, 3, 6, and 12 millimetres mesh sizes showed a close level of performance as indicated by their RMSE values in Figure 4.1a. While the results of the 4 cases showed relatively comparable performance, the 12 mm mesh had a slightly better performance when compared to the other mesh sizes. Specifically, for the mesh sizes of 1.5 mm, 3 mm, and 6 mm, the RMSE values were 5.75, 5.62, and 5.44, respectively whereas the model with the 12 mm mesh resulted in a lower RMSE value of 4.80. These results indicated a relatively close model performance across these mesh sizes. Interestingly, the larger mesh size of 12 mm resulted in a slightly lower RMSE value, suggesting a small improvement in the accuracy of the predictions as shown in Figure 4.1a.

The lower RMSE value for the 12 mm mesh model indicates a better entrainment rate of the saltwater as seen in Figure 4.2. For accurately resolving small-scale phenomena and capturing detailed flow features, a finer mesh with smaller element sizes is typically preferable and expected to increase the accuracy of the results. The coarser mesh is not an ideal choice of modelling as a large mesh size is not able to capture the small-scale vortices and eddies that are responsible for entraining the saltwater. Figures 4.1a and 4.2 show that there is no significant difference between the results obtained using 1.5 mm, 3 mm and 6 mm mesh sizes which indicates that mesh independence has been achieved at this stage. Furthermore, Kirkpatrick et al. (2012) used mesh sizes ranging between 5 mm to 2 mm over the cavity span indicating that a 3 mm cell size is an appropriate choice for this geometry in an LES simulation. Since the 3 mm mesh size fulfils the requirement for even a more demanding simulation such as LES and provides a good computational cost, the 3 mm mesh size was kept as the final choice for modelling the other phases of the lab scale simulations. This choice ensured that both the 2D RANS simulations and the 3D DES simulations receive a fair comparison that can clearly show the difference in performance between both methods.

4.1.2 Influence of the turbulent Schmidt Number

This section presents the performance evaluation for the turbulent Schmidt number using the 2D RANS k-ϵ model. The results showed that the entrainment rate decreases with increased turbulent Schmidt number. This is because a high Schmidt number forces the mass transport to reduce and the momentum diffusion to increase. This statement is supported by Figure 4.3 where it can be seen that a Schmidt number of 1.2 yielded lower entrainment rates than those observed for Schmidt numbers of 0.7 and 1.0.

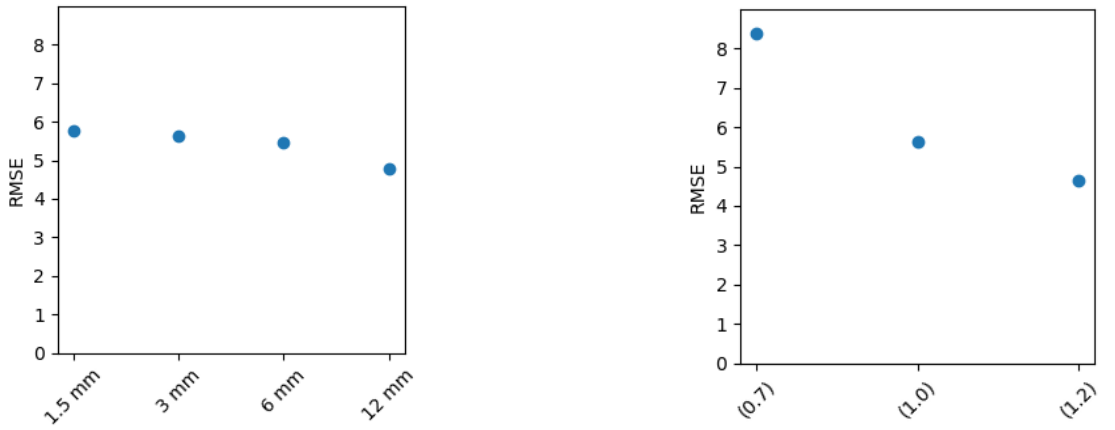

(a) 2D mesh variations

(b) 2D turbulent Schmidt number

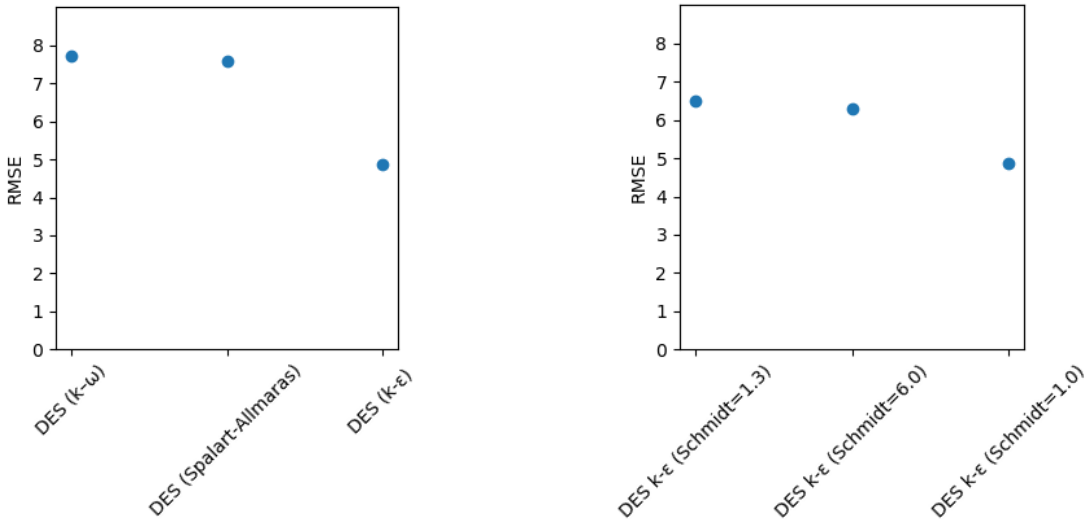

(c) 3D different closure models

(d) 3D turbulent Schmidt number

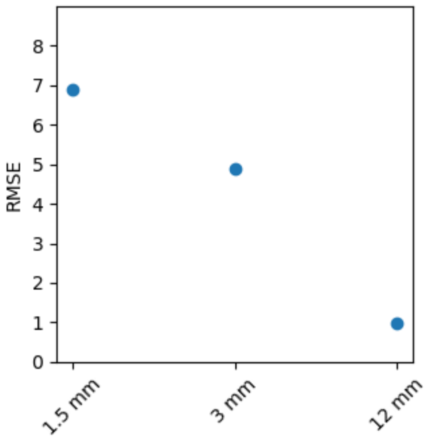

(e) 3D mesh variations

Figure 4.1. RMSE variations for different parameters

Higher turbulent Schmidt numbers result in a lower amount of saltwater being drawn out of the cavity and hence, reducing the entrainment rate. Since the entrainment rate increases with

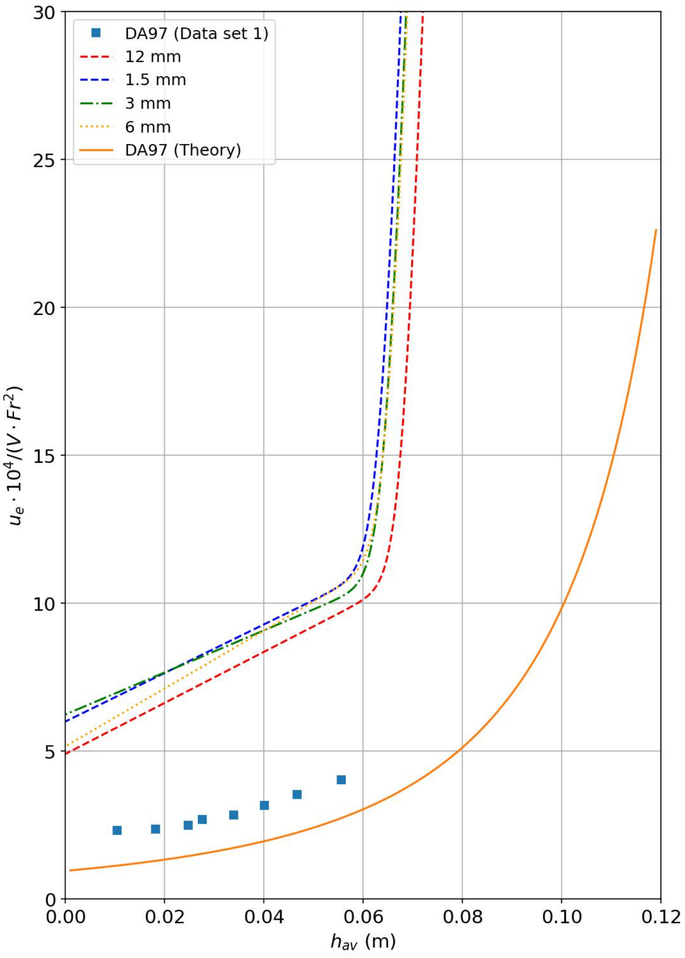

Figure 4.2. Entrainment rate (2D Mesh). DA97 (Data set 1) refers to the results of experiment number 1 of Debler and Armfield (1997). DA97 (Theory) represents the entrainment rate obtained using Equation 12

lower turbulent Schmidt number values, it is more favourable to increase the Schmidt number in order to improve the performance of the model. However, the Schmidt number needs to be kept within the range of 0.2<S_{ct}<1.3 for CFD studies (Tominaga & Stathopoulos, 2007) to maintain a realistic representation of the physical processes happening in the model. The RMSE values corresponding to the turbulent Schmidt number of 0.7, 1.0 and 1.2 were 8.37, 5.62 and 4.63 respectively as seen in Figure 4.1b. Given the small difference between the RMSE values for turbulent Schmidt numbers of 1.0 and 1.2, the choice of Schmidt number 1.0 is preferable for further analysis, as it strikes a balance between improved mixing and adhering to the established range in the literature.

4.2 3D DES lab scale model

To further investigate the accuracy of the predictions and overcome the limitations observed in the 2D simulations, a transition to three-dimensional (3D) CFD simulation was found necessary.

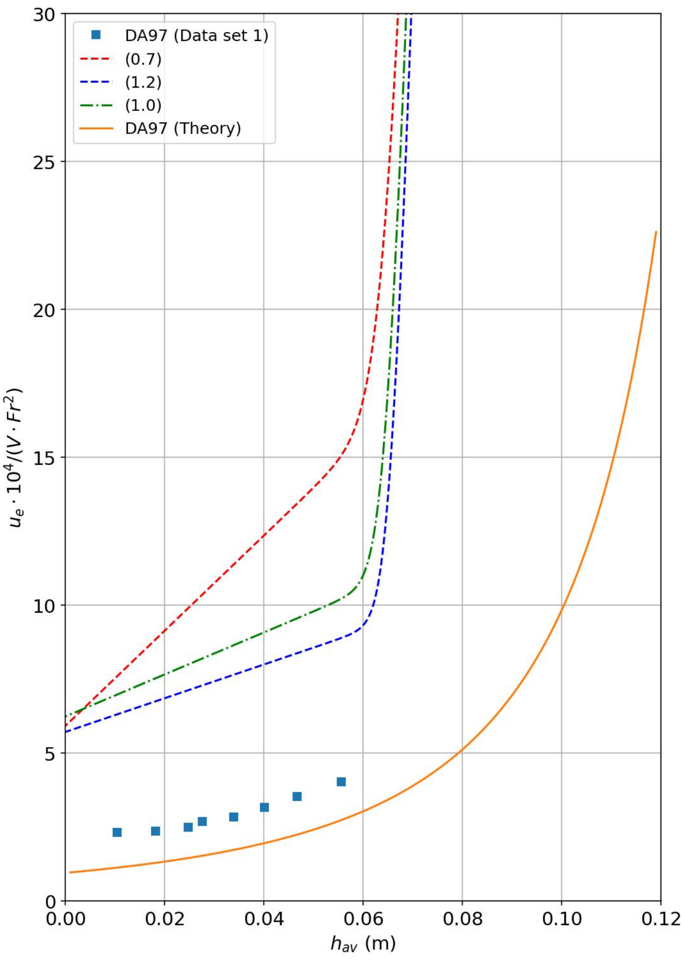

Figure 4.3. Entrainment rate for 2D different turbulent Schmidt numbers

The adoption of a 3D model became necessary to account for the additional complexities and flow phenomena inherent in three-dimensional flow scenarios. The simulation method used was DES as it offers better computational cost when compared to LES.

The transition from 2D RANS simulations to 3D DES models allowed for resolving more of the turbulence which significantly impacted the mixing of stratified layers and the rate of saltwater withdrawal. These models also account for unsteady and transient flow behaviour, capturing the continuous or alternating flow cycles that affect the entrainment process. Overall, the adoption of 3D DES models enabled a better visualisation of the flow dynamics in the cavity and offered more accurate predictions of the rate of saltwater entrainment rate from cavities.

4.2.1 Temporal evolution of the saltwater entrainment

The temporal changes in the cavity during the saltwater entrainment and interfacial mixing for simulation DES1 are presented in Figure 4.4. The sequence of images from $t = 0$ to $t = 400$ seconds shows the entrainment process of saltwater (in red) by freshwater (in blue) as they undergo mixing due to flow initiation and the vortices formation. Initially, saltwater and freshwater are distinctly separated, with the denser saltwater layer filling the cavity beneath the freshwater. As the flow commences from right to left, the saltwater interface shows an upward inclination at the downstream edge of the cavity resulting in an inclination of the pycnocline against the direction of the flow at $t = 20$ and $t = 40$ seconds as shown in Figures 4.4b and 4.4c respectively. Wave-like structures become evident at $t = 60$ seconds, signifying Kelvin-Helmholtz instabilities which are characteristic of stratified fluid layers experiencing velocity shear. The vortices formed start lifting and transporting saltwater from the surface of the interface. By $t = 80$ seconds, the vortices reach the downstream edge of the cavity and the pycnocline inclination against the flow direction reduces. As the simulation progresses, the emergence of larger vortices as seen at $t = 100$ and $t = 120$ seconds indicates an increased turbulent activity, enhancing the mixing process which in turn pushes back the saltwater at downstream edge of the cavity against the direction of the flow. The migration of the saltwater against the flow due to this phenomenon forces the pycnocline to adopt a new inclination, now aligned with the flow direction. Nevertheless, as the simulation advances, the angle of the pycnocline's slope appears to vary, which is evidenced by the snapshots taken at $t = 150$ and $t = 170$. Finally, from $t = 200$ to $t = 400$ seconds, the saltwater entrainment continues and the pycnocline inclination maintains its slope in the direction of the flow.

4.2.2 Influence of mesh variation

The 3D model's performance was assessed using three mesh sizes: 1.5 mm, 3 mm, and 12 mm. The exclusion of the 6 mm simulation was performed to reduce computation time because even without the 6mm, the trend in results was clearly seen in the 2D model. Instead, the 12 mm was used to reduce computational time. The results revealed an unexpected impact of the mesh resolution on the accuracy of predictions. For the 3 mm mesh size, the 3D model exhibited a relatively slight improvement in performance over the 2D model with an RMSE value of 4.88 whereas the 2D model resulted in an RMSE value of 5.62. However, unexpectedly when the mesh size was reduced to 1.5 mm, the model's performance decreased, resulting in a higher RMSE value of 6.89. Conversely, increasing the mesh size to 12 mm significantly improved the model's performance, with an RMSE value of 0.97 as seen in Figure 4.1e.

The model's behaviour was contrary to the anticipated outcome, which should have demonstrated improvement following the reduction in mesh size. Instead, the coarse mesh of 12 mm improved the entrainment rate and reduced the RMSE. Figure 4.5 shows a notable observation where the model employing a 12 mm mesh size not only yielded an improved entrainment rate but also displayed a relatively closer alignment of its curvature to that of the experimental results on the figure. In other words, unlike the finer mesh models which showed a linear drop in the entrainment rate, the 12 mm had a non-linear drop in the entrainment rate following similar behaviour to that

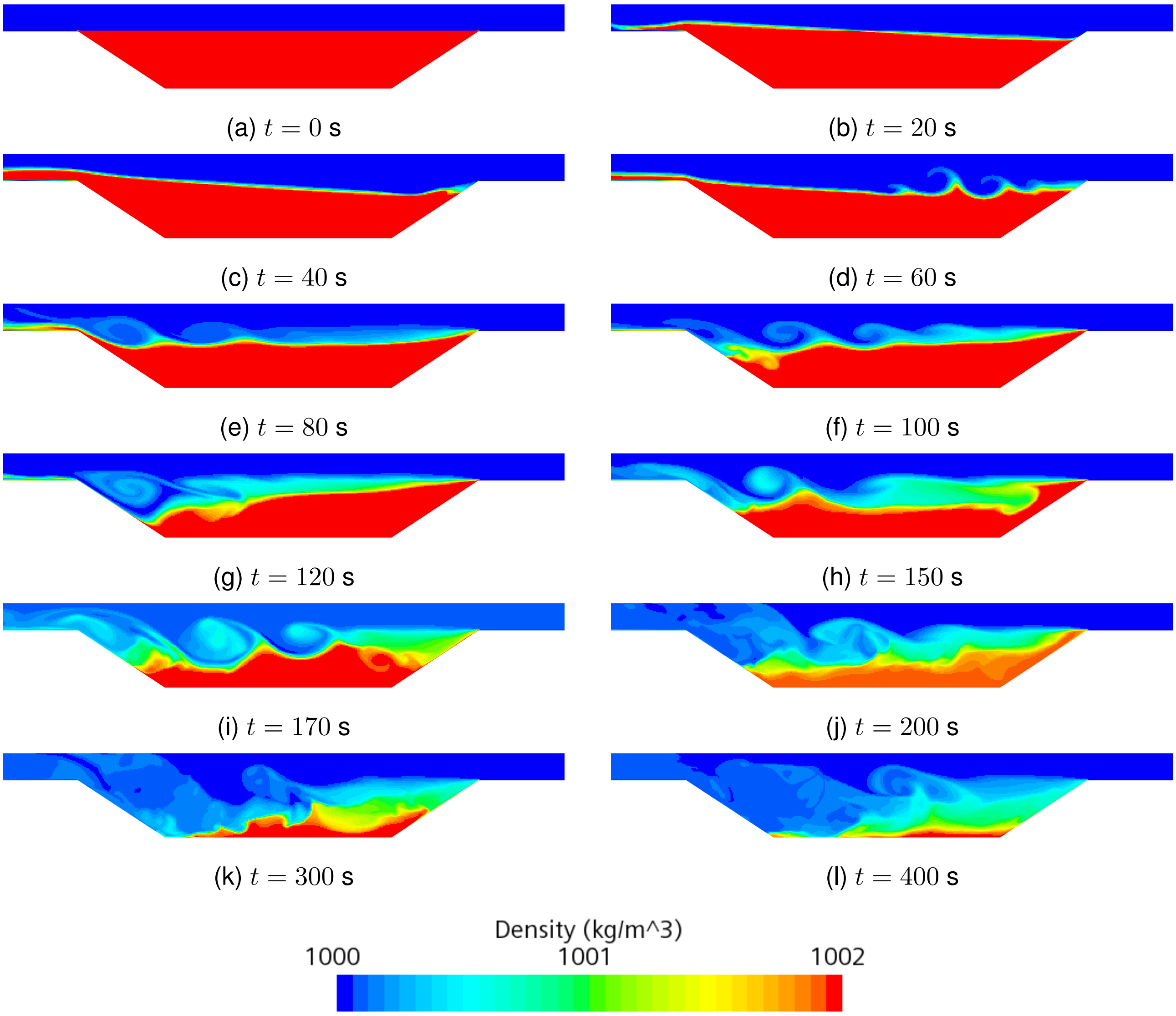

(a) $t = 0$ s

(b) $t = 20$ s

(c) $t = 40$ s

(d) $t = 60$ s

(e) $t = 80$ s

(f) $t = 100$ s

(g) $t = 120$ s

(h) $t = 150$ s

(i) $t = 170$ s

(j) $t = 200$ s

(k) $t = 300$ s

(l) $t = 400$ s

Figure 4.4. Temporal evolution of saltwater entrainment and interfacial mixing in DES1 simulation. The colours represent saltwater in red and freshwater in blue. The flow is freshwater flow is from right to left. (a) shows the initial condition where saltwater and freshwater are distinctly separated; (b) and (c) show the elevation of the saltwater interface at the downstream edge of the cavity due to the flow initiation resulting in an inclination of the pycnocline against the flow direction; (d) Wave-like structures formation at the upstream edge of the cavity indicating the evolution of Kelvin-Helmholtz instabilities; (e) The pycnocline inclination in the direction against the flow direction diminishes as it approaches a horizontal orientation; (f) The vortices induce more turbulence as they hit at the downstream edge of the cavity pushing back the saltwater against the flow direction; (g) The vortices grow larger in size and continues pushing the saltwater from the downstream edge of the cavity back against the flow direction resulting in an inclination in the pycnoline with the direction of the flow; (h) and (i) show that the pycnocline attains horizontal state followed by another inclination in the flow direction; (j), (k) and (l) shows the saltwater being flushed as the cavity empties maintaining the pycnocline incline in the direction of the flow.

seen in the experimental results as seen in Figure 4.5. This behaviour was not shown in the 1.5 mm and 3 mm mesh models indicating an improvement in the response of the 12 mm model in representing the change of entrainment rates over time as the saltwater interface drops. Although this indicates a better representation of the entrainment rate, the loss of fine-scale flow details associated with the coarser mesh resolution may limit the model's ability to capture all essential flow features accurately and this is seen in Figure 4.6.

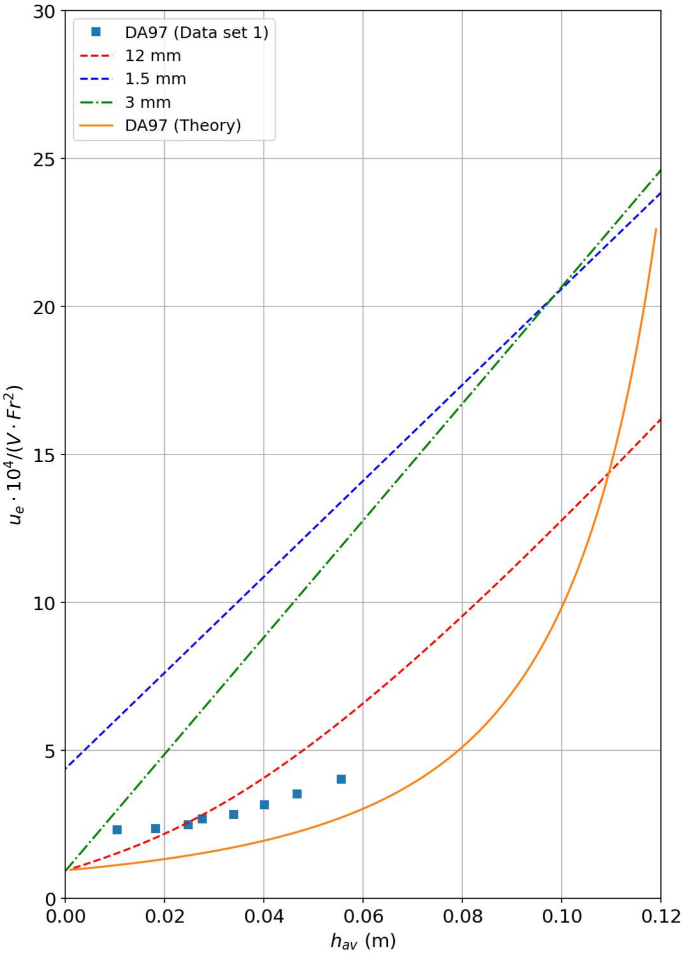

Figure 4.5. Entrainment rate for 3D mesh variations

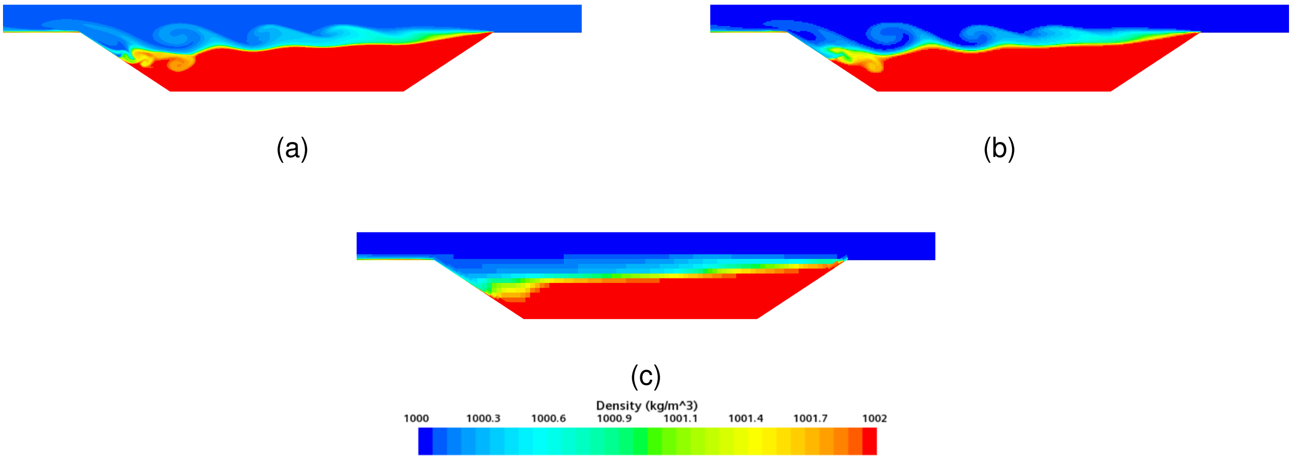

(a)

(b)

(c)

Figure 4.6. Comparison of model resolution. (a) 1.5mm; (b) 3mm; (c) 12mm. All snapshots were taken at a simulation time of 100 seconds.

4.2.3 Influence of turbulent Schmidt number

The high momentum of the turbulent flow in the case of high Schmidt numbers, as explained in section 2.4 of the literature, helps in creating a sharp boundary between the saltwater and the freshwater, resulting in a thinner and less diffused interface as seen in Figure 4.7. This figure illustrates the variance in interface thickness and its degree of diffusivity across three models, characterized by turbulent Schmidt numbers of 0.7, 1.0, and 6.0, respectively. The interface in the case of the 6.0 turbulent Schmidt number was relatively thinner due to the reduced transport of saltwater mass which should result in a reduced entrainment rate. However, this was not the case as shown in Figure 4.8. Furthermore, the RMSE values resulted in values of 4.88, 6.51 and 6.28 for the models with the Schmidt numbers of 1.0, 1.3 and 6.0 respectively as shown in Figure 4.1d. Hence, the model with Schmidt number of 1.0 resulted in a relatively better performance in comparison to the models with Schmidt numbers of 1.3 and 6.0.

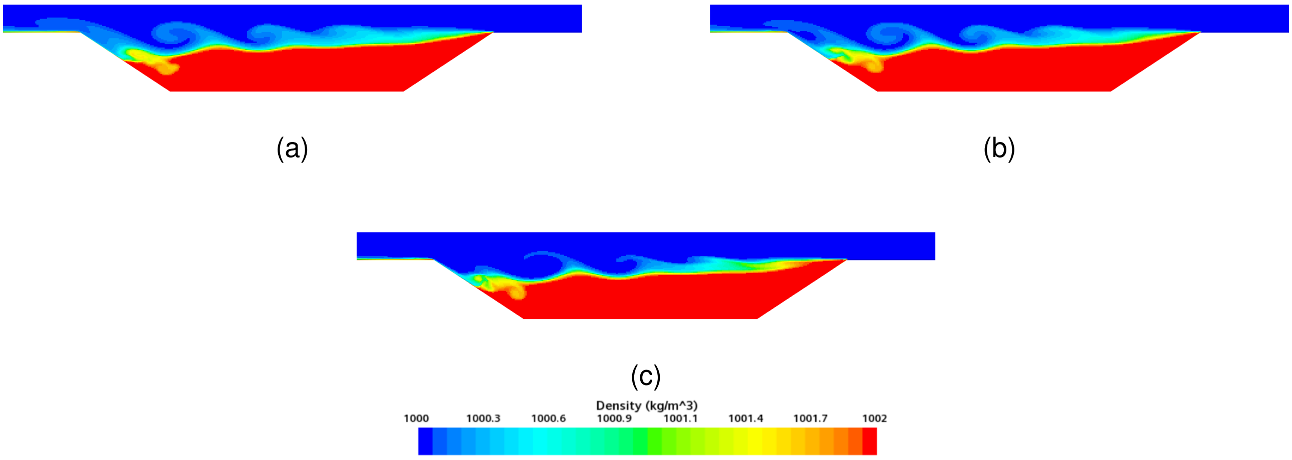
(a)

(b)

(c)

Figure 4.7. Comparative Analysis of the interface width at different Schmidt numbers. (a) S_{ct}=0.7; (b) S_{ct}=1.0; (c) S_{ct}=6.0. All snapshots were taken at a simulation time of 100 seconds.

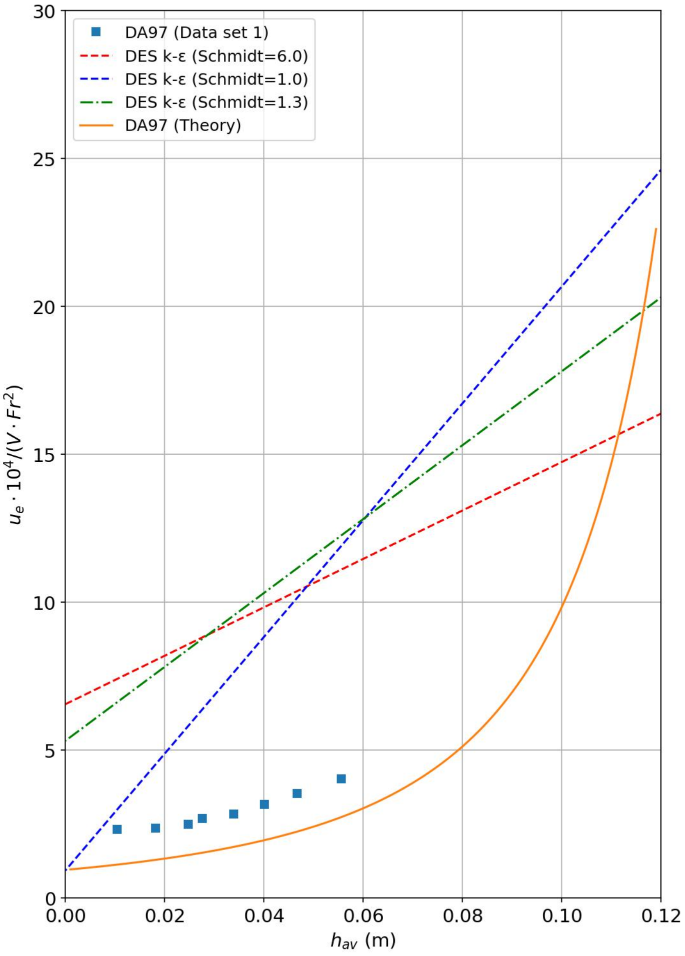

Figure 4.8. Entrainment rates for 3D different Schmidt numbers

4.2.4 Influence of turbulence closure models

The DES ($k-\epsilon$) model, which is the base model used in the 3D simulations, resulted in an RMSE value of 4.88 which was still high, Therefore, the examination of alternative turbulence closure models was motivated especially since the utilization of LES, as shown by Kirkpatrick et al. (2012), provided reliable results.

The results using different turbulence closure models showed varying levels of performance as shown in Figure 4.1c. The (DES $k-\epsilon$) model achieved an RMSE value of 4.88 whereas the (DES $k-\omega$) and DES (Spalart-Allmaras) models showed lower performance, resulting in RMSE values of 7.71 and 7.59, respectively. These findings suggest a noticeable drop in performance compared to the (DES $k-\epsilon$) model.

While Kirkpatrick et al. (2012) demonstrated that employing the LES model yielded results nearly identical to those observed in the study by Debler and Armfield (1997), the (DES $k-\epsilon$) model in this study produced an RMSE value of 4.88 indicating relatively low performance. This discrepancy suggests that the model significantly overestimates the entrainment rate, as illustrated in Figure 4.9. Despite employing similar geometric and mesh setups, the entrainment rate showed considerable discrepancy between the model in this study and the LES simulation presented by Kirkpatrick et al. (2012). The substantial difference in entrainment rates could potentially arise from variations in the temporal and spatial order utilized in the model calculations or the hybrid modelling implementation in Start CCM+ as shown in Appendix D. Kirkpatrick et al. (2012) explained that their model employed 4th-order temporal accuracy, while the maximum available order in Star CCM+ was 2nd-order for time and 3rd-order for space. Additionally, it is important to note that the model employed by Kirkpatrick et al. (2012) was internally developed specifically for predicting entrainment rates and used LES over the entire domain, whereas the model utilized for this study was a commercial software and utilized DES.

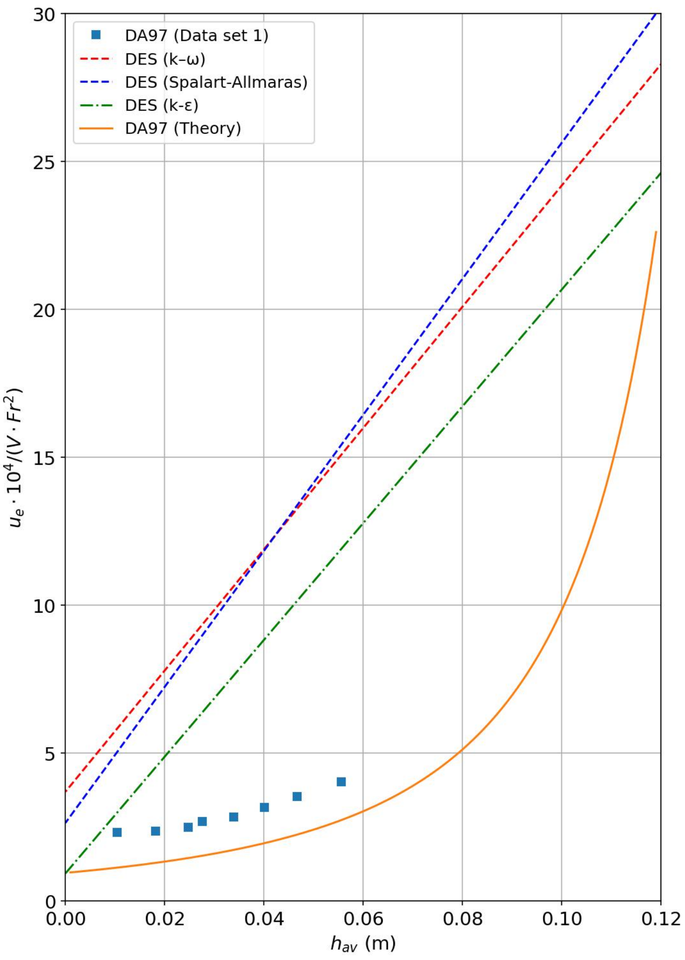

Figure 4.9. Entrainment rates for 3D different closure models

4.3 The Haringvliet DES model

4.3.1 Temporal evolution of the saltwater entrainment

The temporal changes in the scour hole during the saltwater entrainment and interfacial mixing for the Haringvliet simulation are presented in Figure 4.10. This figure illustrates the temporal evolution of the mixing process over a period from 0 to 180 minutes. Initially at $t = 0$ minutes, the separation between saltwater and freshwater is distinct. Figures 4.10b and 4.10b capture the elevation of the saltwater interface at the downstream edge of a scour hole as the simulation progresses. This elevation is a response to the flow initiation, creating an inclined pycnocline that angles against the direction of the freshwater flow similar to what was observed in DES1. Figure 4.10d reveals the formation of wave-like patterns at the upstream edge of the scour hole. These patterns are magnified in Figure 4.11 and appear to be combination of both Holmboe and K-H instabilities as shown in Figure 2.7b. After the initial lift-up of the saltwater interface at the downstream edge of the scour hole, the saltwater interface falls back as the saltwater to the upstream direction of the scour hole. The saltwater retreat is clearly seen when observing the upstream location of the saltwater in Figure 4.10 between the time $t = 120$ to $t = 180$ minutes. The backward movement of the saltwater is also better seen in Figure 4.12.

(a) $t = 0$ min

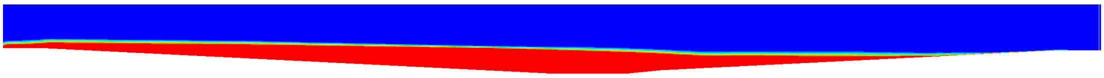

(b) $t = 45$ min

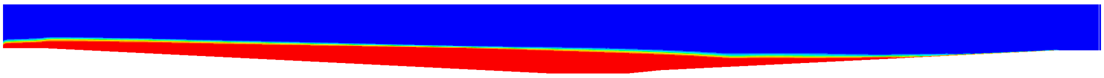

(c) $t = 60$ min

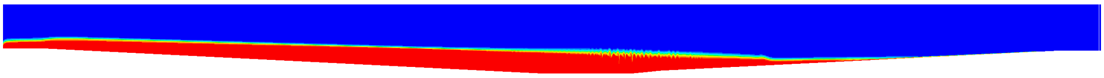

(d) $t = 90$ min

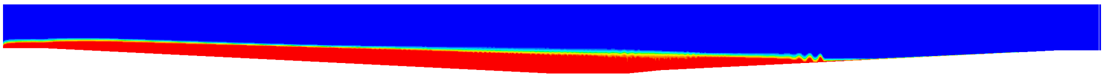

(e) $t = 120$ min

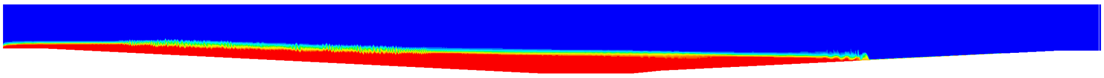

(f) $t = 150$ min

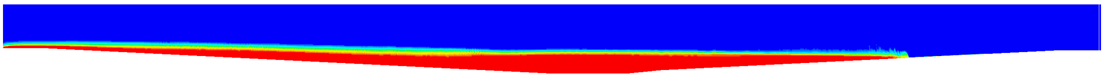

(g) $t = 180$ min

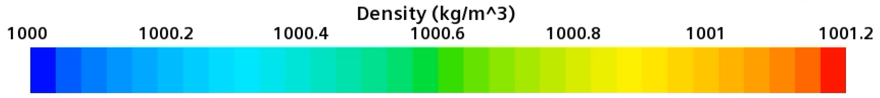

Figure 4.10. Temporal evolution of saltwater entrainment and interfacial mixing in the Haringvliet simulation. The colours represent saltwater in red and freshwater in blue. The flow is freshwater flow is from right to left. (a) Depicts the initial condition where saltwater and freshwater are distinctly separated; (b) and (c) Show the elevation of the saltwater interface at the downstream edge of the scour hole due to the flow initiation resulting in an inclination of the pycnocline against the flow direction; (d) Wave-like pattern emerges upstream edge of the scour hole; (e) More wave-like pattern forms upstream edge of the scour hole; (f) The saltwater interface height at the downstream edge of the scour hole falls down and the saltwater retreats against the flow; (g) The pycnocline levels out as it falls back to a horizontal position and the saltwater retreats further.

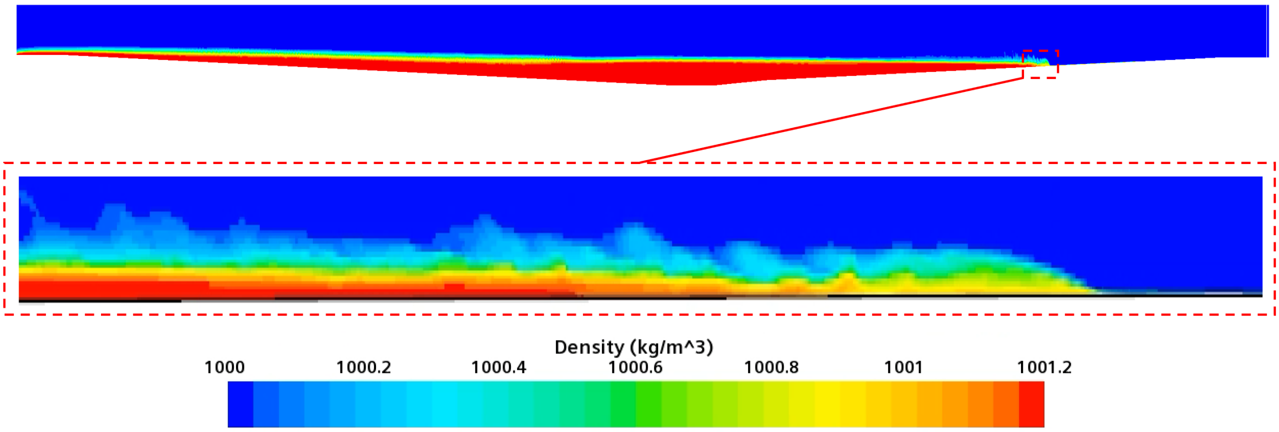

Figure 4.11. Combination of Holmboe and K-H instability. Snapshot at $t = 180$ minutes

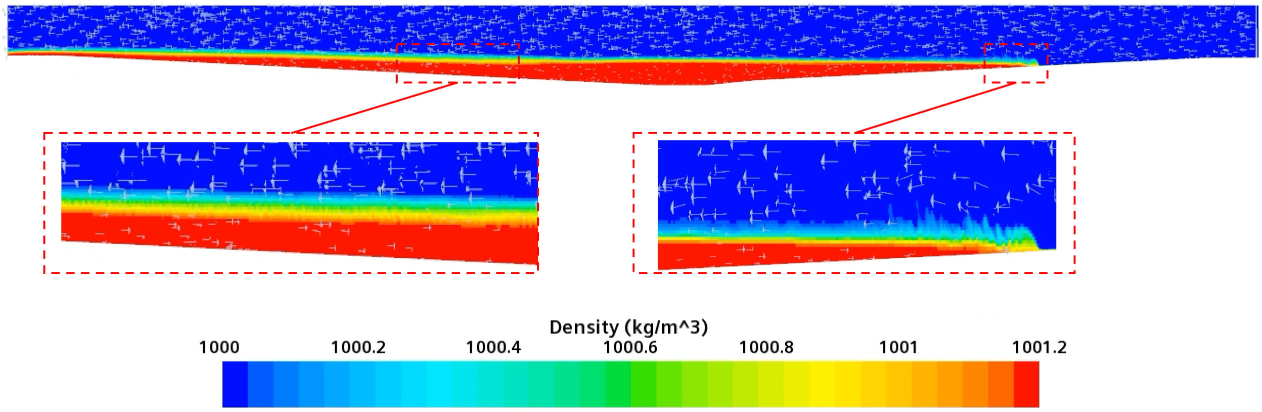

Figure 4.12. Haringvliet saltwater retreat against the flow at $t = 180$ minutes

4.3.2 Comparison of saltwater interface height to the ADCPs field observations

The observed interface height for ADCP1 at the field (Figure 4.13) showed significant fluctuations throughout the recorded period. In contrast, the model-predicted values, although exhibiting similar trends, demonstrated more consistency with fewer fluctuations. Notably, the model's global interface height, representing the remaining saltwater in the scour hole, provided a more consistent representation of the scour hole's interface height drop over time. On the other hand, measurements of the local interface height at the same location of the ADCP revealed higher interface heights in the model than that seen in the scour hole.

The observed interface height for ADCP2 at the field (Figure 4.14) followed a slightly different pattern. The observations exhibited a more gradual decline in interface height over time. Both the global interface height and the local interface height at the ADCP2 location showed close approximations of the interface changes over time observed in the scour hole.

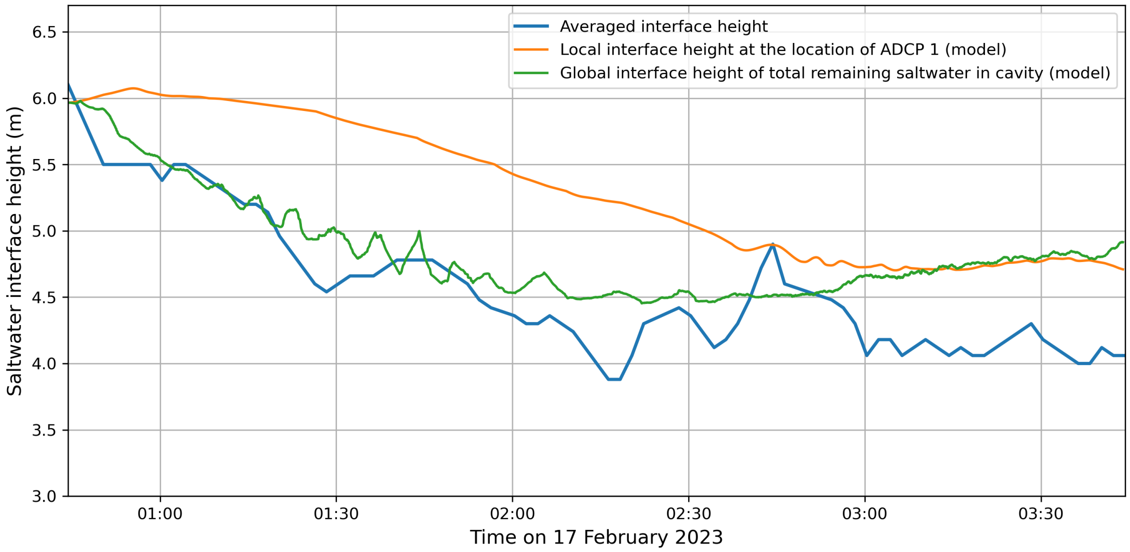

Figure 4.13. Comparison of saltwater interface height for the field observations from ADCP1 and the model output. The data are plotted starting from 00:44 on 17 February 2023

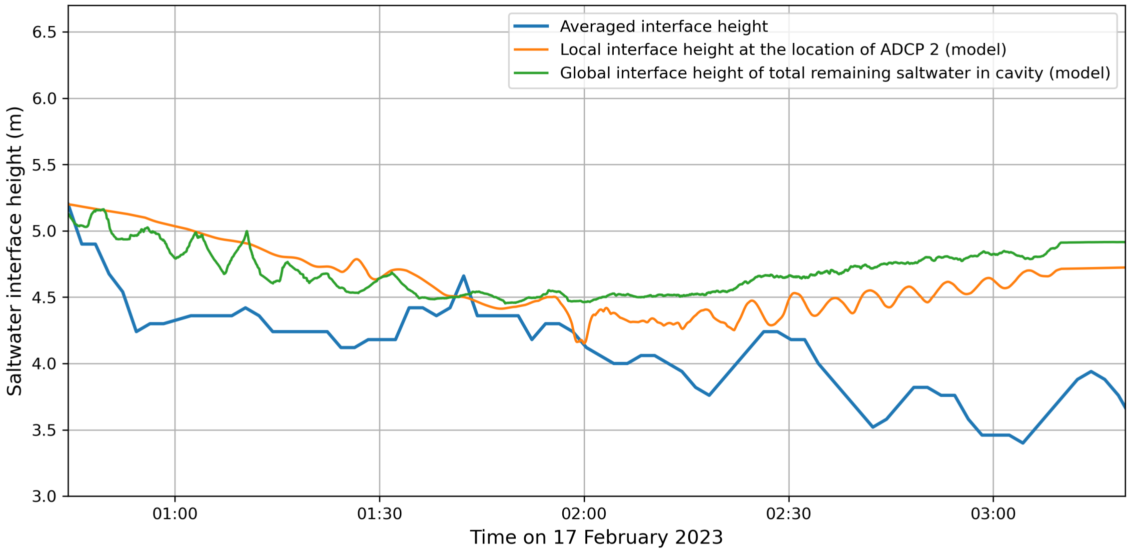

Figure 4.14. Comparison of saltwater interface height for the field observations from ADCP2 and the model output. The data are plotted starting from 00:44 on 17 February 2023

Table 4.1. RMSE of model interface heights compared to the saltwater interface heights observed from the ADCPs data. Global heights refer to the overall elevation of the saltwater interface across the entire scour hole whereas, local heights refer to the elevation of the saltwater interface at specific locations of the ADCP

Field data	**scour hole local saltwater interface height**	**scour hole global saltwater interface height**
ADCP1	0.82	0.40
ADCP2	0.62	0.72

When examining the local saltwater interface height at the corresponding ADCP locations in the model, the local saltwater interface at ADCP2 yielded an RMSE of 0.62, while ADCP1 produced an RMSE of 0.82 as shown in Table 4.1. In terms of the global saltwater interface, the RMSE values for ADCP1 and ADCP2 were 0.40 and 0.72 respectively, suggesting a good model performance when compared to both ADCPs data. This relatively enhanced performance in comparison to the lab scale model could be related to the fact that the hybrid modelling of DES in the Haringvliet case was implemented correctly by the software utilizing RANS near the walls and LES in the remaining regions unlike to what was seen in the Lab scale model (see Appendix E).

Due to the limited simulation time, it was not possible to compare the entrainment rates of the model to the saltwater interface height changes as the model output was not sufficient to calculate the entrainment rate. However, the entrainment rate of the scour hole was calculated using the field ADCP data with Equation 16 and the theoretical entrainment rate was calculated using Equation 12. At higher values of the saltwater interface, where the theoretical entrainment rates were significantly higher than those observed in the field, the entrainment rate varies significantly. The theoretical entrainment rate approaches a trend similar to those found in the ADCPs as the height of the saltwater interface decreases. Moreover, the theoretical entrainment rate agreed better with the ADCP1 observations at lower interface heights as shown in Figure 4.15.

4.3.3 Comparison of saltwater density to the CTD field observations

From Figure 4.16a, it is evident that the saltwater density obtained from the model results remains constant at a depth of 12.5 meters below the water surface. However, there is a clear decline in saltwater density at a depth of 10.3 meters. The model predicts a density decrease from 1001.2 kg/m^3 to 1000.1 kg/m^3 at this depth over a span of 70 minutes. In contrast, field observations indicate a more gradual decrease, taking roughly 3 hours for the density to drop from 1000.5 kg/m^3 to 1000.3 kg/m^3. Furthermore, while the model predicted a constant density at a depth of 12.5 throughout the 3 hour simulation, the field observations showed a density drop from 1001.2 kg/m^3 to 1000.9 kg/m^3 over the same interval of time. Finally, when averaging the saltwater density across the scour hole depth at the CTDs' location within the model, the gradient of the saltwater density decline is promisingly comparable to what is observed in the field, as shown in Figure 4.16a.

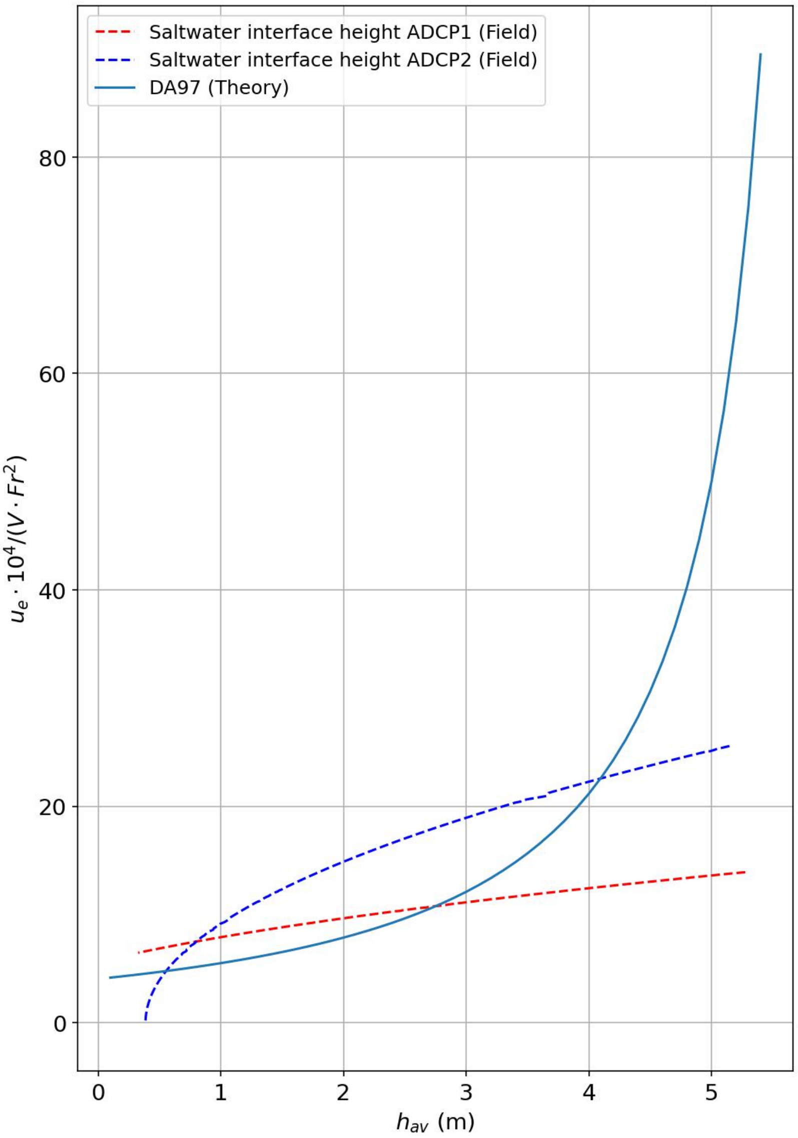

Figure 4.15. Entrainment rates in the Haringvliet

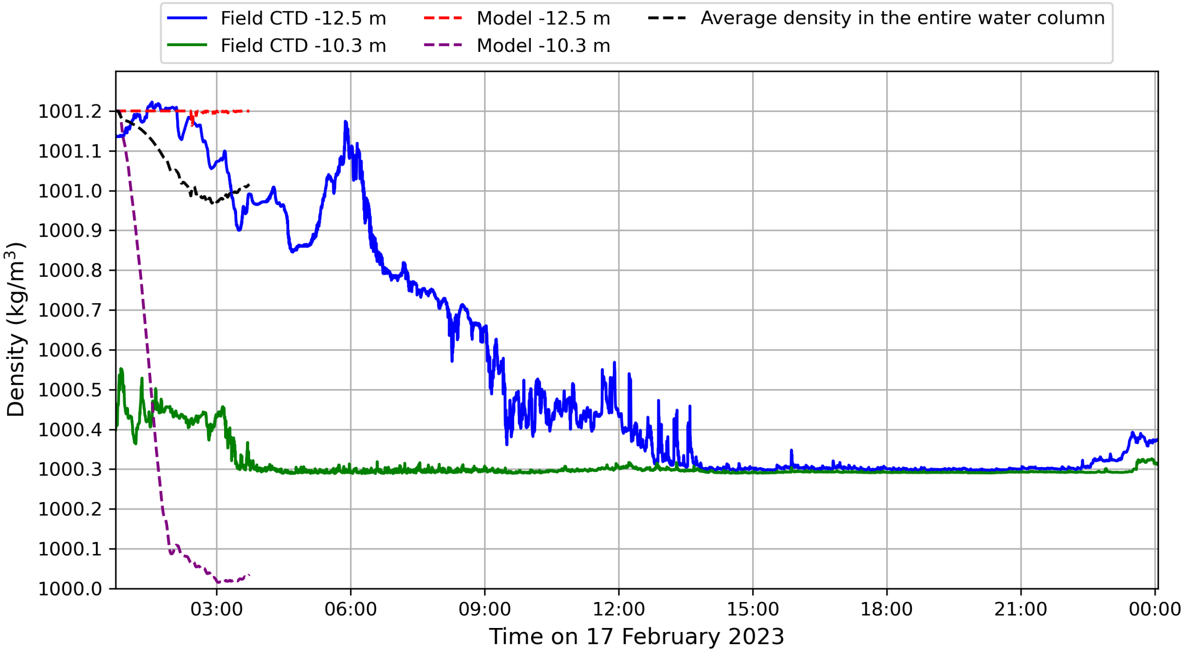

(a)

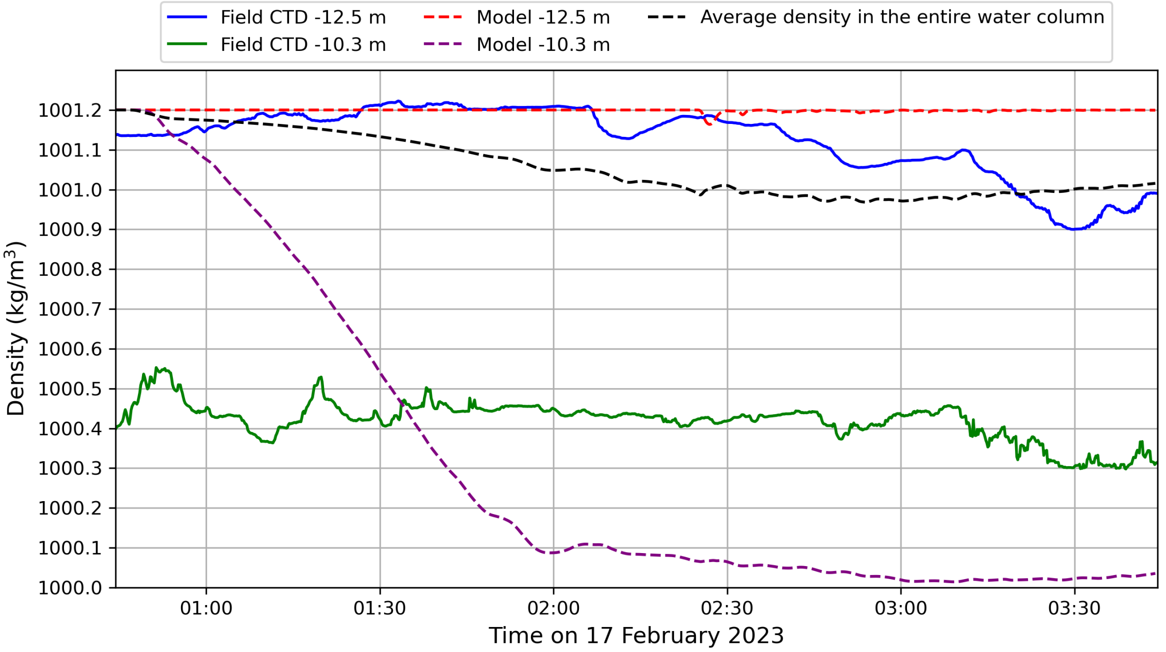

(b)

Figure 4.16. Comparison of saltwater density measured from field observations and model output at the locations of the CTDs in the Haringvliet. The data are plotted over time starting from 00:44 on 17 February 2023. a) 24 hours; b) 180 minutes covering the total simulation time of the model

5 Discussion

To establish a validated model for quantifying the saltwater entrainment rate from a scour hole in the Haringvliet, various modelling choices were thoroughly examined to check their implications on the model performance. The initial 2D model, which employed the RANS $k-\varepsilon$ model, demonstrated low performance in predicting the saltwater entrainment rates from the cavity. This motivated a comprehensive evaluation of several modelling parameters, including turbulence models, mesh sizes, and turbulent Schmidt numbers to improve the performance of the model. However, the 2D RANS model performance was still limited. Motivated by the good performance of the LES model developed by Kirkpatrick et al. (2012), a 3D DES model was developed to address the limitations of the 2D model. Upon tuning the 3D model to improve its performance, the model choices were then integrated into the Haringvliet model and the model predictions were compared against the field observational data.

5.1 The lab scale model

The variation in mesh size demonstrated a slight influence on model performance in the 2D RANS and a significant influence in the 3D DES cases. The model performance was measured in terms of the ability of the model to predict the saltwater entrainment rate. While one might expect that finer mesh would always yield superior results, the coarser mesh of 12 mm mesh size contradicted this intuition by resulting in a relatively lower RMSE when compared to the results of the 1.5 mm and the 3 mm models. The difference in performance was more evident in the DES cases. While the 2D RANS models exhibited minor performance variations, with an RMSE difference of 0.95 between the 1.5mm and 12mm mesh sizes, the 3D DES model showed a more substantial RMSE difference of 5.92 between the 1.5mm and 12mm mesh sizes.

The 2D RANS model demonstrated that a state of mesh independence was attained, indicating that subsequent alterations in mesh size would not significantly impact the model's performance. However, the 3D DES model exhibited significant performance variations when the mesh size was changed. Notably, a finer mesh led to reduced performance, primarily because it resolved more K-H instabilities, consequently resulting in higher entrainment rates. The flow is characterized by a low Richardson number, below the critical Richardson number, and a high Reynolds number indicating high turbulence and expected K-H instability formation as explained in sections 2.4 and 2.5. Therefore, the 3D DES model performed well by resolving the K-H instabilities as shown in Figure 4.4 but at the same time resulted in enhanced saltwater entrainment due to the vortices formed in the cavity. These vortices were responsible for the major transport of saltwater out of the cavity. This, in turn, could be the reason for the lower entrainment rate and higher performance observed in the 12 mm mesh size case, where the K-H instabilities were not resolved as seen in Figure 4.6.

The turbulent Schmidt number influence on the entrainment rates of saltwater in the 2D RANS models was as expected, resulting in lower entrainment rates with increased Schmidt number. However, this was not the case for the 3D case where increased Schmidt numbers resulted in higher entrainment rates and hence, poorer performance. While higher Schmidt numbers should result in lower entrainment rates due to its ability to reduce the mass transport of the saltwater, this discrepancy could be attributed to other factors affecting the entrainment rate. While higher Schmidt numbers, reduce the entrainment rate in the 2D RANS case, the 3D DES case includes more complexity and interactions in the model. Hence, keeping the Schmidt number within the range of 0.2<S_{ct}<1.3 is preferable for CFD studies to avoid unrealistic handling of the physical processes by the model (Tominaga & Stathopoulos, 2007).

Although the model consistently overestimated the results across the tested DES configurations, it is noteworthy to observe its qualitative performance. Specifically, the DES model successfully replicated the flow separation resulting in vortices formation at the upstream edge of the cavity which was also observed in the experimental of Debler and Armfield (1997). This level of accuracy in depicting the flow dynamics within the cavity is evident when comparing figures 4.4 and 2.3, which illustrate case number DES1 and the experimental findings of Debler and Armfield (1997) respectively. Furthermore, the DES model effectively replicated the initial inclination of the pycnocline in opposition to the flow, followed by the emergence of K-H instabilities at the upstream edge of the cavity. As the simulation progressed, the model captured the saltwater's retreat from the cavity's downstream edge and the subsequent alteration in the pycnocline's angle, to a slope opposing its initial orientation observed at the flow's initiation. Consequently, the model predicted well the evolving dynamics within the cavity over the course of the simulation. Nevertheless, it is important to highlight that the vortices observed in the DES simulations were significantly larger in scale compared to those identified in the LES simulation conducted by Kirkpatrick et al. (2012). This variation in model results may be attributed to several factors, including the approach used for defining saltwater, the hybrid modelling approach of DES, and the order of the temporal and spatial solvers in the modes. A key factor could be the method of saltwater definition in the Star CCM+ model, which may contribute to the observed discrepancy. Notably, the K-H instabilities increase in size when the initial vortex reaches the downstream edge of the cavity, exerting a reverse force on the saltwater, counter to the flow. This leads to enhanced mixing causing the vortices in the model to become more pronounced, as evidenced through Figures 4.4f to 4.4j. Additionally, the DES model in this study displayed inaccuracies over time in implementing the hybrid modelling in the regions of the cavity. The software utilized RANS in large regions of the model away from the walls which should not have been the case. Finally, the commercial software Star CCM+ used in this study was limited to 2nd-order time and 3rd-order space solvers, whereas Kirkpatrick et al. (2012) employed more advanced fourth-order schemes in their developed model.

5.2 The Haringvliet model

The saltwater interface height and density were compared against the field observations obtained from the ADCPs and CTDs, respectively. The interface height was evaluated against the ADCPs data in two ways: using the local saltwater interface height from the water column at the exact location of the ADCPs and using a global saltwater interface that represents the height of the remaining saltwater across the entire scour hole. The model simulated a period of 3 hours for data comparison. This run took 48 days using 16 nodes, which are 64 cores, of the cluster at Deltares which is the maximum allowed number of nodes for student use.

The global saltwater interface showed close agreement with the ADCPs observations. The local saltwater interface showed good agreement in the case of ADCP2 and showed lower agreement in the case of ADCP1. The variation in performance between ADCP1 and ADCP2 could be attributed to their locations in the scour hole. Positioned in the downstream half of the scour hole, ADCP1 faced an elevated saltwater interface due to the saltwater being pushed by the freshwater inflow upstream of the cavity, leading to a slightly inclined pycnocline in the direction against the freshwater flow. The orientation of the pycnocline follows a similar behaviour to that seen in the 3D DES lab scale simulations and to that observed in Debler and Armfield (1997) in which the saltwater interface at the downstream edge of the cavity is lifted up as the freshwater flow was initiated. This behaviour would explain the relatively high local interface heights for ADCP1 and the relatively low local interface heights for ADCP2 in comparison to the global interface height, as seen in Figures 4.13 and 4.14. Overall, the model predictions of the interface height change over time aligned well with the field observations. This correlation is clearly demonstrated in Table 4.1, where the RMSE values ranged between 0.40 to 0.82, indicating a strong level of agreement.

The model predictions of the saltwater density changes in comparison to the CTDs observations indicated a low model performance in representing the mixing of saltwater within the scour hole. At depths of -12.5 meters and -10.3 meters in the model, there's a notable discrepancy with field data. Specifically, the model presents a consistent density at -12.5 meters, whereas there were clear fluctuations in density in the field at the same depth. Furthermore, at a depth of -10.3 meters, the model predicted a sharp drop in density while the field observations at the same height showed a gradual decrease in density. However, when the density values were averaged across the entire water column in the scour hole, the model predicted a gradual drop in the density characterized by a gradient that is comparable to the field observations at -12.5 meters, as illustrated in Figure 4.16. Another reason for this discrepancy could be the method of defining saltwater in this study and the way Star CCM+ handles it. Unlike what is seen in the field observations where the saltwater density varies across the depth, the density in the model was either freshwater or saltwater with a small gradient near the saltwater interface as seen in Figure 4.10. This also meant that mixing occurred near the surface of the interface and not through the entire depth in the scour hole. These observations implied that the mixing of saltwater and freshwater in the model is confined to the area near the interface surface.

5.3 Models comparison

The Haringvliet model outperformed the lab-scale model, which consistently over-predicted the entrainment of saltwater from the cavity. This discrepancy could be related to the way the software handled each case. In the lab scenario, the software did not execute the hybrid modelling accurately (refer to Appendices D and E). When employing DES, it is expected that RANS is utilized near the walls and LES is used for the rest of the model region. However, this was not the situation in the lab scale models. The DES $k-\varepsilon$ model employed RANS across the whole model domain for more than 40 seconds after the run commenced. It then began using LES but only in a limited section of the boundary, neglecting areas where intense mixing and vortex formation were likely to occur. On the other hand, the DES $k-\omega$ model was somewhat more accurate, primarily using RANS near the walls and LES for the remaining region of the model. Still, this was observed mainly in the later phases of the simulation, with the initial stages indicating irregular application of RANS and LES within the model regions.

Although the Haringvliet model utilized the DES $k-\varepsilon$ model with similar modelling choices to that implemented in the lab scale model, it appeared to effectively apply RANS near the walls and LES throughout the remaining region of the model during the entire simulation. In the lab scale model, the software might have faced difficulty transitioning from LES to RANS as it approaches the wall at the downstream edge of the cavity, especially when constrained in a small geometry and with a smaller Reynolds number. This led to unusual flow patterns near the downstream edge of the cavity. As a result, a vortex grew at the downstream edge of the cavity, which, over time, introduced high turbulence into the cavity flow as illustrated in Figure4.4. Such behaviour was absent in the simulation by Kirkpatrick et al. (2012) (refer to Figure C.1). In contrast, their model showed a more stable interface with a more gradual saltwater entrainment from the surface of the interface, without any large-scale vortex formations like those observed in the models developed in this study.

5.4 Study limitations

The model did not take into account variations in temperatures and their effect on the density variations. The model did not account for site-specific characteristics, such as the wind, that might influence the entrainment rates of saltwater from the scour hole. Furthermore, the Haringvliet model was simplified by having a symmetry plane rather than using the actual breadth of the scour hole. Finally, the Haringvliet model's prolonged run time rendered it infeasible for sensitivity analysis studies. Furthermore, the significant computational expense is a drawback that makes this modelling option unfavourable for applications.

6 Conclusion and recommendations

As climate change worsens, saltwater intrusion poses an increasing risk to freshwater availability. For this reason, it is important to reduce saltwater intrusion. A practical approach towards reducing saltwater intrusion is through flushing saltwater from scour holes. This research focused on advancing the understanding of saltwater entrainment from cavities, with a primary focus on utilizing CFD to model these phenomena both on laboratory and real-world scales. The main research question was formulated and further divided into four sub-questions. By addressing these sub-questions, the main research question can be fully addressed. The sub-questions and the main research question are answered below.

1. Which turbulence model, in terms of precision and computational efficiency, best estimates the entrainment rate of saltwater from the laboratory scale cavity?

The choice of turbulence closure model has a significant impact on the accuracy of predicting the withdrawal rate of saltwater from a cavity. While the LES model of Kirkpatrick et al. (2012) showed superior performance to the tested models in this study. The tested model configurations showed that the DES $k-\varepsilon$ model offered the highest performance in predicting the saltwater entrainment rates. The DES $k-\varepsilon$ model predicted K-H instabilities but produced large vortices that made the flow very turbulent in the cavity which was not the case in the results of Kirkpatrick et al. (2012). Nevertheless, the model predicted well the overall flow behaviour captured in the experiment of Debler and Armfield (1997). The model was able to predict the eruption of the interface and the changes in the orientations of the pycnocline as the simulation progressed.

2. How does the dynamics of the flow change when the model is upscaled to replicate the dimensions of a scour hole in the Haringvliet and what consequences does this transformation have on the entrainment rate of saltwater?

Upscaling the model to replicate the dimensions of a scour hole in the Haringvliet, distinct alterations in flow dynamics were observed. The upscaled model showed better performance in predicting the saltwater entrainment rate from the scour hole. Contrasting with the lab-scale model, which exhibited high turbulence and significant vortex formation, the Haringvliet model showed no such large eddy formations. This variation might be attributed to differences in their Richardson numbers. The lab-scale model had a low Richardson number, remaining below the critical Richardson number, whereas the Haringvliet model featured a Richardson number surpassing the critical Richardson number. This could also explain why the performance of the Haringvliet surpassed the performance of the lab scale model. The low Richardson number caused the flow to become more turbulent resulting in larger vortices that increased the saltwater entrainment and hence resulted in an overestimation of the saltwater entrainment rate.

3. How does the entrainment rate from the field data of the Haringvliet compare to the theoretical relation in the literature?

The entrainment rate from the field data of the Haringvliet deviates from the entrainment derived from the theoretical relation found in Debler and Armfield (1997). The entrainment rate differs significantly at higher values of the saltwater interface, where the theoretical entrainment rates were much higher in comparison to those observed in the field. As the saltwater interface height drops, the theoretical entrainment rate approaches a trend similar to those observed from the ADCPs. Furthermore, at lower interface heights, the theoretical entrainment rate was in better agreement with the observations from ADCP1. This suggests that the mixing coefficient used in Debler and Armfield (1997) provides a better representation of the saltwater entrainment near the downstream edge of the scour hole where ADCP1 is located.

4. How does the change in the saltwater interface as observed in the Haringvliet compare to the predictions of the CFD model?

The model predicted higher local interface heights at ADCP1 compared to actual observations. For ADCP2, the model prediction of the local interface height showed better agreement than ADCP1 with the field observations. Overall, the RMSE values indicated a good model performance, especially for the global interface height, highlighting the model's ability to accurately capture overall trends despite some discrepancies in local predictions. However, due to the limited simulation time of 3 hours, the model's performance in fully capturing the scour hole's saltwater emptying process, which typically spans 12 to 24 hours, remains somewhat uncertain.

How can the entrainment rate of saltwater from cavities be accurately predicted using CFD modelling with RANS and DES as modelling approaches in laboratory and real-world scales?

Predicting the entrainment rate of saltwater from cavities using CFD involves selecting appropriate turbulence models and adapting them for different scales. RANS modelling is more computationally efficient but is unable to predict all the flow dynamics in the cavity such as the formation of the K-H instability which took an important role in the saltwater entrainment out of the cavity. In contrast, DES modelling blends RANS and LES techniques offering the possibility to capture such instabilities. Overall, RANS and DES modelling can offer a good prediction of the saltwater entrainment in the lab scale model using the Star CCM+ software taking into account an overestimation error factor of the saltwater. However, DES modelling offered a better prediction of the saltwater entrainment from the field model of the scour hole.

Recommendations

Based on the insights gained from this research, the following recommendations are proposed:

- It is recommended to explore software that gives the user more control over the modelling process like OpenFOAM. Unlike the commercial CFD software used in this study, OpenFOAM offers greater transparency and control over the modelling process, allowing researchers to fine-tune and adapt their models with more precision. One possible thing to investigate is the use of higher-order scheme solvers which was not possible in the Star CCM+ software. Additionally, the open-source nature of OpenFOAM promotes community-driven improvements and collaborations, potentially leading to easier access to discussions over issues such as the improper implementation of RANS away from the boundaries in the hybrid modelling in this study.
- The formation of large vortices in the model reduced the performance of the model for the lab scale models. Therefore, it would be interesting to find a way to suppress the size of these vortices.
- The definition of saltwater could be investigated to improve the ability of the model to represent the density gradient through the entire water column.
- Motivated by the good performance of the field scale model, the use of a limiter to limit the vortices size could potentially improve the performance of the lab scale model. Despite using a similar model set up in the lab scale model and in the field scale model, the field scale model performed better. This could be attributed to the large scale vortices formed in the lab scale simulations. Therefore, limiting the size of these vortices could increase the performance of the model.
- Given the distinct performances of the Star CCM+ software for the laboratory and field scale models, it is advisable to examine the impacts of turbulence models on this larger scale model. Assessing whether RANS yields results comparable to DES could lead to decreased computational costs. Such an evaluation would also enable comprehensive sensitivity analysis, which could prove valuable for sluice management.
- The performance of the LES model could be investigated especially because the LES model of Kirkpatrick et al. (2012) showed very good performance in predicting the saltwater entrainment rates.
- Future studies should place a strong emphasis on validating the chosen turbulence model against more extensive sets of real-world data. This will further solidify the findings of this research and ensure that CFD models accurately represent the saltwater entrainment from real-world scour holes.

References

Almohagry, A. A. (2023). *Saltwater entrainment from bathymetric depressions: A CFD analysis from a laboratory cavity to a scour hole in the haringvliet estuary* (Literature Study Report. Master Thesis Preparation). University of Twente. The Netherlands.

An, Q., Wu, Y., Taylor, S., & Zhao, B. (2009). Influence of the three gorges project on saltwater intrusion in the yangtze river estuary. *Environmental Geology*, *56*(8), 1679–1686. https://doi.org/10.1007/s00254-008-1266-4

Argyropoulos, C., & Markatos, N. (2015). Recent advances on the numerical modelling of turbulent flows. *Applied Mathematical Modelling*, *39*(2), 693–732. https://doi.org/10.1016/j.apm.2014.07.001

Augustijn, D. C. M., Van Den Berg, M., De Bruine, E., & Korving, H. (2011). Dynamic control of salt intrusion in the mark-vliet river system, the netherlands. *Water Resources Management*, *25*(3), 1005–1020. https://doi.org/10.1007/s11269-010-9738-1

Bakker, A., Haidari, A. H., & Oshinowo, L. M. (2001). Realize greater benefits from CFD. *Chemical engineering progress*, *97*(3), 45–53.

Baratian-Ghorghi, Z., & Kaye, N. B. (2013). Modeling the purging of dense fluid from a street canyon driven by an interfacial mixing flow and skimming flow. *Physics of Fluids*, *25*(7), 076603. https://doi.org/10.1063/1.4813786

Boschetti, T., O'Mahoney, T., & Bijlsma, A. C. (2017). CFD modelling of the mitigation of salt intrusion by selective withdrawal, 4.

CHANG, P. K. (1970). *Separation of flow*. Elsevier. https://doi.org/10.1016/C2013-0-05541-7

Christodoulou, G. C. (1986). Interfacial mixing in stratified flows. *Journal of Hydraulic Research*, *24*(2), 77–92. https://doi.org/10.1080/00221688609499323

Chu, V. H., & Baddour, R. E. (1984). Turbulent gravity-stratified shear flows. *Journal of Fluid Mechanics*, *138*, 353–378. https://doi.org/10.1017/S002211208400015X

Debler, W., & Armfield, S. W. (1997). The purging of saline water from rectangular and trapezoidal cavities by an overflow of turbulent sweet water. *Journal of Hydraulic Research*, *35*(1), 43–62. https://doi.org/10.1080/00221689709498643

de Fockert, A., O'Mahoney, T. S. D., Nogueira, H. I. S., Oldenziel, G., Bijlsma, A. C., & Janssen, H. (2022). Assessing the effectiveness of the IJmuiden salt screen design for nonuniform selective withdrawal by physical and numerical modeling. *Journal of Hydraulic Engineering*, *148*(2), 05021011. https://doi.org/10.1061/(ASCE)HY.1943-7900.0001958

Di Bernardino, A., Monti, P., Leuzzi, G., & Querzoli, G. (2020). Turbulent schmidt number measurements over three-dimensional cubic arrays. *Boundary-Layer Meteorology*, *174*(2), 231–250. https://doi.org/10.1007/s10546-019-00482-z

Hogg, A. M., & Ivey, G. N. (2003). The kelvin–helmholtz to holmboe instability transition in stratified exchange flows. *Journal of Fluid Mechanics*, *477*. https://doi.org/10.1017/S0022112002003397

Hossain, M. S., El-Shafie, A., Mahzabin, M. S., & Zawawi, M. H. (2018). System performances analysis of reservoir optimization–simulation model in application of artificial bee colony algorithm. *Neural Computing and Applications*, *30*(7), 2101–2112. https://doi.org/10.1007/s00521-016-2798-2

Huismans, Y. (2016). *Systeemanalyse rijn-maasmonding: Analyse relaties noord- en zuidrand en gevoeligheid stuurknoppen: Deelproject systeemanalyse en slim watermanagement* (1230077-001-ZWS-0010). https://publications.deltares.nl/1230077_001.pdf

Jirka, G. H. (1979). SUPERCRITICAL WITHDRAWAL FROM TWO-LAYERED FLUID SYSTEMS: Part 1: Two-dimensional skimmer wall. *Journal of Hydraulic Research*, *17*(1), 43–51. https://doi.org/10.1080/00221687909499599

Kirkpatrick, M. P., & Armfield, S. W. (2005). Experimental and large eddy simulation results for the purging of salt water from a cavity by an overflow of fresh water. *International Journal of Heat and Mass Transfer*, *48*(2), 341–359. https://doi.org/10.1016/j.ijheatmasstransfer.2004.08.016

Kirkpatrick, M. P., Armfield, S. W., & Williamson, N. (2012). Shear driven purging of negatively buoyant fluid from trapezoidal depressions and cavities. *Physics of Fluids*, *24*(2), 025106. https://doi.org/10.1063/1.3680861

Kolmogorov, A. (1991). Local structure of turbulence in incompressible viscous fluid for very large reynolds number. *Dokl Akad Nauk SSSR*, *434*, 9–13.

Konikow, L. F., & Kendy, E. (2005). Groundwater depletion: A global problem. *Hydrogeology Journal*, *13*(1), 317–320. https://doi.org/10.1007/s10040-004-0411-8

Kranenburg, W. M., Tiessen, M. C., Blaas, M., & Van Veen, N. P. (2023). Circulation, stratification and salt dispersion in a former estuary after reintroducing seawater inflow. *Estuarine, Coastal and Shelf Science*, *282*, 108221. https://doi.org/10.1016/j.ecss.2023.108221

Kundu, P. K., Cohen, I. M., & Dowling. (2012). Vorticity dynamics. In *Fluid mechanics* (pp. 171–196). Elsevier. https://doi.org/10.1016/B978-0-12-382100-3.10005-8

Linden, P. F. (1979). Mixing in stratified fluids. *Geophysical & Astrophysical Fluid Dynamics*, *13*(1), 3–23. https://doi.org/10.1080/03091927908243758

Loucks, D. P., & Van Beek, E. (2017). *Water resource systems planning and management*. Springer International Publishing. https://doi.org/10.1007/978-3-319-44234-1

Markatos, N. (1986). The mathematical modelling of turbulent flows. *Applied Mathematical Modelling*, *10*(3), 190–220. https://doi.org/10.1016/0307-904X(86)90045-4

Meehan, M. A., Wimer, N. T., & Hamlington, P. E. (2022). Richardson and reynolds number effects on the near field of buoyant plumes: Temporal variability and puffing. *Journal of Fluid Mechanics*, *950*, A24. https://doi.org/10.1017/jfm.2022.788

Moukalled, F., Mangani, L., & Darwish, M. (2016). *The finite volume method in computational fluid dynamics: An advanced introduction with OpenFOAM and matlab*. Springer.

Nguyen, A. D., Savenije, H. H., Pham, D. N., & Tang, D. T. (2008). Using salt intrusion measurements to determine the freshwater discharge distribution over the branches of a multi-channel estuary: The mekong delta case. *Estuarine, Coastal and Shelf Science*, *77*(3), 433–445. https://doi.org/10.1016/j.ecss.2007.10.010

Nitsche, M. (2006). Vortex dynamics. In *Encyclopedia of mathematical physics* (pp. 390–399). Elsevier. https://doi.org/10.1016/B0-12-512666-2/00254-6

R. Massel, S. (2015). *Internal gravity waves in the shallow seas*. Springer International Publishing. https://doi.org/10.1007/978-3-319-18908-6

Rashaduddin, M., & Waheedullah, A. (2017). A study on airflow over a plane. *6*(10).

Rodi, W. (2017, November 1). *Turbulence models and their application in hydraulics: A state-of-the-art review* (W. Rodi, Ed.; 3rd ed.). Routledge. https://doi.org/10.1201/9780203734896

Rowley, C. W., & Williams, D. R. (2006). DYNAMICS AND CONTROL OF HIGH-REYNOLDS-NUMBER FLOW OVER OPEN CAVITIES. *Annual Review of Fluid Mechanics*, *38*(1), 251–276. https://doi.org/10.1146/annurev.fluid.38.050304.092057

Ruiz, L. E. A. (2022). *The flushing procedure in salt filled cavities* (Internship Report).

Sierra, J. P., Sánchez-Arcilla, A., Figueras, P. A., González Del Río, J., Rassmussen, E. K., & Mösso, C. (2004). Effects of discharge reductions on salt wedge dynamics of the ebro river: SALT WEDGE DYNAMICS. *River Research and Applications*, *20*(1), 61–77. https://doi.org/10.1002/rra.721

Smagorinsky, J. (1963). GENERAL CIRCULATION EXPERIMENTS WITH THE PRIMITIVE EQUATIONS: I. THE BASIC EXPERIMENT*. *Monthly Weather Review*, *91*(3), 99–164. https://doi.org/10.1175/1520-0493(1963)091<0099:GCEWTP>2.3.CO;2

Spalart, P., Jou, W.-H., Strelets, M., & Allmaras, S. (1997). Comments on the feasibility of LES for wings, and on a hybrid RANS/LES approach. https://www.researchgate.net/publication/236888805_Comments_on_the_Feasibility_of_LES_for_Wings_and_on_a_Hybrid_RANSLES_Approach

Spalart, P. R. (2008). Detached-eddy simulation.

Strang, E. J., & Fernando, H. J. S. (2001). Entrainment and mixing in stratified shear flows. *Journal of Fluid Mechanics*, *428*, 349–386. https://doi.org/10.1017/S0022112000002706

Strang, E. J., & Fernando, H. J. S. (2004). Shear-induced mixing and transport from a rectangular cavity. *Journal of Fluid Mechanics*, *520*, 23–49. https://doi.org/10.1017/S0022112004001697

Surana, K. S., Allu, S., Tenpas, P. W., & Reddy, J. N. (2007). K-version of finite element method in gas dynamics: Higher-order global differentiability numerical solutions. *International Journal for Numerical Methods in Engineering*, *69*(6), 1109–1157. https://doi.org/10.1002/nme.1801

Thompson, D. J., Latorre Iglesias, E., Liu, X., Zhu, J., & Hu, Z. (2015). Recent developments in the prediction and control of aerodynamic noise from high-speed trains. *International Journal of Rail Transportation*, *3*(3), 119–150. https://doi.org/10.1080/23248378.2015.1052996

Tominaga, Y., & Stathopoulos, T. (2007). Turbulent schmidt numbers for CFD analysis with various types of flowfield. *Atmospheric Environment*, *41*(37), 8091–8099. https://doi.org/10.1016/j.atmosenv.2007.06.054

Townsend, A. A. (1958). Turbulent flow in a stably stratified atmosphere. *Journal of Fluid Mechanics*, *3*(4), 361–372. https://doi.org/10.1017/S0022112058000045

Travin, A., Shur, M., Strelets, M., & Spalart, P. (2000). Detached-eddy simulations past a circular cylinder. *Flow, Turbulence and Combustion*, *63*(1), 293–313. https://doi.org/10.1023/A:1009901401183

UNESCO. (1981). Tenth report of the joint panel on oceanographic tables and standards. *Unesco technical papers in marine science*, *36*. https://www.jodc.go.jp/info/ioc_doc/UNESCO_tech/046148eb.pdf

Wilcox, D. C. (1994). *Turbulence modeling for CFD* (1st edition). DCW Industries.

Williamson, N., Kirkpatrick, M. P., & Armfield, S. W. (2018). Entrainment across a sheared density interface in a cavity flow. *Journal of Fluid Mechanics*, *835*, 999–1021. https://doi.org/10.1017/jfm.2017.796

Xuequan, E., & Hopfinger, E. J. (1986). On mixing across an interface in stably stratified fluid. *Journal of Fluid Mechanics*, *166*(-1), 227. https://doi.org/10.1017/S0022112086000125

Zawawi, M. H., Saleha, A., Salwa, A., Hassan, N. H., Zahari, N. M., Ramli, M. Z., & Muda, Z. C. (2018). A review: Fundamentals of computational fluid dynamics (CFD), 020252. https://doi.org/10.1063/1.5066893

A UNESCO formulation for defining the density of saltwater

The density of seawater is calculated using Equation A19 (R. Massel, 2015; UNESCO, 1981).

$$\rho = \rho_{SMOW} + \alpha S + \beta S^{1.5} + \gamma S^2 \tag{A19}$$

where, ρ is the density, ρ_{SMOW} is the Standard Mean Ocean Water density, T is the temperature, S is the salinity and α, β, and γ are coefficients determined based on temperature as shown below.

$$\rho_{SMOW} = a_0 + a_1 T + a_2 T^2 + a_3 T^3 + a_4 T^4 + a_5 T^5 \tag{A20}$$

$$\alpha = b_0 + b_1 T + b_2 T^2 + b_3 T^3 + b_4 T^4 \tag{A21}$$

$$\beta = c_0 + c_1 T + c_2 T^2 \tag{A22}$$

Where:

$$\begin{aligned} a_0 &= 999.842594 \\ a_1 &= 6.793953 \times 10^{-2} \\ a_2 &= -9.095290 \times 10^{-3} \\ a_3 &= 1.001685 \times 10^{-4} \\ a_4 &= -1.120083 \times 10^{-6} \\ a_5 &= 6.536332 \times 10^{-9} \end{aligned}$$

$$\begin{aligned} b_0 &= 8.2449 \times 10^{-1} \\ b_1 &= -4.0899 \times 10^{-3} \\ b_2 &= 7.6438 \times 10^{-5} \\ b_3 &= -8.2467 \times 10^{-7} \\ b_4 &= 5.3875 \times 10^{-9} \end{aligned}$$

$$\begin{aligned} c_0 &= -5.7246 \times 10^{-3} \\ c_1 &= 1.0227 \times 10^{-4} \\ c_2 &= -1.6546 \times 10^{-6} \\ \gamma &= 4.8314 \times 10^{-4} \end{aligned}$$

Under a constant temperature, the UNESCO formulation results in a linear relationship since the equation solely depends on the salinity value. Therefore, a simplified approach can be adopted in scenarios where temperature is not considered.

B Haringvliet observational data

The data presented below is part of WP 3.2 of the SaltiSOLUTIONS and was provided for the validation of the Haringvliet model in this study.

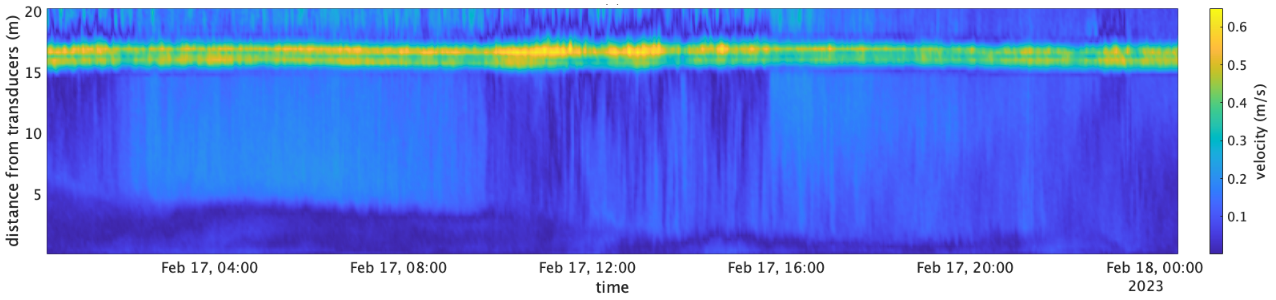

(a) Mean horizontal velocity

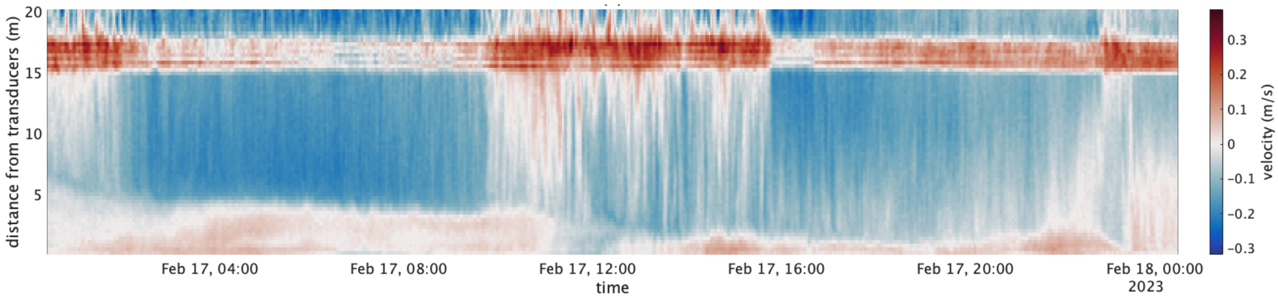

(b) Velocity in the primary direction of the cavity

Figure B.1. ADCP 1 field data

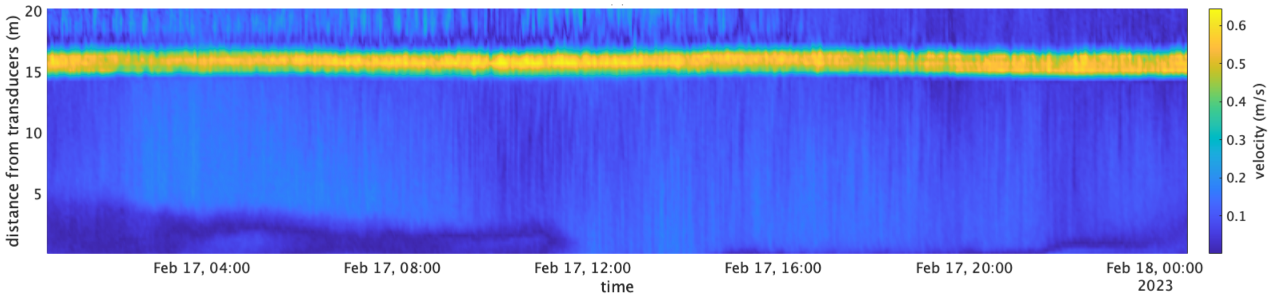

(a) Mean horizontal velocity

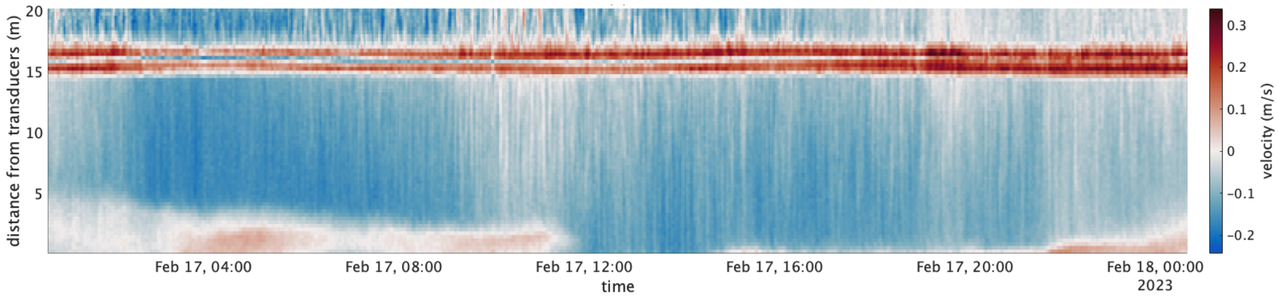

(b) Velocity in the primary direction of the cavity

Figure B.2. ADCP 2 field data

C Model qualitative observations from the Literature

The LES model of Kirkpatrick et al. (2012) is shown below.

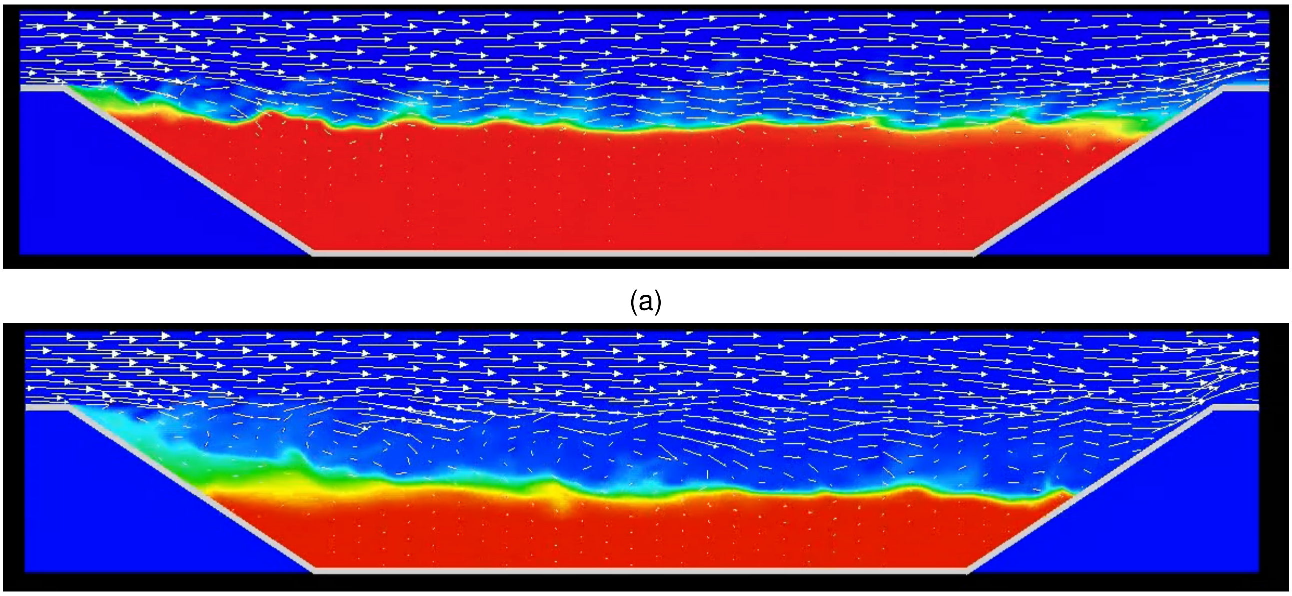

(a)

(b)

Figure C.1. Snapshots taken at different times over the course of the simulation (Kirkpatrick et al., 2012)

D Snapshots of the simulation case DES1

The following figures show the development of the model over the simulation time. The figures show the density, velocity and the DDES through several times steps. These figures present the inaccurate handling of the hybrid modelling in the Star CCM+ software where it is seen that LES was not utilized in large regions of the model throughout the simulation.

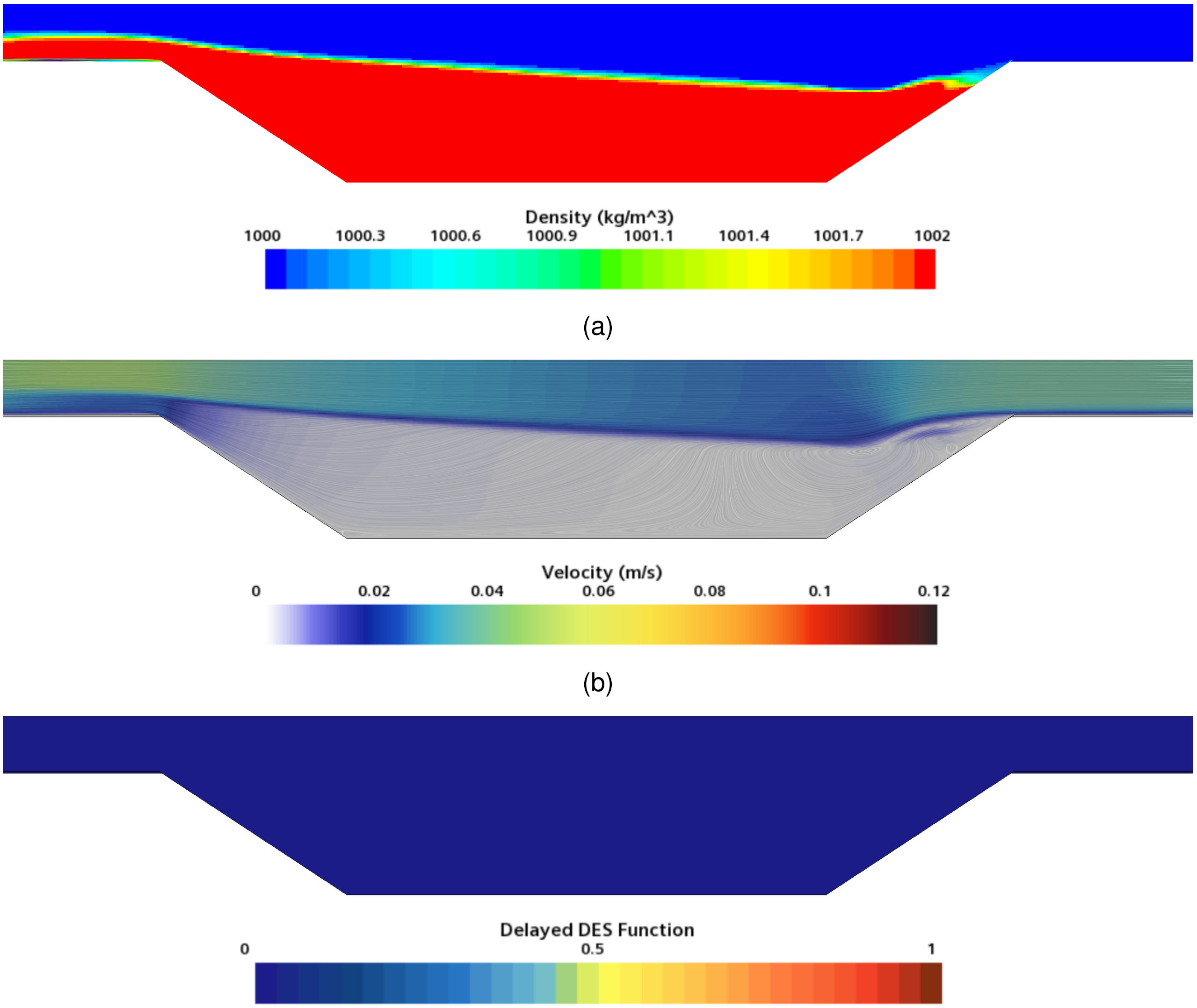

(c)

Figure D.1. Model snapshots for DES1 simulation at 40 Seconds: (a) Density Contour, depicting the fluid density across the model domain, with a scale from blue (fresh water density) to red (saltwater density); (b) Velocity Contour; (c) DDES Function, indicating the computational areas where RANS is active (value of 0, shown in blue) and where the LES is active (value of 1, shown in red).

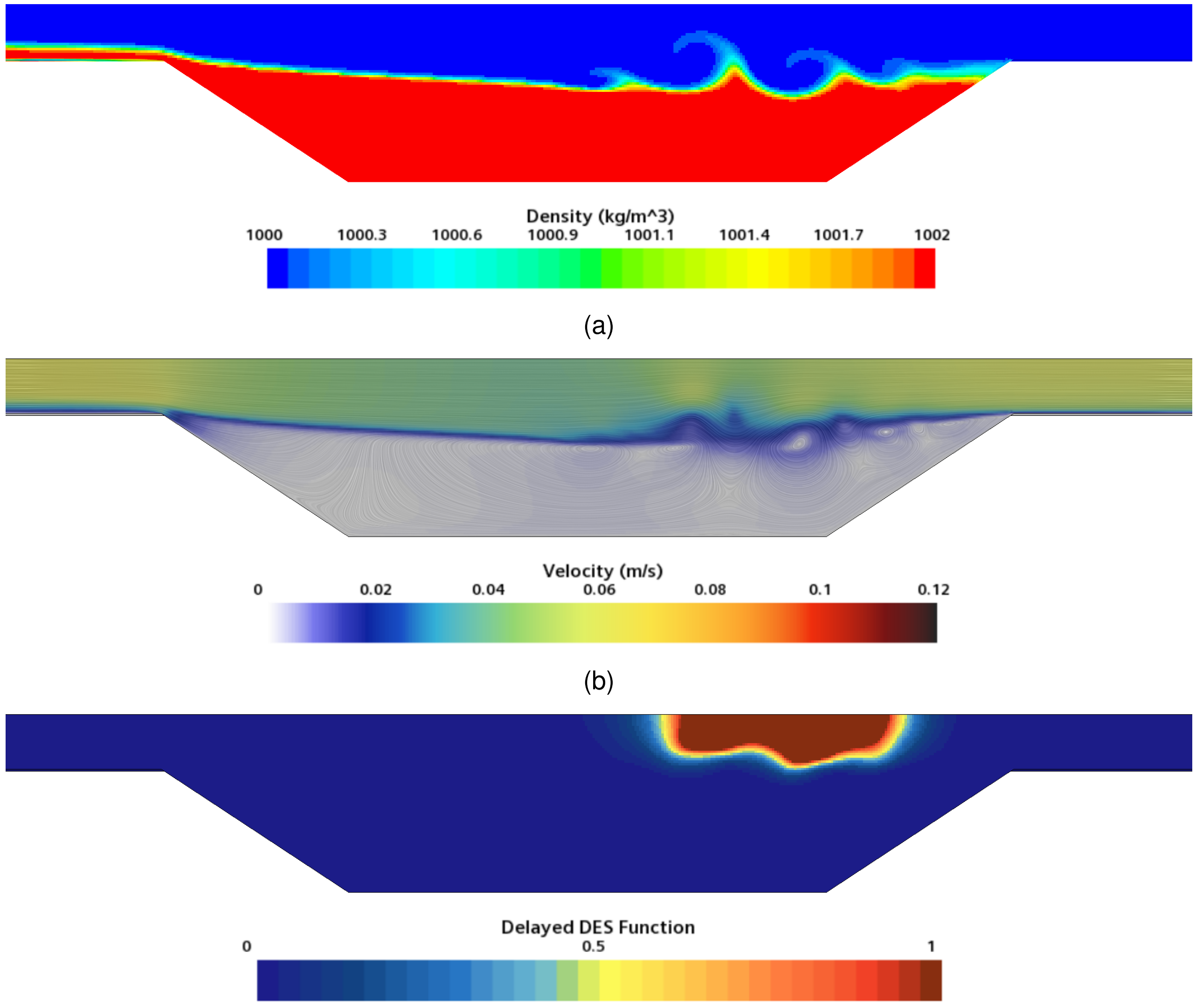

(a)

(b)

(c)

Figure D.2. Model snapshots for DES1 simulation at 60 Seconds: (a) Density Contour, depicting the fluid density across the model domain, with a scale from blue (fresh water density) to red (saltwater density); (b) Velocity Contour; (c) DDES Function, indicating the computational areas where RANS is active (value of 0, shown in blue) and where the LES is active (value of 1, shown in red).

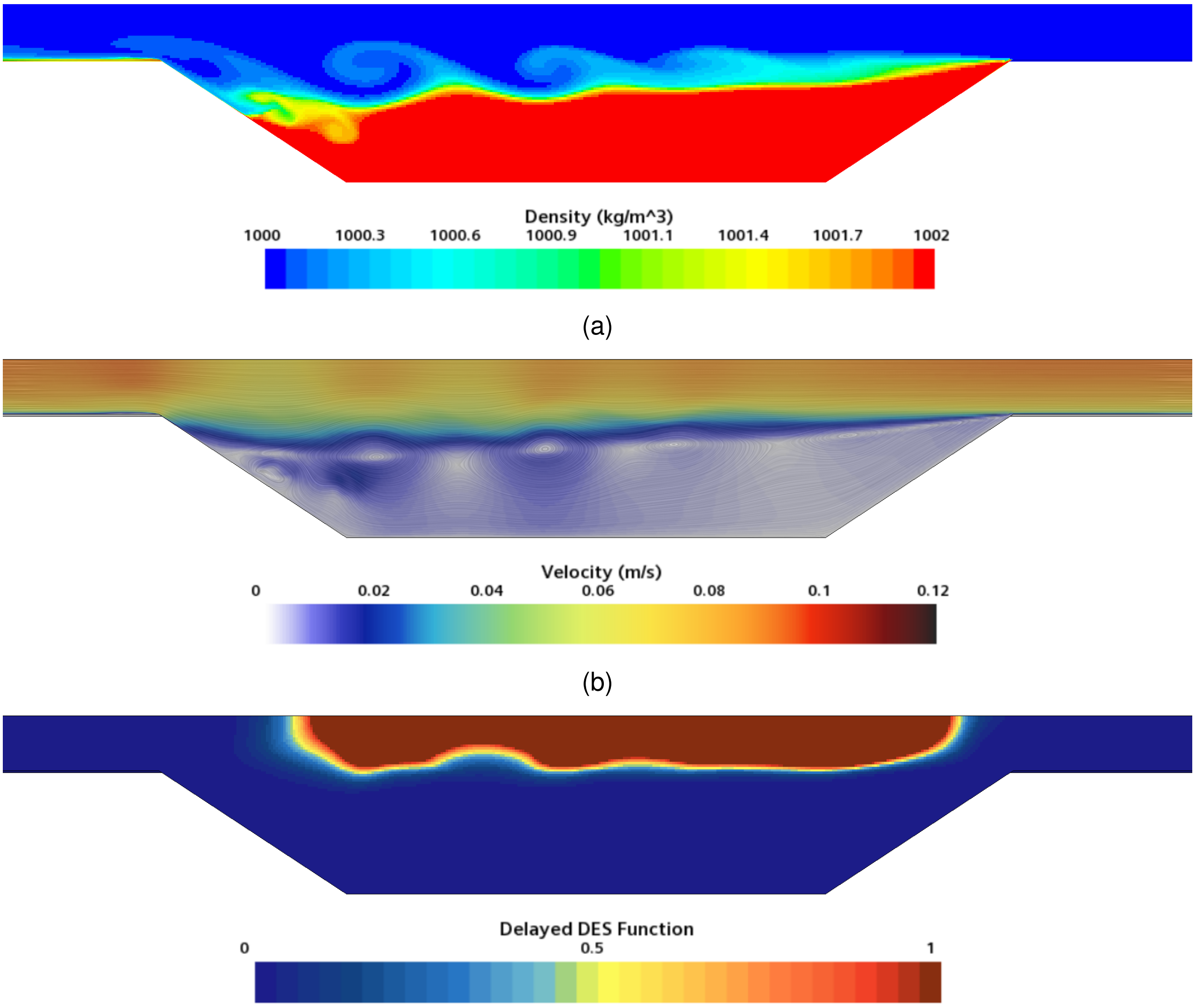

(a)

(b)

(c)

Figure D.3. Model snapshots for DES1 simulation at 100 Seconds: (a) Density Contour, depicting the fluid density across the model domain, with a scale from blue (fresh water density) to red (saltwater density); (b) Velocity Contour; (c) DDES Function, indicating the computational areas where RANS is active (value of 0, shown in blue) and where the LES is active (value of 1, shown in red).

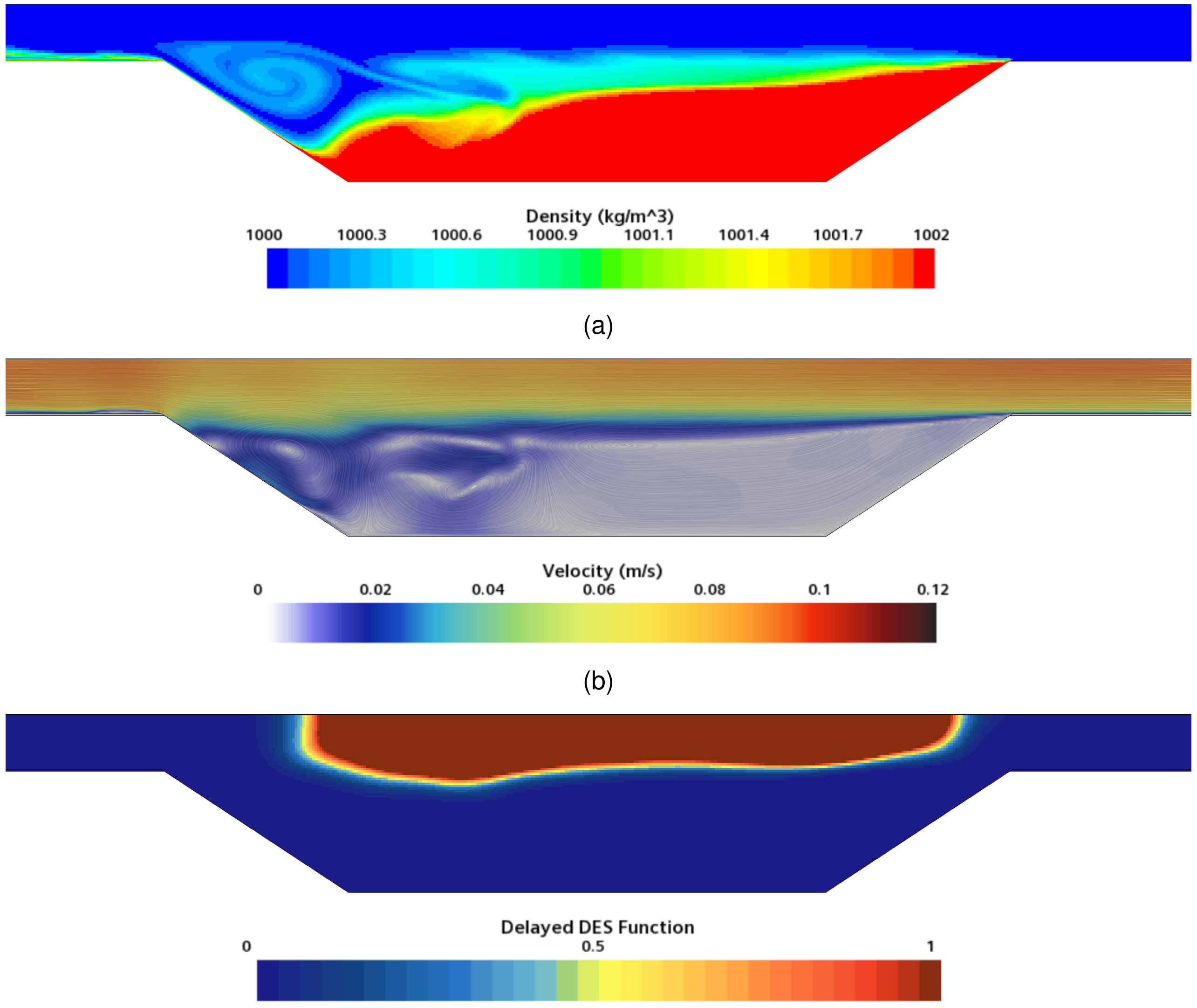

(a)

(b)

(c)

Figure D.4. Model snapshots for DES1 simulation at 120 Seconds: (a) Density Contour, depicting the fluid density across the model domain, with a scale from blue (fresh water density) to red (saltwater density); (b) Velocity Contour; (c) DDES Function, indicating the computational areas where RANS is active (value of 0, shown in blue) and where the LES is active (value of 1, shown in red).

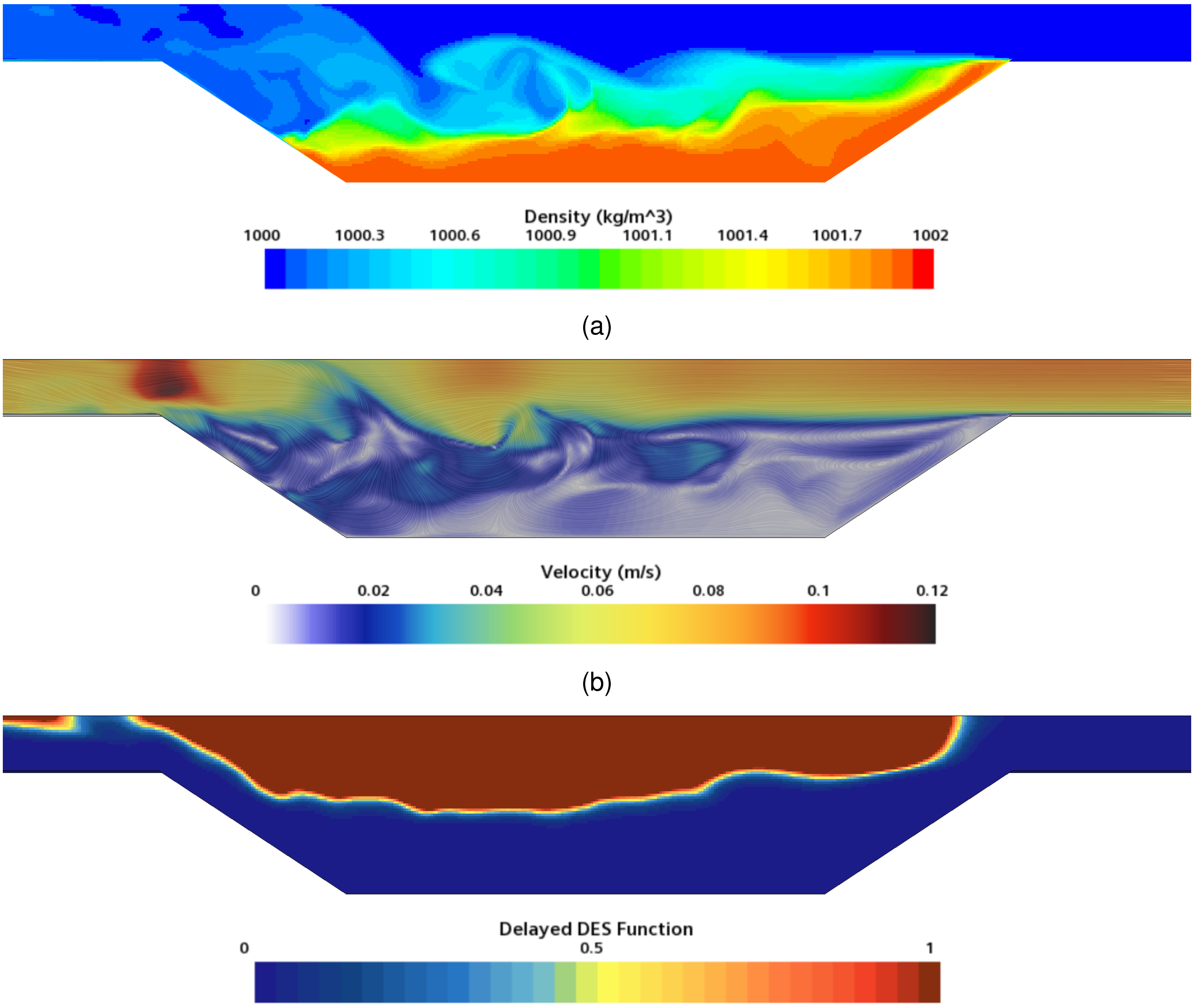

(a)

(b)

(c)

Figure D.5. Model snapshots for DES1 simulation at 200 Seconds: (a) Density Contour, depicting the fluid density across the model domain, with a scale from blue (fresh water density) to red (saltwater density); (b) Velocity Contour; (c) DDES Function, indicating the computational areas where RANS is active (value of 0, shown in blue) and where the LES is active (value of 1, shown in red).

E Snapshots of the hybrid DES modelling

The following figures show the comparison in performance of the DES modelling in Star CCM+ for both the Lab and the Haringvliet models.

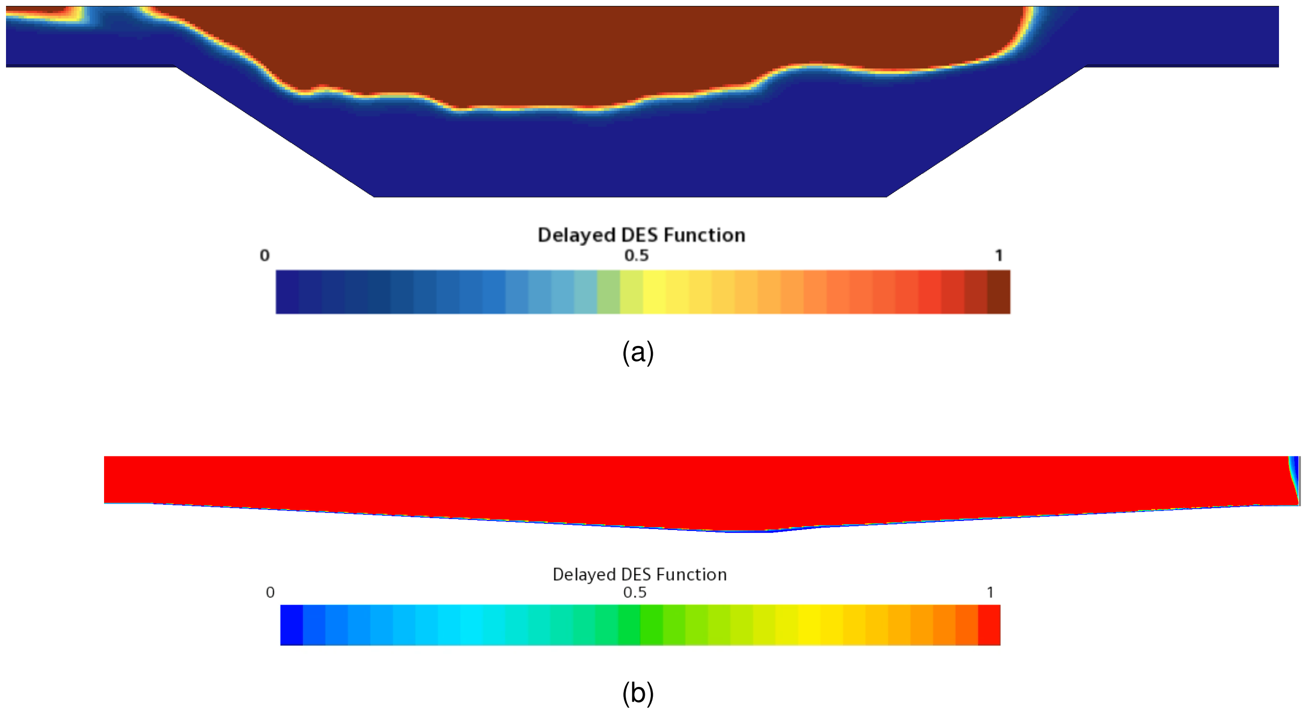

Figure E.1. Model snapshots of the DES modelling in both the Lab and the Haringvliet models: (a) The lab scale at 200 seconds; (b) The Haringvliet model at 45 minutes. The colour bar shows the DDES Function, indicating the computational areas where RANS is active (value of 0, shown in blue) and where the LES is active (value of 1, shown in red).

F Courant number

The figure below shows the performance of the model under different Courant numbers. It is observed that the performance of the model did not show significant sensitivity to varying courant numbers.

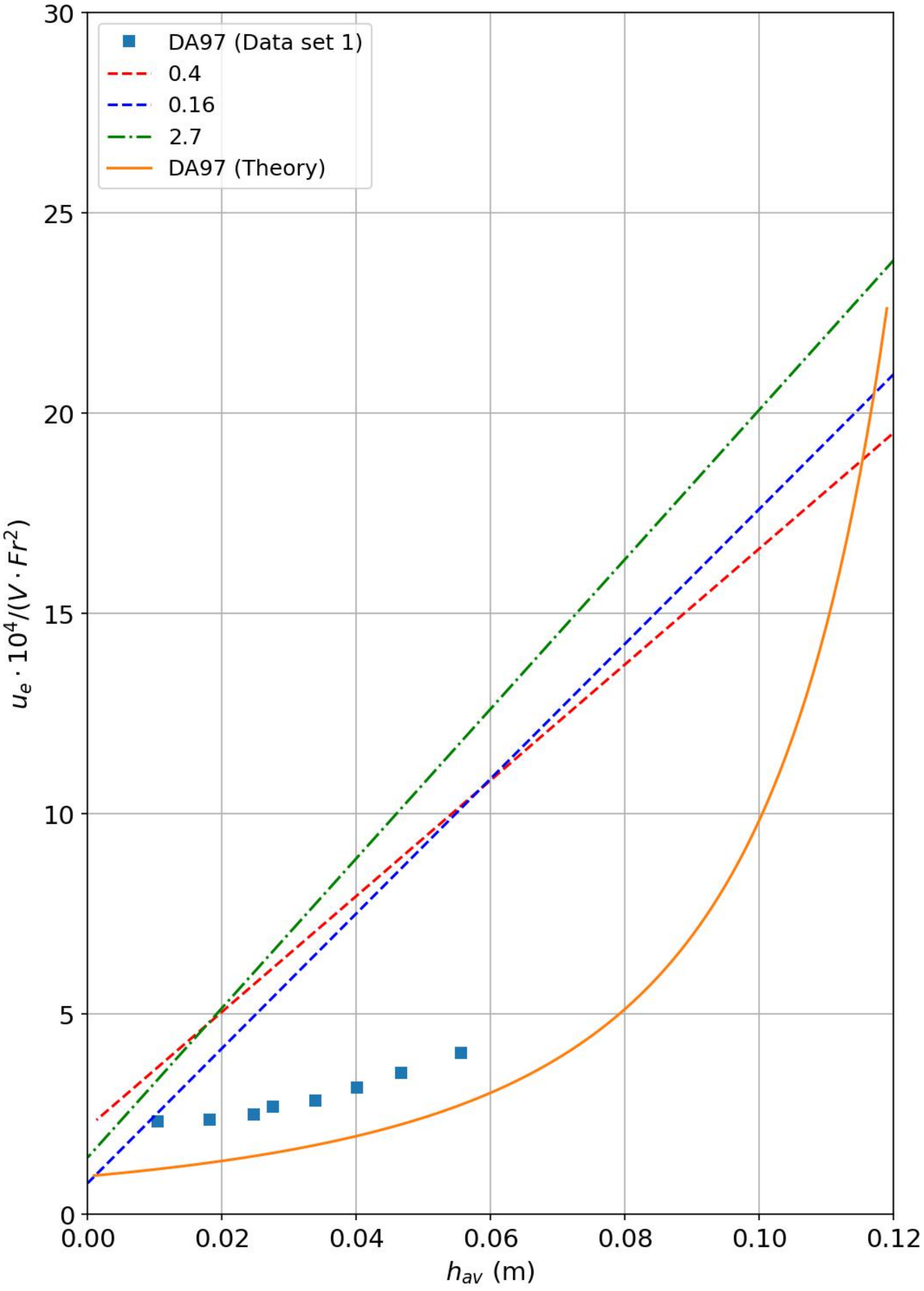

Figure F.1. Entrainment rate for different courant numbers